FRIEDRICH-SCHILLER-
UNIVERSITÄT
JENA

Dissertation

Experiments on Synthetic Dimensions in Photonics

zur Erlangung des Doktorgrades

Doctor rerum naturalium

vorgelegt von

André Luiz Marques Muniz

aus Poços de Caldas

März 2020

Gutachter

1. *Prof. Dr. Ulf Peschel*
   Institut für Festkörpertheorie und Optik
   Friedrich-Schiller-Universität Jena

2. *Prof. Dr. Mordehcai Segev*
   Solid State Institute
   Technion - Israel Institure of Technology

3. *Prof. Dr. Jan Wiersig*
   Institut für Physik
   Otto-von-Guericke-Univerität Magdeburg

Tag der Disputation: 26.01.2021

“We make our world significant by the courage
of our questions and the depth of our answers”.

Carl Sagan

Abstract

Photonic mesh lattices combined with the time-multiplexing technique provide a rich ground to explore complex physical phenomena that rely on the wave theory of light due to ease of resembling and experimental accessibility. It stems from the fact that high-speed photonic devices connected in such loops allow for precise and fast manipulation of amplitude and phase of optical pulses, and high stability of corresponding interferences at their network nodes. In addition to innumerous possibilities of measurements, time-multiplexing through long-range interaction extends the dimensionality of a complex network to two transverse dimensions and opens up new possibilities for research and experiments.

The first and introductory section of the dissertation presents the working principle of a one- and two-dimensional photonic mesh lattice based on the time-multiplexing technique. The basis of a random walk interrelated to the corresponding light and quantum walk is comprehensively discussed as well. Further, the experimental schemes and operational arrangements of amplitude and phase modulation are described in detail for both sets of photonic mesh lattices.

The second part of the dissertation consists of three experiments on a one-dimensional photonic mesh lattice. Firstly, the Kapitza-based guiding light project models the Kapitza potential as a continuous Pauli-Schrödinger-like equation and presents an experimental observation of light localization when the transverse modulation is bell-shaped but with a vanishing average along the propagation direction. Secondly, the optical thermodynamics project experimentally demonstrates for the first time that any given initial modal occupancy reaches thermal equilibrium by following a Rayleigh-Jeans distribution when propagates through a multimodal photonic mesh lattice with weak nonlinearity. Remarkably, the final modal occupancy possesses a unique temperature and chemical potential that have nothing to do with the actual thermal environment. Finally, the quantum interference project discusses an experimental all-optical architecture based on a coupled-fiber loop for generating and processing time-bin entangled single-photon pairs. Besides, it shows coincidence-to-accidental ratio and quantum interference measurements relying on the phase modulation of those time bins.

The third part of the dissertation comprises two experiments on a two-dimensional photonic mesh lattice. The first project discusses the experimental realization of a two-dimensional mesh lattice employing short- and long-range interaction. Besides, it shows the collapse of a broad initial field distribution around a single lattice site caused by the action of

a cubic nonlinearity, which corresponds to a pulse compression scheme working at mW-power levels. To some extent, the second project presents a nonconservative system based on a two-dimensional photonic mesh lattice exploiting parity-time (PT) symmetry. By appropriately modulating the gain/loss contrast as well as the pertinent phase, it experimentally demonstrates the impulse response of this system under both conservative and pseudo-Hermitian conditions where the PT symmetry is broken or unbroken. Besides, it presents a non-Hermitian nonlinear localization of broad Gaussian-like field distribution and, in contrast to what one could expect from a Hermitian system, nonconservative PT solitons display an effective energy growth −a process that makes them more unstable and rapidly induces a collapse event. For higher input power levels, a family of non-Hermitian solitons is also experimentally observed that tends to self-accelerate and move during the collapse.

Zusammenfassung

Photonische Maschengitter in Verbindung mit der Zeitmultiplextechnik bieten einen reichen Grund, um komplexe physikalische Phänomene zu erforschen, die sich auf die Wellentheorie des Lichts stützen, da sie leicht zu ähneln und experimentell zugänglich sind. Sie beruht auf der Tatsache, dass in solchen Schleifen verbundene photonische Hochgeschwindigkeitsvorrichtungen eine präzise und schnelle Manipulation von Amplitude und Phase der optischen Pulse und eine hohe Stabilität der entsprechenden Interferenzen an ihren Netzwerkknoten ermöglichen. Neben unzähligen Messmöglichkeiten erweitert das Zeitmultiplexen durch weiträumige Wechselwirkung die Dimensionalität eines komplexen Netzwerks auf zwei transversale Dimensionen und eröffnet neue Möglichkeiten der Forschung und Experimente.

Im ersten und einführenden Teil der Dissertation wird das Funktionsprinzip eines ein- und zweidimensionalen photonischen Netzgitters vorgestellt, das auf der Zeitmultiplextechnik basiert. Die Grundlage eines Random-Walks, der mit dem entsprechenden Licht- und Quanten-Walk verbunden ist, wird ebenfalls umfassend diskutiert. Weiterhin werden die experimentellen Schemata und Betriebsanordnungen der Amplituden- und Phasenmodulation für beide Sätze photonischer Maschengitter ausführlich beschrieben.

Der zweite Teil der Dissertation besteht aus drei Experimenten an einem eindimensionalen photonischen Maschengitter. Erstens modelliert das auf Kapitza basierende Leitlichtprojekt das Kapitza-Potential als eine kontinuierliche Pauli-Schrödinger-ähnliche Gleichung und präsentiert eine experimentelle Beobachtung der Lichtlokalisierung, wenn die Transversalmodulation glockenförmig ist, aber mit verschwindendem Mittelwert entlang der Ausbreitungsrichtung. Zweitens demonstriert das Projekt der optischen Thermodynamik zum ersten Mal experimentell, dass eine gegebene modale Anfangsbelegung das thermische Gleichgewicht erreicht, indem sie einer Rayleigh-Jeans-Verteilung folgt, wenn sie sich durch ein multimodales photonisches Maschengitter mit schwacher Nichtlinearität ausbreitet. Bemerkenswert ist, dass die endgültige modale Besetzung ein einzigartiges Temperatur- und chemisches Potential besitzt, das nichts mit der tatsächlichen thermischen Umgebung zu tun hat. Schließlich diskutiert das Quanten-Walk-Projekt eine experimentelle volloptische Architektur, die auf einer Koppel-Faserschleife zur Erzeugung und Verarbeitung von verschränkten Einzelphotonenpaaren mit Zeitverzögerung basiert. Darüber hinaus zeigt es Koinzidenz-zu-Zufalls-Verhältnis und Quanteninterferenzmessungen, die sich auf die Phasenmodulation dieser Zeitbins stützen.

Der dritte Teil der Dissertation besteht aus zwei Experimenten an einem zweidimensionalen photonischen Maschengitter. Im ersten Projekt wird die experimentelle Realisierung eines zweidimensionalen Maschengitters unter Verwendung von Kurz- und Langstreckenwechselwirkung diskutiert. Außerdem zeigt es den Kollaps einer breiten anfänglichen Feldverteilung um einen einzelnen Gitterplatz, der durch die Wirkung einer kubischen Nichtlinearität verursacht wird, was einem Impulskompressionsschema entspricht, das bei mW-Leistungspegeln arbeitet. In gewisser Weise stellt das zweite Projekt ein nichtkonservatives System dar, das auf einem zweidimensionalen photonischen Maschengitter basiert, das die parity-time (PT)-Symmetrie ausnutzt. Durch geeignete Modulation des Verstärkungs-/Verlustkontrasts sowie der zugehörigen Phase wird die Impulsantwort dieses Systems sowohl unter konservativen als auch unter pseudo-Hermitischen Bedingungen, bei denen die PT-Symmetrie gebrochen oder ungebrochen ist, experimentell nachgewiesen. Darüber hinaus zeigt es eine nicht-Hermitische nichtlineare Lokalisierung einer breiten gaußähnlichen Feldverteilung, und im Gegensatz zu dem, was man von einem Hermitischen System erwarten könnte, zeigen nicht-konservative PT-Solitonen ein effektives Energiewachstum −ein Prozess, der sie instabiler macht und schnell ein Kollapsereignis auslöst. Bei höheren Eingangsleistungsniveaus wird experimentell auch eine Familie von nicht-eremitischen Solitonen beobachtet, die dazu neigt, sich während des Kollaps selbst zu beschleunigen und zu bewegen.

Contents

1. Photonic Mesh Lattices

1.1. From Light Walk to Synthetic Dimensions

Random events and stochastic processes are commonly present in our daily-basis life [1], [2]. A coin tossed into the air and fluctuating prices in the stock market seems not to be interrelated, but their probabilities can be described by a unique mathematical object, namely a random walk. In particular, a random walk process has applications in many scientific areas, such as engineering [3], [4], physics [5], economics [6], computer science [7], [8], chemistry [4], [9] as well as biology [10]. A classical random walk (CRW) consists of a sequence of random steps for which a walker randomly moves to neighbor positions at every discrete time m with a certain probability p [11]. A remarkable example of CRW is the Galton board of classical particles, in which several one-dimensional (1D) walkers go to the left or right at 50% probability. As a collection of particles takes individually either one direction or another at every discrete time step m, their quantity at each position n is summed up following a normal distribution ($m \gg 1$) due to binomial distribution throughout subsequent time steps [12] (see Figure 1(a)). A two-dimensional (2D) random walk analogously follows the 1D version with an additional degree of freedom of walking onto y and x coordinates.

Contrary to classical particles, a walker as a wave physically splits into two identical fractions of its original one and occupies both neighbor positions [13]. Surprisingly, each position on this random walk is now not governed by incoherent addition of particles, but by interference effects. For this circumstance, a random walk is replaced by a quantum walk (QW) provided that its walker is a particle that follows a quantum mechanical description, such as a trapped ion [14] or a single photon [15]. In a quantum walk measurement, one or multiple quantum particles (walker) evolve on multiple series of two unitary transformations sequentially applied to the walker: “coin” and “step” operations. The first transformation acts on the particle degrees of freedom which describes its internal state, such as up-down spin in trapped ions [14], or horizontal/vertical polarization [16], idler/signal frequency [17], and discrete arrival times [18], [19] in optics. Next, a “step” transformation performs a conditional translation on the walker based on its internal state. On the other hand, light walk (LW) measurements employ a classical description of light as an electromagnetic wave [19], [20] by using an initial walker as a monotone continuous wave (CW) signal [21] or a bright pulse [22]. As a result, the intensity distribution at a given time step is fully equivalent to a probability distribution for its quantum counterpart [18], [23]. Random walk models with

wave propagation opened up a new mark in science for quantum search algorithms [24], [25], quantum computation [26], modeling of diffusion processes [4], [27], complex networks [28], [29], to mention just a few.

Historically, the first prominent LW experiment employed a spatially organized pyramid of beam splitters (BS) for mimicking, in an ingenious way, its classical counterpart (see Figure 1(b)) [30]. As a result, a beam splitter (see Figure 1(c)) reproduces a "coin" operator, meaningfully splitting photons at its transmitted and reflected output by a 50/50 ratio [31]. That portion of the light that undergoes the reflected port acquires a phase shift of $\pi/2$. Consequently, two coincident light beams experience constructive or destructive interference (or anything in between) based on their relative phase [13]. On the condition that external phase fluctuations do not influence the LW process, a completely distinct distribution resembles at the end in contrast to its classical counterpart (see Figure 1(d)). Whereas particles in CRW spread at a diffusive rate (standard deviation $\propto \sqrt{m}$), light spreads with ballistic speed $\propto m$, thus reaching farther positions n away from its initial point [7], [25]. However, the pyramid of optical free-space beam splitters is experimentally challenging since the number of components (photodetectors and beam splitters) exponentially increases with the number of time steps.

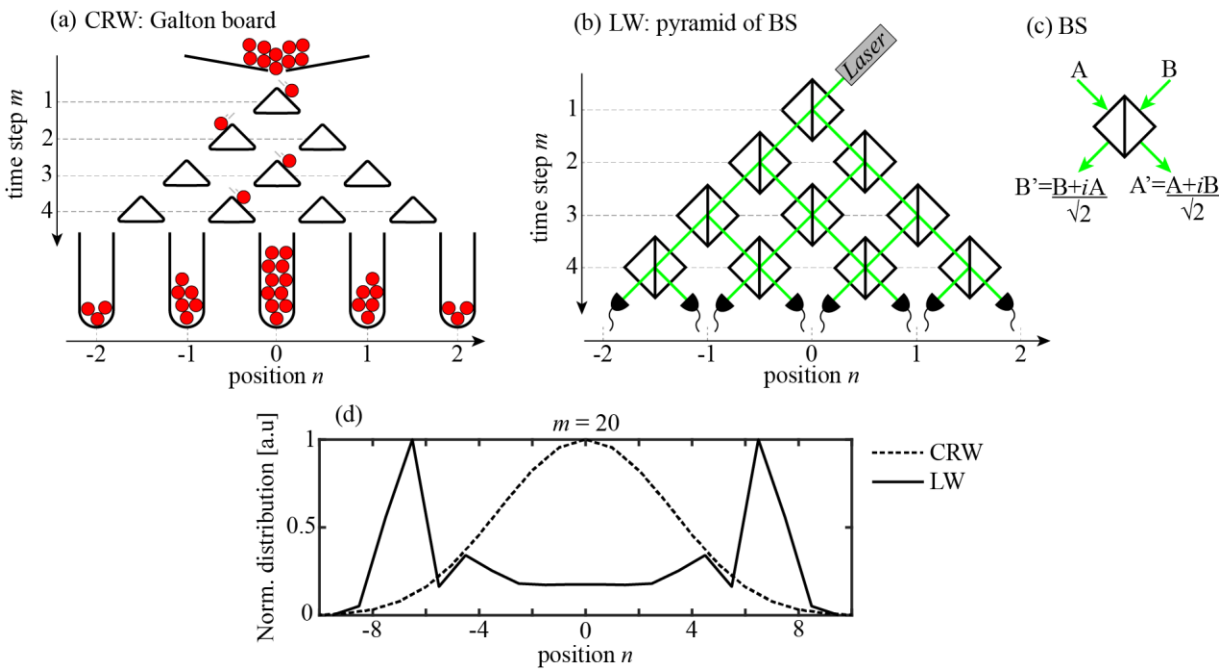

Figure 1: (a) Classical random walk (CRW) described by a Galton board. (b) Light walk (LW) experiment realized by a spatially-organized pyramid of beam splitters (BS). (c) Working principle of a 50/50 splitting ratio BS with input (A and B) and output (A' and B'). (d) Comparison of the final distribution of a classical random walk and a light walk.

To solve this difficulty, new approaches have been reported exploiting degrees of freedom of light, such as polarization [30], [32], frequency [17], [33], [34], and arrival time [35]–[37]. The latter utilizes the well-known technique of time-division multiplexing (TDM) of telecommunication channels, which encodes information (amplitude and phase of the optical pulses) into a single channel (an optical fiber) as well as discretizes the time domain into temporal packages (TP) (see gray boxes in Figure 2(b) and Figure 3(b)) [38]. Importantly, each TP in a coupled-fiber loop corresponds to a time step m of the pyramid of beam splitters and each loop stands for the synthetic transverse coordinate [22], [39]. The present thesis focuses on the time-multiplexing approach as a framework for investigating physical phenomena in 1D and 2D photonic mesh lattices.

Recently, the concept of synthetic dimension has been broadly used as a framework for researching unexploited complex physical phenomena that are experimentally challenging or practically impossible in the physical world conditions [39]. The physics of a photonic structure is mostly described by its apparent geometric dimensionalities, such as 1D photonic crystals [40], [41], 2D graphene layers [42], or 3D metamaterials [43]. However, it is possible to explore physics in a space with a dimensionality that is higher as compared to the apparent geometrical dimensionality of its structure [39], [44], such as 1D optical fiber resembling a 2D photonic mesh lattice by time-multiplexing technique [36], [45].

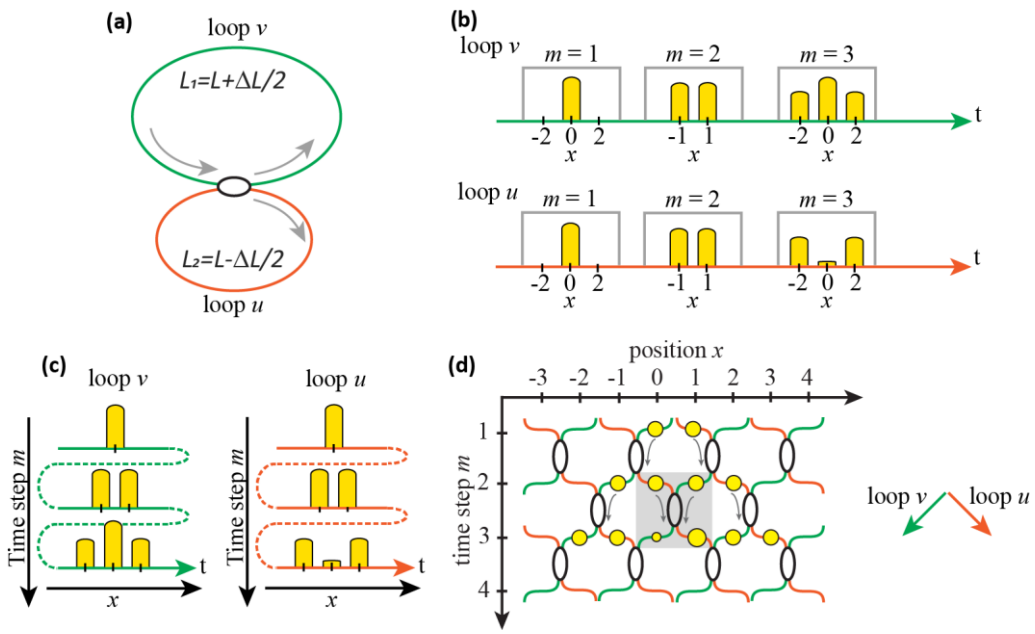

Figure 2: 1D mesh lattice realized by coupled-fiber loops and time-multiplexing technique. (a) Two slightly dissimilar fiber loops are connected by an optical coupler. (b) Arrival times of a chain of pulses in the loop $\boldsymbol{v}$ and $\boldsymbol{u}$ and corresponding temporal packages representing time steps $\boldsymbol{m}$ (gray boxes). (c) The arrow of time is wisely organized into equivalent mesh lattices, featuring a synthetic transverse dimension $\boldsymbol{x}$. (d) Correspondent 1D mesh lattice. The unit cell of the mesh lattice is depicted in a gray box.

The synthetic dimension is thus determined by the nature of coupling, where multiple states in a mesh lattice are able to "walk" according to its dimensionality [39]. In this thesis, the notation ascribed to the lattice position n in previous works [22], [35], [37], [46], [47] is changed now to the Cartesian coordinate notation xy for simplicity.

For tailoring 1D photonic mesh lattices, the time-multiplexing technique produces a periodic temporal system based on two slightly dissimilar coupled-fiber loops (see Figure 2(a)). An optical coupler connecting the fiber loops resembles an identical outcome of that pyramid of BS. The temporal sequence of pulses is reordered into an equivalent spatial mesh lattice (see Figure 2(b) and (c)). In this configuration, optical pulses are represented by their intensities in a photonic mesh lattice and the whole system thus resembles the light dynamics in a waveguide array with lumped coupling [22] (see Figure 2(d)). Similarly, a 2D arrangement employs two pairs of fiber loops, each standing for one synthetic transverse dimension (see Figure 3(a)). The 2D time-multiplexing technique produces a similar periodic temporal system as the 1D case, but now the inner loop inserts a shorter time delay than the outer loop, thus providing an additional means of coupling known as short- and long-range interaction [36], [45], [48] (see Figure 3(b)). The one-dimensional sequence of pulses in the time domain is mapped onto a 2D photonic mesh lattice (see Figure 3(c)), exhibiting pulse intensities every roundtrip on xy-axes (see Figure 3(d)).

The feasibility of using the coupled-fiber loop method enables only one (two) optical coupler and two (four) photodetectors to simulate a 1D (2D) photonic mesh lattice, regardless of the number of roundtrips. In addition, since always the same components are passed, any phase disturbance with a time scale smaller than the measurement time influences all pulses in the same way, and, therefore, the system acts as a self-aligning interferometer. An even richer ground is expected by using in-fiber and commercially available high-speed telecommunication devices, such as amplitude (AM) and phase (PM) modulators, variable couplers (VC), and Erbium-doped fiber amplifiers (EDFA), in order to fully control and manipulate optical pulses. All experiments in the present dissertation are performed with bright pulses from a coherent laser source (except quantum interferences in Section 2.4), thus approaching the classical description of light as an electromagnetic wave. The concept developed here for 1D and 2D photonic mesh lattices is primarily based on the original ideas of discrete-time quantum walks published in [18], [23], [31], [32], [36], [49], [50].

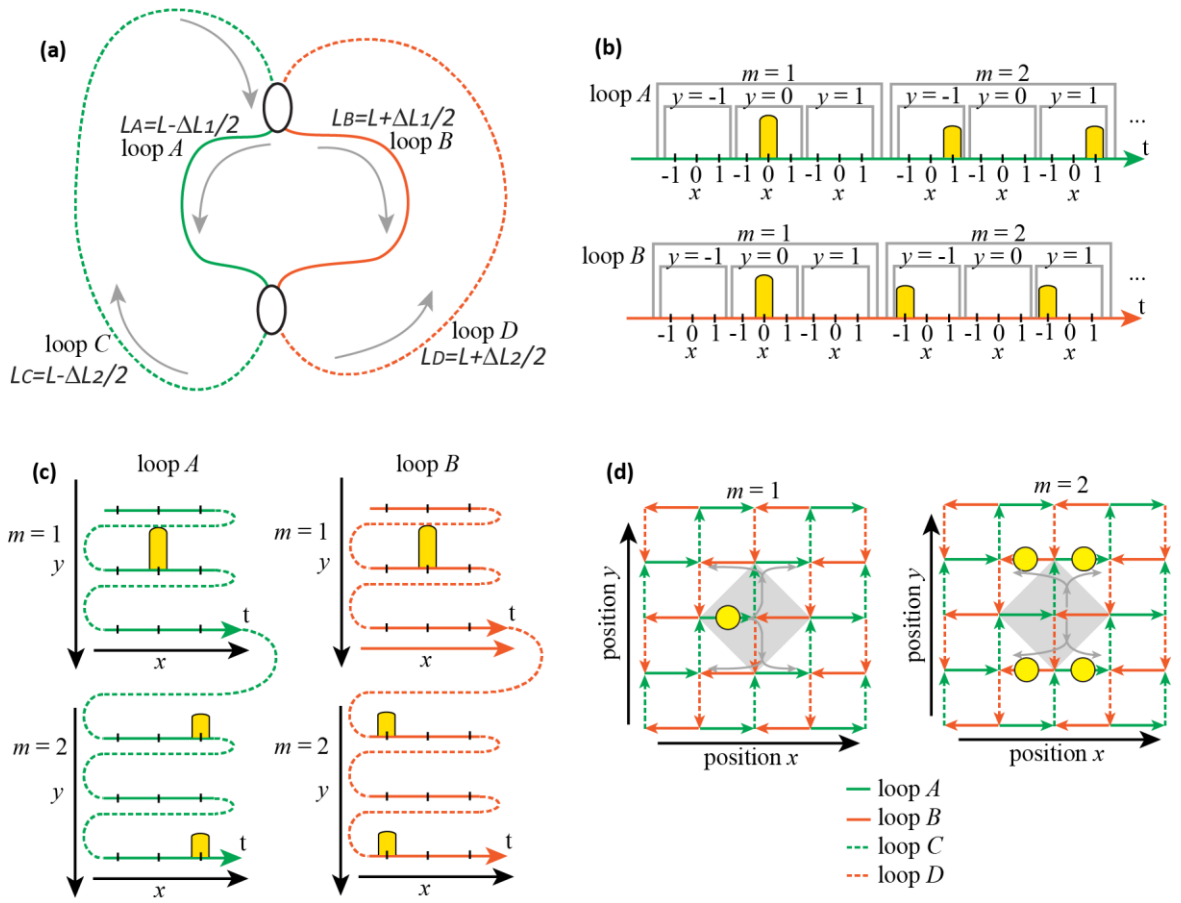

Figure 3: 2D mesh lattice realized by coupled-fiber loop and time-multiplexing technique. (a) Four slightly dissimilar fiber paths are connected by two optical couplers to form two fiber loops. (b) Arrival time of a chain of pulses in loop $\boldsymbol{A}$, $\boldsymbol{B}$, $\boldsymbol{C}$ and, $\boldsymbol{D}$ and correspondent temporal packages representing short- and long-range interaction and time steps $\boldsymbol{m}$ (gray boxes). (c) The arrow of time is wisely organized into an equivalent mesh lattice, featuring two synthetic transverse dimensions in $\boldsymbol{xy}$-axes. (d) Correspondent 2D mesh lattice. The unit cell of the mesh lattice is depicted in a gray box.

1.2. Experimental setup: 1D Photonic Mesh Lattice

The experimental setup consists of two main parts: a pulse generation module (see Figure 4) and a coupled fiber-based loop set-up (see Figure 5). In the pulse generation part, a CW signal at carrier wavelength $\lambda = 1550\ nm$, emitted by a high-coherent laser diode, is cut into a train of rectangular pulses of 22 ns temporal width by using a Mach-Zehnder modulator (MZM).

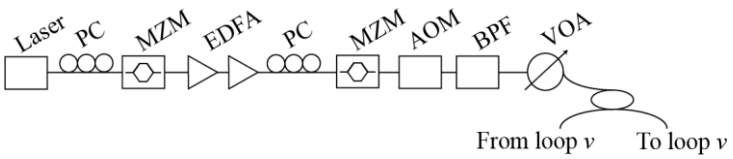

Figure 4: Pulse generation module of the experimental setup. PC: polarization controller; MZM: Mach-Zehnder modulator; EDFA: erbium-doped fiber amplifier; AOM: acousto-optic modulator; BPF: bandpass filter; VOA: variable optical attenuator.

The pulse sequence is amplified by two EDFAs. Afterward, another MZM is employed to eliminate the amplified background noise between adjacent pulses and thus to reach a higher extinction ratio. A tunable optical bandpass filter (BPF) placed thereafter spectrally purifies the pulses by removing the out-of-band amplified spontaneous emission (ASE) originating from the amplifier. The peak power of the resulting pulses is coarsely controlled by the variable optical attenuator (VOA), whereas a fine-tuning of the peak power is carried out by an acousto-optic modulator (AOM) with a variable transmission ratio. The AOM is also used for performing an automatized control over different power levels.

The generated 22 ns long pulse is injected into loop v by an optical switcher acting as a gate, allowing only one seed pulse per measurement session to enter the fiber-coupled loop system, as shown in Figure 5. The experimental platform is built up of two slightly different fiber loops, connected via an optical coupler or VC. Each path comprises of a standard single-mode fiber (SSMF) of few meters long (nonlinear coefficient $\gamma \approx 1.1\ (\mathrm{W.km})^{-1}$ [51]) combined with approximately 4 km of dispersion-compensating fiber (DCF, type: OFS-HSDK, nonlinear coefficient $\gamma \approx 7\ (\mathrm{W.km})^{-1}$ [52]) to ensure an additional boost of nonlinearity due to the higher nonlinear coefficient. During one roundtrip, pulses which propagate through the longer (v) or shorter loop (u) result in a total travel length of about $L \approx$ 4 km or a roundtrip time of $\overline{T} \approx 20$ µs. However, due to the different fiber lengths ($\Delta L \approx$ 20 m), pulses arrive after one roundtrip at different time slots, which encodes the traveled distance and creates discrete arrival times ($\Delta T \approx 50$ ns) being equivalent to synthetic positions $x - 1$ (loop u) or $x + 1$ (loop v) in the effective spatial domain, respectively. After one roundtrip, m increases by one and the process starts again. For any m roundtrips, pulses arrive in the photodetectors (see Figure 6(a)) at different arrival times as

$$T_{\text{arrival}}(m, x) = m \underbrace{\left(\frac{T_v + T_u}{2}\right)}_{\overline{T}} + \underbrace{\left(\frac{T_v - T_u}{2}\right)}_{\Delta T} x \tag{1}$$

where x stands for the effective spatial position. In this experiment, pulse energies are measured with a photodetector, the signal of which is sampled electronically by an offline digital signal processing software, as shown in Figure 6(b)-(d).

The size of the synthetic lattice and the maximum number of roundtrips are limited by the used fiber lengths. Provided that the initial light distribution is always spreading, e.g. 1D LW depicted in Figure 6(e), the earliest pulse from the roundtrip $m + 1$ will overlap with the latest pulse from roundtrip m [32]. Therefore, the maximum number of positions along the

transverse direction is given by $x_{\max} \approx \overline{T}/\Delta T$. Besides, to reduce noise and to improve the measurement quality of the photodetected pulse sequence, we always average over 100 subsequent single runs of the experiment, each requiring about ~30 ms.

Additionally, each path possesses an EDFA amplifier, which compensates for energy losses accumulated in every roundtrip from the passive and active optical components depicted in the scheme as well as from the pulse propagation through SSMF and DCF fibers (see Figure 5). Effective gain factors of the EDFAs are controlled by tuning the power of a corresponding pilot CW laser, which operates at a blue-shifted wavelength of $\lambda = 1536$ nm. This pilot signal is combined with the pulses via a wavelength division multiplexer (WDM) in front of the respective EDFAs and removed afterward by tunable BPFs placed directly behind the amplifiers. Next, PM and MZM, control phase and amplitude of the pulses within the loops, respectively. The polarization state of the signal is controlled by an additional photodetector coupled via polarizing beam splitters (PBS) in each of the loops. Minimizing the signals at these photodetectors ensures a fixed and well-controlled polarization state of all pulses at the optical coupler to ensure interference and to guarantee proper operation of all polarization-maintaining components, such as optical coupler, PMs, and MZMs. The optical coupler, which connects both loops, is described by the following 2×2 matrix

$$C = \begin{pmatrix} t & ir \\ ir & t \end{pmatrix}, \tag{2}$$

where t and r denote real-valued transmission and reflection coefficients ($t^2 + r^2 = 1$). During linear propagation through an optical fiber, pulses of width T_0 stretch to $\sqrt{2}T_0$ after the so-called dispersion length L_D given by

$$L_D = \frac{T_0^2}{|\beta_2|}, \tag{3}$$

where β_2 denotes the group velocity dispersion with a value of $\sim 10^5$ fs²/km for DCF at 1550 nm. Given the initial optical pulse is 22 ns long in the experiment, the dispersion length L_D is approximately $2.5 \cdot 10^6$ km and, as that loop length (L) is 4 km, a single optical pulse in the system can propagate up to $62.5 \cdot 10^4$ round trips (m) without experiencing significant spreading in time. Since only ~600 roundtrips are utilized in the experiments, dispersion effects can be safely neglected or, in other words, pulses can be modeled as monochromatic under these experimental conditions.

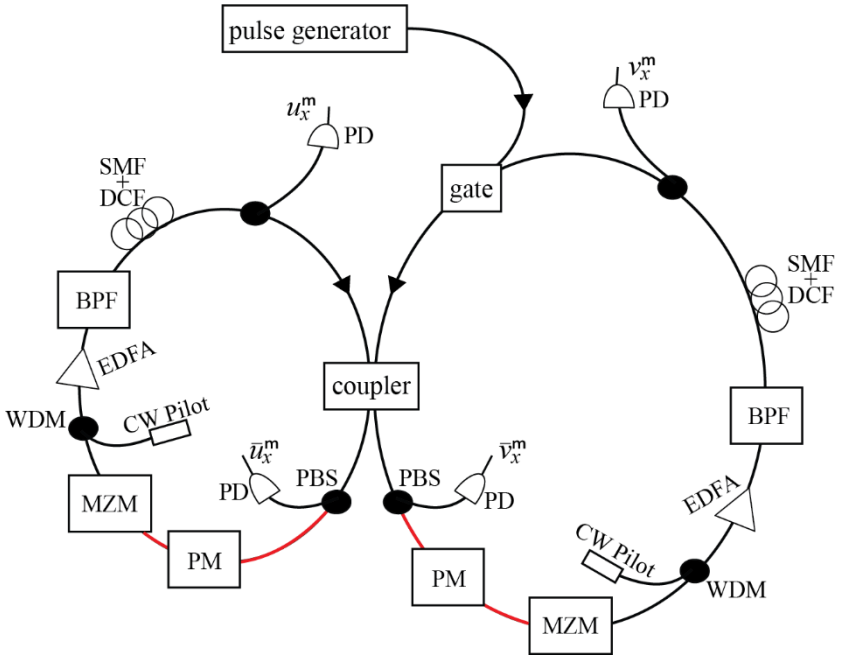

Figure 5: Coupled fiber loop connected via a variable coupler. A pulse is created and injected into the loop *v*. Each fiber path comprises an erbium-doped fiber amplifier (EDFA) for loss compensation and **4** km of optical fiber. Mach-Zehnder modulators (MZM) and phase modulators (PM) allow for amplitude and phase modulation. Polarization-maintaining single-mode fiber and standard single-mode fiber are depicted as red and black lines, respectively. BPF: bandpass filter; WDM: wavelength division multiplexer; gate: optical switcher; SMF: single-mode fiber; DCF: dispersion-compensating fiber; PD: photodetector; PBS: polarizing beam splitter.

Therefore, pulse dynamics is effectively described in terms of amplitudes and carrier-envelope phases, altogether encoded in the complex amplitudes u_x^m and v_x^m during m roundtrips (or coupling length) at position x

$$u_x^{m+1} = (t_{x-1}^m u_{x-1}^m + i r_{x-1}^m v_{x-1}^m)\exp(i\chi|t_{x-1}^m u_{x-1}^m + i r_{x-1}^m v_{x-1}^m|^2)\exp(i\varphi_u), \quad (4)$$

$$v_x^{m+1} = (t_{x+1}^m v_{x+1}^m + i r_{x+1}^m u_{x+1}^m)\exp(i\chi|t_{x+1}^m v_{x+1}^m + i r_{x+1}^m u_{x+1}^m|^2)\exp(i\varphi_v), \quad (5)$$

where t_x^m and r_x^m are the splitting ratio ($t^2 + r^2 = 1$) of the optical coupler from Equation (2). In this model, χ denotes an effective nonlinearity, in which optical pulses acquire a nonlinear phase shift proportional to their power (see Section 1.6). The last term in Equations (4) and (5) denote an external phase modulation protocol in loop v (φ_v) and u (φ_u) for tuning the band structure of the system (see Section 1.4) or creating an effective phase potential.

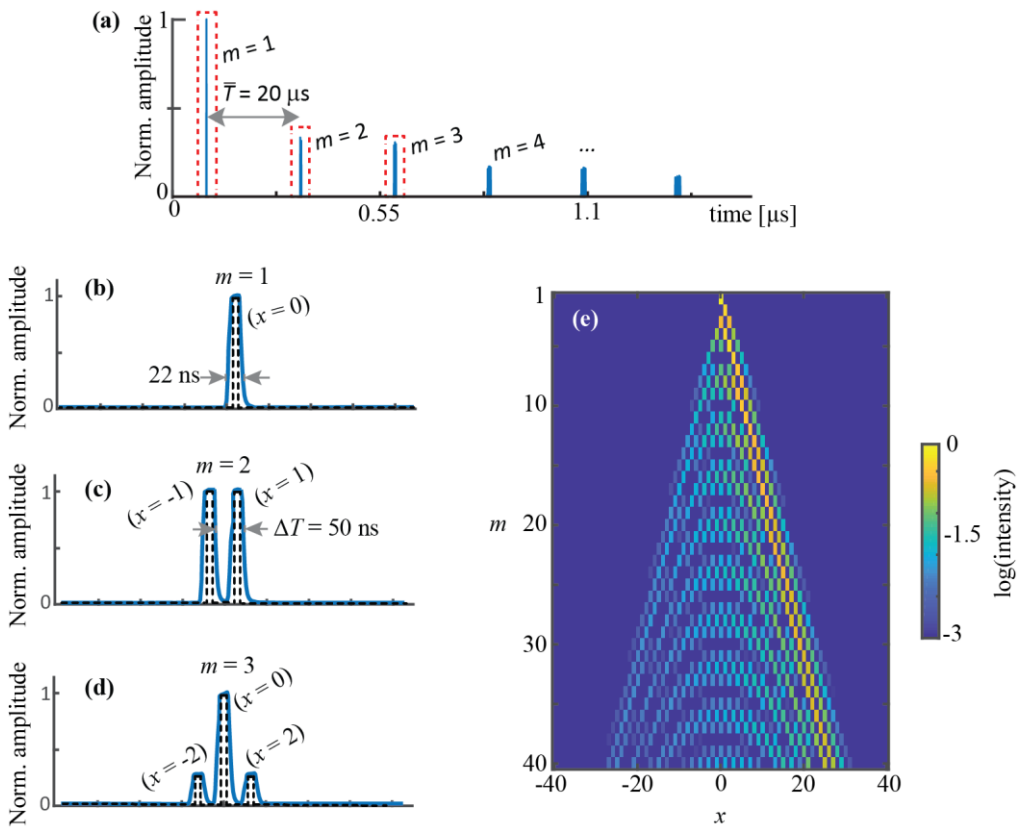

Figure 6: (a) During each round trip, each pulse splits and interferes into the 50/50 couplers and arrives with different arrival times at the photodetectors. (b)-(d) Arriving pulses are photodetected (blue line), sampled electronically (black dashed line) by computer software and (e) mapped onto a 1D spatially $\boldsymbol{x}$ representation (loop $\boldsymbol{v}$; 1D Light walk for $\boldsymbol{\varphi_{u,v}} = \mathbf{0}$).

1.3. Experimental setup: 2D Photonic Mesh Lattice

In the 2D photonic mesh lattice, the initial 22 ns long pulse is generated similarly to the 1D case (see Figure 4) and injected into loop C by an optical switcher, as shown in Figure 7. The experimental platform is built up of four paths of slightly different fiber lengths, arranged as inner and outer loops connected by two 50/50 couplers. Each path comprises of an SSMF of 30 km long (nonlinear coefficient $\gamma \approx 1.1\ (\mathrm{W.km})^{-1}$ [51], [53]) combined with approximately 4 km of DCF fiber (type: OFS-HSDK, nonlinear coefficient $\gamma \approx 7\ (\mathrm{W.km})^{-1}$ [52]) to ensure an additional boost of nonlinearity due to the higher nonlinear coefficient.

In addition, each path possesses an EDFA amplifier, which compensates for energy losses accumulated in every roundtrip from the passive and active optical components depicted in the scheme as well as from the pulse propagation through SSMF and DCF fibers. Effective gain factors of the EDFAs are controlled by tuning the power of a corresponding pilot CW laser, which operates at a blue-shifted wavelength of $\lambda = 1536$ nm. This pilot signal is combined with the pulses via a wavelength division multiplexer (WDM) in front of

the respective EDFAs and removed afterward by tunable BPFs placed directly behind the amplifiers. Next, PM and amplitude modulators (AOM and MZM) control the phase and amplitude of the pulses within the loops, respectively. The polarization state of the signal is controlled by an additional photodetector coupled via polarizing beam splitters (PBS) in each of the loops. Minimizing the signals ($\bar{A}$ and $\bar{B}$) at these photodetectors ensures a fixed and well-controlled polarization state of all pulses at the optical coupler to ensure interference and to guarantee proper operation of all polarization-maintaining components, such as optical coupler, PMs, and MZMs.

As depicted in Figure 7, AOMs are placed at the beginning of the inner loop, but MZMs in the outer ones. The AOMs provide a higher suppression ratio and require only an RF signal. Although having longer switching times compared to MZMs, they are still fast enough for amplitude modulation on time scales in the order of microseconds. Additionally, the performance of the AOMs does not depend on the state of polarization, which simplifies the setup considerably. Likewise, MZMs in the outer loop provide much faster control of pulses in the nanoseconds range but require DC bias control and polarization stability. The mechanism used to implement a 2D photonic mesh lattice relies on the pulse arrival time (similarly to the 1D scheme [22]) and results in a straightforward mapping from the temporal evolution through the fiber loops onto an equivalent 2D spatial mesh lattice (see Figure 8(a)).

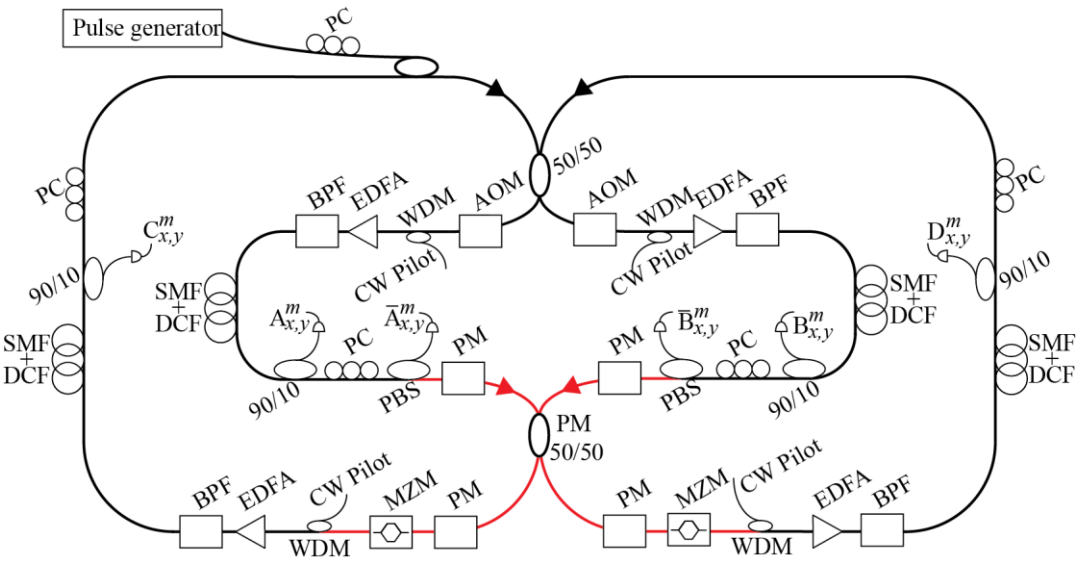

Figure 7: Two pairs of fibers are connected via 50/50 couplers (see upper panel). A pulse is created and injected into the outer left path. Each fiber path has **30** km of optical fiber and an erbium-doped fiber amplifier (EDFA) for loss compensation. Acousto-optic modulators (AOM) in the inner and Mach-Zehnder modulators (MZM) in the outer pair allow for amplitude modulation. Additionally, phase modulators (PM) are placed in both inner and outer loops. Polarization-maintaining single-mode fiber and standard single-mode fiber are shown in red and black colors, respectively. BPF: bandpass filter; WDM: wavelength division multiplexer; gate: optical switcher; SMF: single-mode fiber; DCF: dispersion-compensating fiber; PD: photodetector; PBS: polarizing beam splitter.

All fiber patches shown in Figure 7 are approximately 30 km long, where the two inner ones (A and B) differ by $\Delta L_{\text{inner}} = L_A - L_B \approx 600$ m ($\Delta T_{\text{inner}} = 3$ µs), while the two outer ones (C and D) differ by $\Delta L_{\text{outer}} = L_C - L_D \approx 6$ m ($\Delta T_{\text{outer}} = 30$ ns). During one roundtrip, the pulses which propagate through the inner and outer loops result in a total travel length of about 60 km or a roundtrip time of $\overline{T} = 300$ µs. However, due to the different fiber lengths, pulses arrive after one roundtrip at different time slots, which encodes the traveled distance (see Figure 8(b)). After one roundtrip, the pulse that took the shorter inner and/or outer path arrives first, whereas the pulse that propagated through the longer inner and/or outer path is delayed. Thus, the arrival time

$$T_{\text{arrival}} = m\underbrace{\left(\frac{T_A + T_B}{2} + \frac{T_C + T_D}{2}\right)}_{\overline{T}} + \underbrace{\left(\frac{T_A - T_B}{2}\right)}_{\Delta T_{\text{inner}}} x + \underbrace{\left(\frac{T_C - T_D}{2}\right)}_{\Delta T_{\text{outer}}} y \tag{6}$$

is given by a linear combination of the roundtrip time $\overline{T}$ and the length differences ΔT_{inner} and ΔT_{outer}. In this model, $x, y,$ and m are integer numbers, where m counts the number of roundtrips and x, y are increased or decreased by 1 after each roundtrip through the longer or shorter patch of the inner and outer paths.

Based on Equation (6), the earliest pulse taking the shorter inner and outer paths arrives at $T_{\text{arrival}} = T_B + T_D$ and thus $x = -1$ and $y = -1$, which is equal to a step to the left bottom on the 2D lattice. The latest pulse arrives at $T_{\text{arrival}} = T_A + T_C$, which corresponds to $x = 1$ and $y = 1$ (right top on the lattice). Taking the inner short and outer long paths lead to a delay of $T_{\text{arrival}} = T_B + T_C$, which means $x = -1$ and $y = 1$ (left top). The last case, i.e. a roundtrip through the inner long and outer short paths, results in $T_{\text{arrival}} = T_A + T_D$ ($x = 1$ and $y = -1$, or right bottom of the 2D lattice). Therefore, the 2D lattice can be created by time multiplexing as depicted in Figure 8. This mesh lattice displayed in Figure 3(d) and Figure 8(a), is for instance equivalent to a 2D waveguide array and both 50/50 couplers resemble the effect of wave coupling to neighboring waveguides in the horizontal or vertical direction. Consequently, each roundtrip m in this system can be considered as a propagation step by one coupling length in a 2D waveguide array [36], [45].

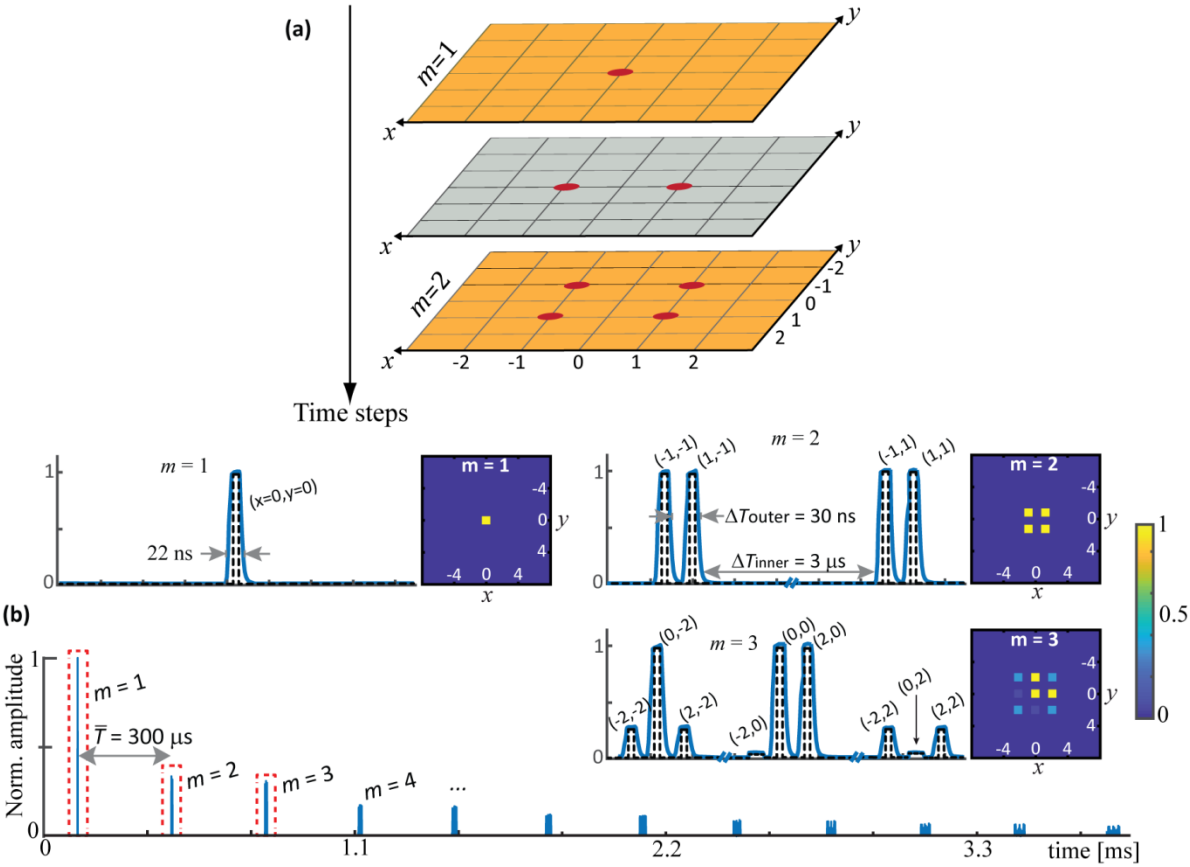

Figure 8: (a) Pulse arrival by time multiplexing mapped onto a 2D lattice. (b) During each roundtrip, each pulse splits and interferes into the 50/50 couplers and arrives with different arrival times at the photodetectors. The pulse amplitudes are photodetected (blue line), sampled electronically (black dashed line) by computer software, and mapped onto a 2D spatially $\boldsymbol{x}$-$\boldsymbol{y}$ representation.

The size of the mesh lattice and its maximum number of roundtrips are limited by the used fiber lengths, provided that the initial light distribution, e.g. 2D Light Walk as shown in Figure 9, is always spreading [18], [45]. At some roundtrip m of the propagation, the earliest pulse from the roundtrip $m+1$ will overlap with the latest pulse from roundtrip m. Therefore, the maximum number of positions along the horizontal direction is given by $x_{\max} \approx \overline{T}/\Delta T_{\text{inner}}$. Analogously, time-multiplexing fails if, during one roundtrip, two pulses from adjacent timeslots overlap. This results in a maximum vertical lattice size $y_{\max} \approx \Delta T_{\text{inner}}/\Delta T_{\text{outer}}$. Interestingly, there are different pathways and sequences through the loops that some pulses can acquire the same time delay and, consequently, being interfered with since only pulses arriving at the same timeslot in a 50/50 coupler can interact. For example, pulses propagating first through the shorter inner and outer paths and afterward through the longer inner and outer long paths arrive at the same time as the pulses that first took the longer inner and outer paths and then the shorter inner and outer patches. Hence, these pulses finally arrive at the same lattice point but following different trajectories. Since pulses travel

always through the same fiber pieces and components, they acquire the same time delays and phases over subsequent roundtrips at least within the time scales below those of fiber length fluctuations, taking place due to acoustic noise and temperature changes. Hence, the system acts as a self-aligning interferometer and allows for coherent light evolution through a considerable number of roundtrips.

Given an initial 22 ns long pulse, pulse dispersion is negligible (see Equation (3)) and the dynamics in this system are well described by the complex amplitudes $a_{x,y}^{m}$ / $b_{x,y}^{m}$ and $c_{x,y}^{m}$ / $d_{x,y}^{m}$ of the pulses traveling through A and B loop (short/long inner loops) and C and D loop (short/long outer loops), respectively. By interpreting the number of roundtrips m as a discretized time variable and the subscripts (x, y) as the Cartesian position on the mesh lattice displayed in Figure 8, the pulse evolution in the inner loops can then be described by the following equations

$$a_{x,y}^{m} = \frac{1}{\sqrt{2}}\left(c_{x+1,y}^{m-1} + i d_{x+1,y}^{m-1}\right) \exp\left(i\frac{1}{2}\chi\left|c_{x+1,y}^{m-1} + i d_{x+1,y}^{m-1}\right|^2\right) \exp(i\varphi_a), \tag{7}$$

$$b_{x,y}^{m} = \frac{1}{\sqrt{2}}\left(d_{x-1,y}^{m-1} + i c_{x-1,y}^{m-1}\right) \exp\left(i\frac{1}{2}\chi\left|d_{x-1,y}^{m-1} + i c_{x-1,y}^{m-1}\right|^2\right) \exp(i\varphi_b), \tag{8}$$

while in the outer loops by

$$c_{x,y}^{m} = \frac{1}{\sqrt{2}}\left(a_{x,y+1}^{m} + i b_{x,y+1}^{m}\right) \exp\left(i\frac{1}{2}\chi\left|a_{x,y+1}^{m} + i b_{x,y+1}^{m}\right|^2\right) \exp(i\varphi_c), \tag{9}$$

$$d_{x,y}^{m} = \frac{1}{\sqrt{2}}\left(b_{x,y-1}^{m} + i a_{x,y-1}^{m}\right) \exp\left(i\frac{1}{2}\chi\left|b_{x,y-1}^{m} + i a_{x,y-1}^{m}\right|^2\right) \exp(i\varphi_d). \tag{10}$$

New pulses are formed by interference inside the 50/50 couplers as reflected by the first term of Equations (7)-(10). Nonlinear phase modulation is induced by the action of the Kerr nonlinearity in the optical fiber, which is represented by an effective factor χ (see Section 1.6). The third term represents an external phase modulation φ_{a}, φ_{b}, φ_{c}, and φ_{d} imprinted by phase modulators in order to tune the band structure of the system (see Section 1.4) or ensure 2D $\mathcal{PT}$ symmetry (see Section 3.3). Following a 2D quantum walk dynamics [36], [50], an initial single pulse (see Figure 9(a)) injected into the left outer loop (on the center of the lattice $x = 0, y = 0$, see Figure 9(c)) results in a one-dimensional stream of arrival pulses (see Figure 9(b)).

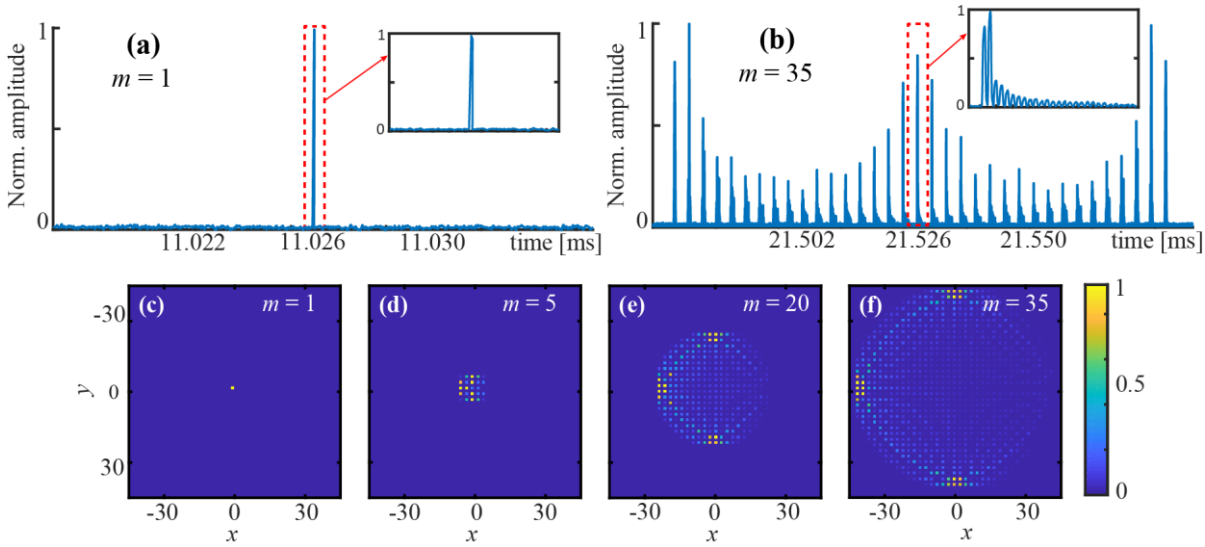

Figure 9: Experimental realization of a 2D light walk for vanishing phase modulation $\boldsymbol{\varphi_0} = \mathbf{0}$. (a) Photodetected signal of the first time step $\boldsymbol{m}$, at which a single pulse is inserted into the left outer loop. (b) Oscilloscope trace of time step $\boldsymbol{m} = \mathbf{35}$. (c)-(f) 2D Light walk for different propagation steps $\boldsymbol{m}$.

Consequently, those pulses perform a 2D light walk ($\varphi_{a,b,c,d} = 0$), which are sampled and attributed to the corresponding 2D mesh lattice positions (see Figure 9(c)-(f)). Note that the expanded inset of Figure 9(a) and (b) (dotted red square) represents all values displayed on the x-axis for $y = 0$, according to Equation (6). This successful emulation of further synthetic dimensions by using a genuine 1D fiber is based on the combination of long- and short-range coupling caused by the inner and outer loop pairs, respectively.

1.4. 1D and 2D Photonic Band Structure

The 1D and 2D photonic mesh lattices created by a coupled-fiber loop scheme exhibit a periodic unit cell (see Figure 2 and Figure 3) and, consequently, eigen-energies of the system yield a dispersion relation based on the Bloch wave theory [54]–[58]. In the linear ($\chi = 0$) and conservative 1D case, the lattice periodicity is two in the transverse and propagation direction (see Figure 2) and Equations (4)-(5) depicts a generalized double time step evolution as

$$u_x^{m+2} = \big(t_{x-1}^{m+1}(t_{x-2}^m u_{x-2}^m + i r_{x-2}^m v_{x-2}^m)e^{i\varphi_u(m)} + i r_{x-1}^{m+1}(t_x^m v_x^m + i r_x^m u_x^m)e^{i\varphi_v(m)}\big)e^{i\varphi_u(m+1)}, \tag{11}$$

$$v_x^{m+2} = \big(t_{x+1}^{m+1}(t_x^m v_x^m + i r_x^m u_x^m)e^{i\varphi_v(m)} + i r_{x+1}^{m+1}(t_{x+2}^m u_{x+2}^m + i r_{x+2}^m v_{x+2}^m)e^{i\varphi_u(m)}\big)e^{i\varphi_v(m+1)}, \tag{12}$$

where transmission and reflection coefficients (t_x^m and r_x^m) and phase modulation (φ_v and φ_u) are considered. First, let consider a Floquet-Bloch ansatz in the form

$$\begin{pmatrix} v_x^m \\ u_x^m \end{pmatrix} = \begin{pmatrix} V \\ U \end{pmatrix} e^{ix\frac{k_x}{2}} e^{im\frac{\theta}{2}}, \tag{13}$$

where $(V, U)^t$ is the eigenvector consisting of two components (amplitude and phase relation between loops v and u), θ is the propagation constant and k_x is the Bloch momentum, inserted into Equations (11)-(12) [22], [47], a dispersion relation yields[1]

$$\cos\theta = C\cos k_x - (1 - C)\sin\varphi_0, \tag{14}$$

where C stands for the splitter ratio of that optical coupler ($C = t^2 = 1 - r^2$), and φ_0 denotes the intensity of a phase modulation applied to the mesh lattice as follows

$$\varphi_v(m) = \begin{cases} -\varphi_0/2, & \text{odd } m \\ +\varphi_0/2, & \text{even } m \end{cases} \quad \text{and}$$

$$\varphi_u(m) = \begin{cases} +\varphi_0/2, & \text{odd } m \\ -\varphi_0/2, & \text{even } m \end{cases}. \tag{15}$$

For the passive case ($\varphi_0 = 0$) and 50/50 splitting ratio ($C = 0.5$), Equation (14) displays a Dirac cone at the edges of the Brillouin zone ($k_x = \pm\pi$), however for any non-vanishing φ_0 the degeneracy is lifted and a gap opens up. A new Dirac cone is formed in the center of the Brillouin zone for $\varphi_0 = \pm\pi$, as shown in Figure 10. In addition, Figure 10(b) exhibits the tuning band structure as a function of splitting ratio $0 \leq C \leq 1$ for phase modulation $\varphi_0 = 0.25\pi$. Furthermore, due to the Floquet-Bloch nature of the system, the passive band structure repeats itself with respect to θ for multiples of 2π [59]. Additionally, the eigenstate $(V, U)^t$ can be manipulated[2] in order to probe a narrow momentum spread excitation, e.g. a broad Gaussian distribution, onto the lower, upper or superposition of both band structure $\theta(k_x)$ [35], [37], [47], [60].

[1] See Appendix A.
[2] See Appendix A.

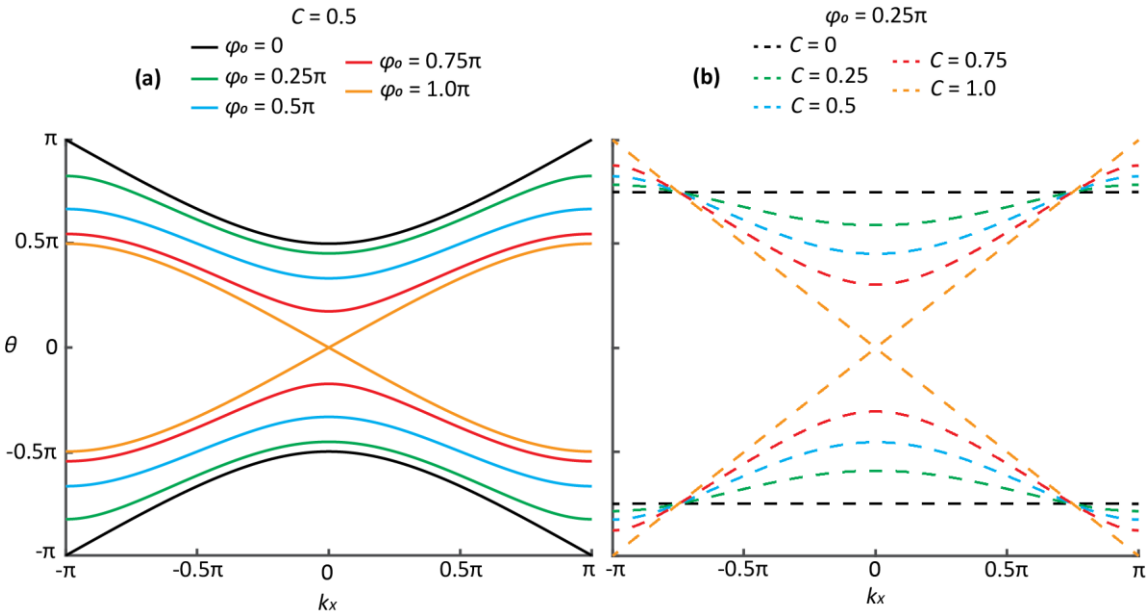

Figure 10: 1D band structure as a function of (a) phase modulation ($\boldsymbol{\varphi_0}$) and (b) splitting ratio ($\boldsymbol{C}$).

The same analogy applies to a 2D photonic mesh lattice, yet it requires a simplification in Equations (7)-(10) to reduce them into two iteration equations. As $a_{x,y}^{m}$ and $b_{x,y}^{m}$ are uniquely determined by $c_{x,y}^{m-1}$ and $d_{x,y}^{m-1}$ and those depend on $a_{x,y}^{m-1}$ and $b_{x,y}^{m-1}$ only, it is possible to replace $c_{x,y}^{m-1}$ and $d_{x,y}^{m-1}$ as

$$a_{x,y}^{m+1} = \frac{1}{2}\left(a_{x-1,y-1}^{m} + ib_{x-1,y-1}^{m} + \left(ib_{x-1,y+1}^{m} - a_{x-1,y+1}^{m}\right)\exp(i(-1)^{m-1}\varphi_0)\right), \tag{16}$$

$$b_{x,y}^{m+1} = \frac{1}{2}\left(\left(b_{x+1,y+1}^{m} + ia_{x+1,y+1}^{m}\right)\exp(i(-1)^{m-1}\varphi_0) + ia_{x+1,y-1}^{m} - b_{x+1,y-1}^{m}\right), \tag{17}$$

where optical couplers are set to a 50/50 splitting ratio and $\varphi_a = \varphi_c = 0$, while φ_b and φ_d consist of a phase modulation as follows

$$\varphi_{b,d}(m) = \begin{cases} -\varphi_0, & \text{odd } m \\ +\varphi_0, & \text{even } m \end{cases}. \tag{18}$$

Furthermore, as in the 1D counterpart, the band structure is calculated by a Floquet-Bloch ansatz [35], [37], [45], [47], [60]

$$\begin{pmatrix} a_{x,y}^{m} \\ b_{x,y}^{m} \end{pmatrix} = \begin{pmatrix} A \\ B \end{pmatrix} e^{i(k_x x + k_y y - \theta m)/2}, \tag{19}$$

where k_x and k_y stand for Bloch momenta in x and y directions, and θ is the propagation constant. In Equation (19), $(A, B)^t$ is the eigenvector consisting of two components, which

describe the amplitude and phase relation between loops A and B from Equations (16) and (17). The structure of the ansatz accounts for the double periodicity of the lattice −i.e. a unit cell contains two points in each direction and two roundtrips are required to reproduce the lattice. Inserting the ansatz into a double-step of the evolution in Equations (16) and (17) produces a dispersion relation[3]

$$\cos(\theta) = \pm\frac{1}{2}\Big(-\frac{1}{2} - \frac{1}{2}\cos(2\varphi_0) - \cos(\varphi_0)\cos(k_x) - \cos(\varphi)\cos(k_y) + \cos(k_x)\cos(k_y)\Big). \tag{20}$$

For any non-vanishing ($\varphi_0 \neq 0$) phase modulation, the degeneracy at the Dirac cone at the edge of the Brillouin zone is lifted and a gap opens up as shown in Figure 11(b)-(f). A new Dirac cone is formed in the center of the Brillouin zone for $\varphi_0 = \pm\pi$ (Figure 11(g)). Similarly, due to the Floquet-Bloch nature of the system, the band structure repeats itself with respect to θ for multiples of 2π.

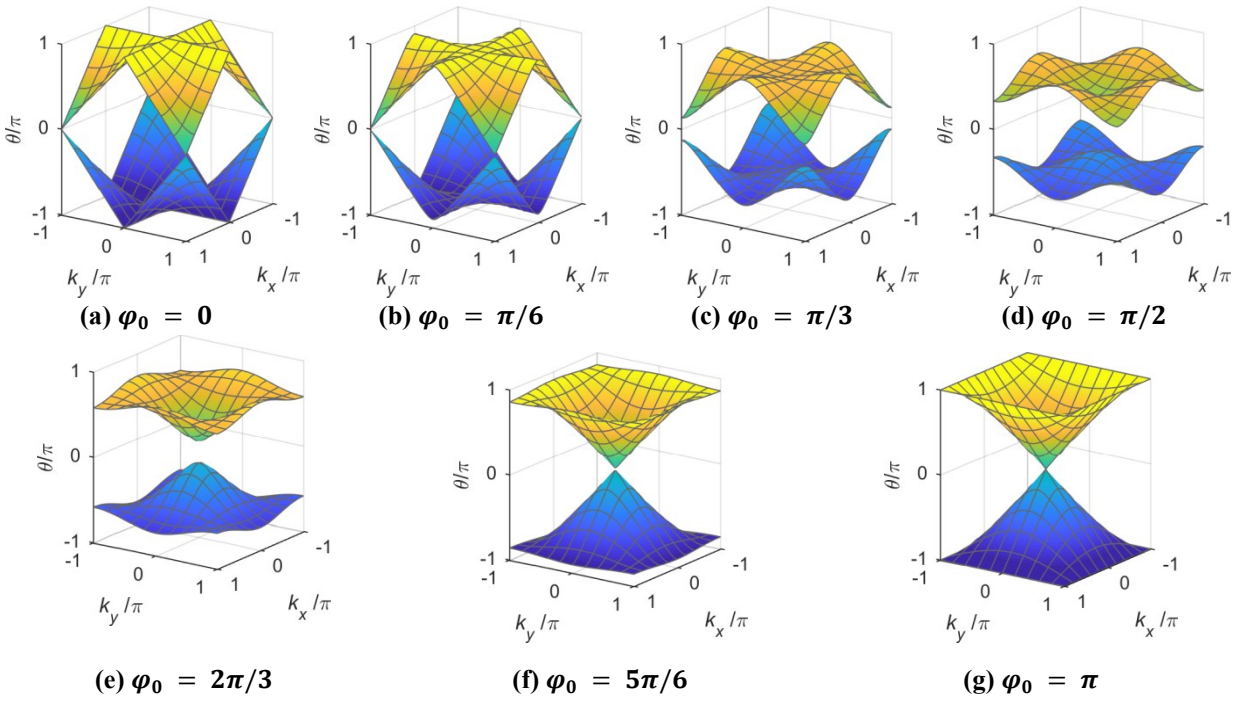

(a) $\boldsymbol{\varphi_0 = 0}$ **(b)** $\boldsymbol{\varphi_0 = \pi/6}$ **(c)** $\boldsymbol{\varphi_0 = \pi/3}$ **(d)** $\boldsymbol{\varphi_0 = \pi/2}$

(e) $\boldsymbol{\varphi_0 = 2\pi/3}$ **(f)** $\boldsymbol{\varphi_0 = 5\pi/6}$ **(g)** $\boldsymbol{\varphi_0 = \pi}$

Figure 11: 2D band structure as a function of the phase modulation $\boldsymbol{\varphi_0}$.

[3] See Appendix B.

1.5. Amplitude, Phase, and Coupling Modulation

Amplitude modulators, such as MZM and AOM, allocated in the 1D and 2D experimental set-up allows for generating broad Gaussian distribution (see Sections 2.1 and 3.1) and gain/loss modulation (see Section 0 and 3.3). They are controlled by a radio frequency (RF) signal from function waveform generators (FWG), in which the transmission ratio (Υ) from AMs varies from 0 (0%) to 1 (100%) according to their characteristic voltage curve [53]. Provided that AMs are set to an idle transmission coefficient of $\Upsilon = \xi$ ($0 < \xi < 1$), a global attenuation is introduced into the fiber paths by $\sqrt{\xi}$ and it is only compensated by an EDFA afterwards in order to restore the quasi-conservative nature of the system. Subsequently, by coarsely varying Υ in the time domain, optical pulses can be amplified ($\Upsilon_x^m > \xi$) or attenuated ($\Upsilon_x^m < \xi$) every roundtrip, from which the maximum gain $G_{\mathrm{MAX}} = 1/\sqrt{\xi}$ is limited by setting $\Upsilon_x^m = 1$.

Similarly, phase modulators enable a variety of physical effects in the photonic mesh lattice [22], [33], [61], such as Kapitza confinement (see Section 0), multimodal photonic mesh lattice (see Section 0), $\mathcal{PT}$ symmetry (see Section 3.3), as well as breaking the degeneracy of the system for opening up a bandgap (see Sections 1.4). In each loop, a PM allows for a linear phase shift (φ_0) based on its characteristic voltage curve [53], in which it is also controlled by an electrical RF signal generated by an FWG.

Additionally, optical couplers which connect the fiber-coupled loops can consist of a fixed splitting ratio, such as 50/50 ratio, or a mechanism of modulating the coupling ratio in order to vary its transmission (t) and reflection (r) coefficients ($t^2 + r^2 = 1$) in the time domain. A variable coupler structurally has an RF input port, similarly to PM and AM, in which the splitting ratio C ($C = t^2 = 1 - r^2$) coarsely vary as a function of the input voltage signal. Normally, VCs commercially available in the market do not present high-speed modulation (~1 MHz) compared to high-speed MZM and PM (~40 GHz), yet it is possible to modulate them in the order of roundtrips (~μs), but not in the range of individual pulse positions.

1.6. Fiber Nonlinearity in 1D and 2D Photonic Mesh Lattices

In the experiment, a nonlinear power-dependent phase shift is acquired by the optical pulses propagating through DCF fibers (type: OFS-HSDK [52]) and SSMF. The long length interaction and the high field concentration in the fiber's core enable significant nonlinear

phase shifts at mW power levels [51]. As silica is inversion-symmetric, its optical nonlinearity is dominated by the third-order susceptibility $\chi^{(3)}$. The experimental parameters were chosen such that they can exclude the influence of any additional nonlinear material response like Raman and Brillouin scattering or acoustic resonance effects on the observed propagation patterns. The power-dependent phase shift is thus a consequence of self-phase modulation in the optical fibers [51].

In the 1D scheme, the nonlinear phase contribution of SSMF is negligible since it has smaller γ and only a few meters are used in the experiments compared to DCF fiber (~4 km). In particular, provided that each path has a fiber spool of DCF, the power-induced nonlinear phase shift is written as

$$\varphi_{NL(1\mathrm{D})} = P_0\left(\gamma_{DCF} L_{DCF}^{eff}\right). \tag{21}$$

$$L^{eff} = \frac{1 - e^{-0.23\alpha L}}{0.23\alpha}, \tag{22}$$

where L^{eff} and α are the effective lengths and absorption coefficients, where the latter is multiplied by a factor 0.23 in Equation (22) to convert it from dB/km into 1/km [52], [53]. P_0 is the power taken within the loop at a certain time step m by the squared absolute value of the pulse amplitude $\left|a_{x,y}^{m}\right|^2$. On the other hand, 2D experiments include the nonlinear phase contribution of SSMF because now the fiber spools consist of ~30 km of SSMF and ~4 km DCF fiber. Despite SSMF has γ smaller (1.1 $(\mathrm{W.km})^{-1}$) than that of the DCF (7 $(\mathrm{W.km})^{-1}$), its cumulative effect should be taken into account due to considerable propagation distances [51]. Therefore, provided that each path has, in sequence, a fiber spool of DCF and SSMF, the power-induced nonlinear phase shift is written as

$$\varphi_{NL(2\mathrm{D})} = P_0\left(\gamma_{DCF} L_{DCF}^{eff} + \gamma_{SMF} L_{SMF}^{eff} e^{-\alpha_{DCF} L_{DCF}}\right). \tag{23}$$

The absorption coefficient ($\alpha_{DCF} = 0.6$ dB/km and $\alpha_{SMF} = 0.2$ dB/km) and the nonlinear parameter $\gamma = 2\pi n_2 / A_{\mathrm{eff}}\lambda$ are fiber-specific parameters [51]. Here, A_{eff} is the effective mode area of the fiber and n_2 is the nonlinear index coefficient. By inserting the fiber parameters used in the experiment into Equations (21)-(23), a nonlinear phase shift of 2π is accumulated at a peak power of about: ~290 mW (1D) and ~157 mW (2D). In numerical simulations, the iteration equations in Equations (4),(5),(7)-(10) consider the nonlinearity as $e^{i\chi|a^2|}$, where $\chi = \gamma L^{eff}$. In addition, according to numerical simulations, the

pulse dynamics are insensitive to a small difference of nonlinearities γ between the loops, which occurs due to experimental imperfections (splice losses, fiber parameters, etc.) Therefore, the evolution equation using in this dissertation, as well as numerical simulations, make the approximation that the effective nonlinearities are equal in both loops [35], [45].

1.7. Coupled-fiber Loop: Historical Milestones

Following previous works in our group [22], [35], [37], [47], [60]–[62], 1D light walk measurement based on the time-multiplexing technique has been improved in several different aspects. Initially, the first investigation in the field was developed by Benjamin Hinrichs in his diploma thesis "*Feldausbreitung in photonischen Netzwerken*" [63], which demonstrated a feasible number of 40 roundtrips possible for propagating through a coupled-fiber loop. Further improvements on the experimental platform accomplished by Alois Regensburger [22], [37], [62], [64] enabled pulse propagation up to 200 roundtrips by using semiconductor optical amplifiers (SOA). Remarkably, telecommunication devices, such as amplitude and phase modulators, were also employed in the system for developing complex fiber networks, such as parity-time symmetric mesh lattice [22], [37], and defect states [62]. Alternatively to SOA, Martin Wimmer proposed a new amplification method in his master thesis "*Nichtlineare Pulsausbreitung in einem optischen Fasernetzwerk*" [65] based on EDFA combined with a co-propagation pump at blue-shifted wavelength. As a result, the maximum number of time steps increased to 1,600 roundtrips. Higher amplification and the resulting peak power combined with nonlinearity enabled the formation of 1D parity-time symmetric solitons [35], Bloch oscillation under parity-time symmetry [66], and optical diametric drive acceleration [61]. M. Wimmer also contributed to Berry curvature measurement from anomalous transport [47] and time-reversed light propagation [67]. Additionally, Arstan Bisianov investigated topological effects in 1D photonic mesh lattice with nonlinearity [68].

To some extent, the present dissertation discusses novel physical phenomena in 1D photonic mesh lattices and an extended scheme for increasing the dimensionality to a 2D photonic mesh lattice. Additional improvements, at this point, on the combination of high-coherent optical pulses and state-of-the-art EDFAs contributed not only to better resolution of pulse interferences at high peak power but also for increasing the synthetic dimensionality of the system and minimizing temperature and polarization drifts during longer data acquisition measurements. This work contributes to 1D Kapitza light confinement [69], optical

thermodynamics in a 1D multimodal photonic mesh lattice, 1D quantum walk with entangled photon-pairs, nonlinear dynamics in 2D photonic mesh lattice [45], and parity-time symmetry in 2D photonic mesh lattice [70].

1.8. Experimental Performance on Coupled-fiber Loops

In this section, two experimental issues, such as acoustic noise and pulse coherence, are discussed and technical solutions to minimize them at an acceptable level are demonstrated. In the 1D experiment, the fiber spools in each loop do not require a long fiber length ($L \approx 4$ km) to synthesize its spatial dimension. However, the extended 2D approach requires approximately 9-times longer fiber spools ($L \approx 35$ km) for tailoring an additional synthetic transverse coordinate (xy-axes). Because the majority of the optical fiber is maintained wrapped in a spool, the acoustic waves can vibrate them in such a way that its length slightly varies in time [71], resulting in considerably small phase variation between optical pulses.

As an illustration, let consider a monotone acoustic tone with a period of $1/f_{\mathrm{ac}}$ applied on two different scenarios of measurements in the coupled-fiber loop having a fiber length of L_1 and L_2 ($L_1 \ll L_2$) (see Figure 12(a)). The measurement time of the first case ($m_{\mathrm{MAX}}.\frac{nL_1}{c} = m_{\mathrm{MAX}}.T_1$, where c is the speed of light and n is the refraction index of silica) is not influenced by external noise oscillations since all pulses practically experience the same noise intensity, whereas the second one ($m_{\mathrm{MAX}}.T_2$) suffers the entire period of that oscillation and thus a train of pulses propagating through this fiber loop receives phase oscillations $\propto 1/f_{\mathrm{ac}}$.

To experimentally illustrate this idea, two cases of a 1D LW are considered in the experiment, of which each loop has: a fiber spool of (1) 4 km (original 1D fiber length) and (2) 34 km (original 2D fiber length). For the first scenario, the phase disturbance is practically imperceptible due to measurement time is smaller than that acoustic noise period, thus all pulses are influenced in the same way during the whole measurement time (see Figure 12(b)). On the other hand, a fiber spool of 34 km results in a longer measurement time, and the chain of pulses experience throughout the experiment the entire phase turbulence (see Figure 12(c)). Therefore, it is used as the latter scenario for optimizing 2D experiments against vibration and acoustic noise. Even though we placed the fiber spools within wooden boxes for both mentioned cases, the latter case demonstrated a poor quality of isolation.

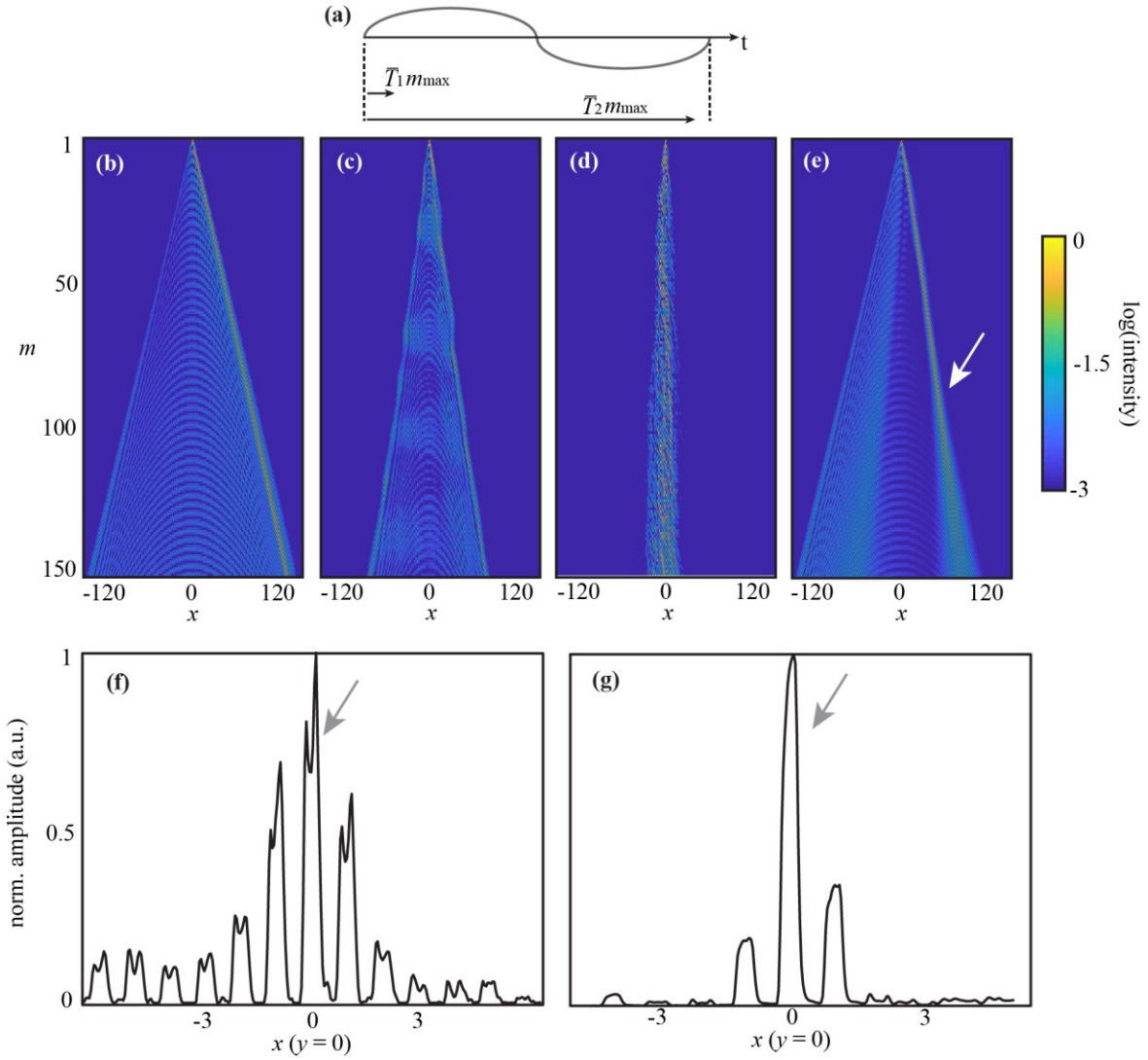

Figure 12: Experimental performance and improvements of a fiber-coupled loop. (a) Two scenarios of measurement time and phase disturbance. (b) 1D light walk without acoustic vibrations. (c) 1D light walk under the influence of phase disturbance caused by acoustic noise. (d) An extreme case of phase disturbance by knocking the fiber spools. (e) Worsening of pulse coherence (interferences) due to poor quality laser source and highly nonlinear phase modulation (indicated by a white arrow). (f) Example of poor pulse coherence (indicated by a grey arrow) at high input power case of a 2D wave collapse. (g) Enhancement of pulse coherence (indicated by a grey arrow) by a high coherent pulse source at high input power case of a 2D wave collapse.

Additionally, to demonstrate an extreme case, if the optical table was knocked/shacked during measurements, high vibrational components distorted the signal so that the phase information between pulses was completely destroyed (see Figure 12(d)). The most feasible technical approach our group used for solving this issue was covering those four fiber spools in wooden boxes and shielding them on soundproofing 3-cm thick acoustic panels (inside and outside) and lining those boxes on the optical table with adhesive low-frequency acoustic foam panels.

Next, pulse coherence was also another technical problem either in 1D and 2D cases. It was first realized in the 1D system [35], from which increasing input power a soliton tends to

form and propagates vertically through the mesh lattice in the ideal case. However, due to the poor coherent time of the initial pulse, this solitonic state was practically destroyed after a few roundtrips (see Figure 12(e)). Similarly, in the 2D case, we recognized the same problem at high input power excitation, in which pulses tend to collapse into a single lattice site and form a bright spike pulse (see Section 0). In this case, provided that pulse coherence is low, nonlinear phase shift combined with a sequence of interferences (at longer time steps) resulted in distorted pulses and poor quality results (see 2D measurements with distorted pulses in the synthetic coordinate x for $y = 0$ in Figure 12(f)). Instead of using a diode laser which has not significant time coherence, our group solved this issue by employing a high-quality laser source (NKT-Photonics Koheras BASIK E15) with narrower linewidth (< 100 Hz) and low phase-noise (3.2 μrad/$\sqrt{\text{Hz}}$/m @ 100Hz) (see results in Figure 12(g) and compare to that previous one in Figure 12(f)).

2. One-dimensional Photonic Mesh Lattice Projects

2.1. Generation of 1D Gaussian Wave Packet as an Initial Distribution

There are two procedures for generating an initial broad distribution: either from an external pulse generator or from an internal phase/amplitude protocol. On one hand, inserting an externally generated wave packet by cutting pulses from a CW signal allows for flexibility, but requires active interferometry stabilization due to mutual phase decoherence. The pulse distance within the chain requires to match the loop difference ΔT, in which inaccuracy in the order of the wavelength has to be compensated by a phase modulator. On the other hand, an amplitude/phase protocol can be used for preparing a broad distribution from an initial seed pulse. This protocol consumes a considerable number of time steps and restricts the amplitude distribution (e.g. exponentially decaying tails of a Gaussian envelope), but it ensures a flat phase distribution and high coherence between pulses since the system acts as a self-aligning interferometer and allows for coherent light evolution. This work focused on creating an initial distribution from a sequence of pulses internally generated by a protocol in order to circumvent technical challenges, such as phase decoherence.

2.1.1. Amplitude Modulation Protocol

Given an initial seed pulse injected into loop v, an alternating amplitude modulation generates a Gaussian distribution by blocking one of the two fiber loops every second roundtrip, which is described by a set of diffusive equations:

$$2v_x^{m+2} = \left(\underbrace{v_{x+2}^m}_{=0} + iu_{x+2}^m + iu_x^m + \underbrace{v_x^m}_{=0} \right) = i(v_{x+2}^m + v_x^m), \tag{24}$$

$$2u_x^{m+2} = \left(u_{x-2}^m + \underbrace{iv_{x-2}^m + iv_x^m}_{=0} + u_x^m \right) = v_{x-2}^m - v_x^m \,, \tag{25}$$

which ensures a vanishing phase after every second roundtrip and forms a Gaussian distribution [64]

$$v_x^m \approx \frac{i^m}{\sqrt{\frac{\pi}{2}m}} e^{-\frac{x^2}{2w^2}}, \tag{26}$$

provided that $m \gg 1$. The width of the distribution w using amplitude modulation protocol grows proportionally to $\sqrt{m}$ since it follows a classical diffusive process [47]. Although its

intensity presents an exponential decay of $e^{-\alpha m}$ due to alternating amplitude modulation, a small amount of amplification in both loops during this process compensates that precipitating loss and yields total power roughly constant [35].

2.1.2. Phase Modulation Protocol

The working principle of generating a broad distribution by phase modulation is based on the fact that compensating the phase difference between loop v and u, every time step m, produces a discretized diffusive equation:

$$v_x^{m+1} = \frac{1}{\sqrt{2}}(v_{x+1}^m + iu_{x+1}^m)e^{i\Phi_v(m,x)} = \frac{1}{\sqrt{2}}\left(v_{x+1}^m + \underbrace{i}_{=1} u_{x+1}^m\right), \tag{27}$$

$$u_x^{m+1} = \frac{1}{\sqrt{2}}(u_{x-1}^m + iv_{x-1}^m)e^{i\Phi_u(m,x)} = \frac{1}{\sqrt{2}}\left(u_{x+1}^m + \underbrace{i}_{=1} v_{x+1}^m\right), \tag{28}$$

where $\Phi_u(m,x)$ and $\Phi_v(m,x)$ denote a spatially-dependent phase profile. Therefore, by numerical simulation, a phase modulation protocol ensures that every time step m, pulses in loop v and u arrive at the optical coupler with zero phase difference

$$\Phi_{\mathrm{u}}(\mathrm{m},\mathrm{x}) = -\tan^{-1}\left(\frac{\Im[\mathrm{u}_\mathrm{x}^\mathrm{m}]}{\Re[\mathrm{u}_\mathrm{x}^\mathrm{m}]}\right), \tag{29}$$

$$\Phi_{\mathrm{v}}(\mathrm{m},\mathrm{x}) = -\tan^{-1}\left(\frac{\Im[\mathrm{v}_\mathrm{x}^\mathrm{m}]}{\Re[\mathrm{v}_\mathrm{x}^\mathrm{m}]}\right), \tag{30}$$

where $\Im[\cdot]$ and $\Re[\cdot]$ represent the imaginary and real parts of the complex vector. As an illustration, a seed pulse injected initially into loop v ($v_{x=0}^{m=0} = 1$) splits into two pulses ($u_{x=-1}^{m=1} = i\frac{1}{\sqrt{2}}$ and $v_{x=1}^{m=1} = \frac{1}{\sqrt{2}}$), in which a phase modulator compensates the phase shift of that first time step, as shown in Figure 13(a) (a circle and star symbol). Subsequently, at every roundtrip m, a phase modulation is applied to loop v and u, following the pattern displayed in Equations (29) and (30) and Figure 13(a) and (b). Provided that $m \gg 1$, a broad distribution having a Gaussian envelope is formed (see Figure 13(d))

$$v_x^m \approx \frac{1}{\sqrt{\pi m}} e^{-\frac{x^2}{2w^2}}, \tag{31}$$

in which the width of the distribution w grows $\propto \sqrt{2m}$ (see Figure 13c) and thus $\sqrt{2}$ faster than that amplitude modulation protocol since the modulation period is reduced by 2. In special, by reducing the coupling ratio C of that optical coupler during this process, wider Gaussian-like distribution is formed

$$v_x^m \approx \frac{1}{\sqrt{2m\frac{\rho}{C}}} e^{-\frac{x^2}{2w^2}}, \tag{32}$$

where $\rho \approx |\theta(k_x = 0)| = \cos^{-1}(2C - 1)$ provided that $m \gg 1$ (see Figure 13(c)).

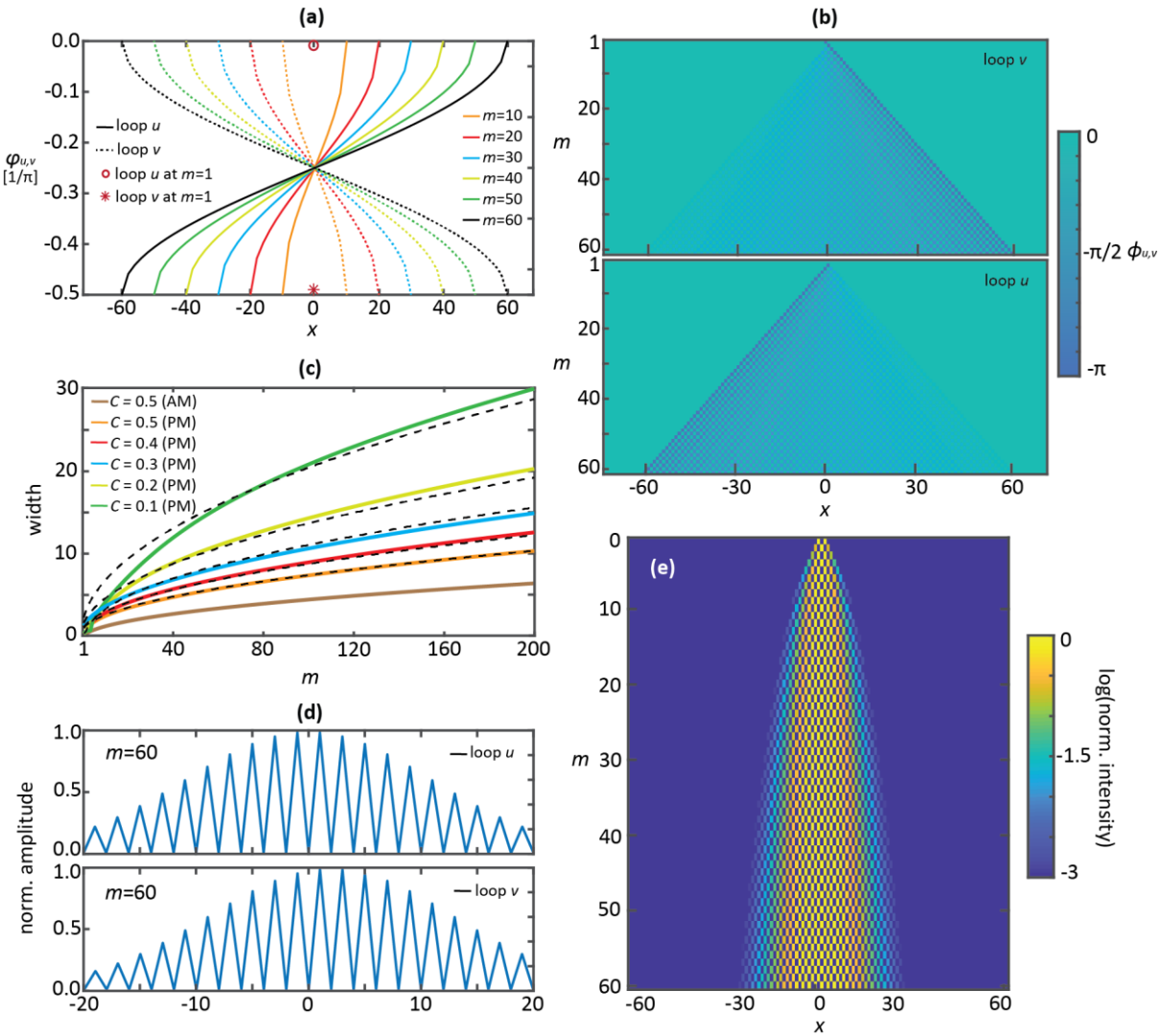

Figure 13: Phase modulation protocol for preparing a wave packet having a Gaussian distribution from an initial seed pulse injected into loop $\boldsymbol{v}$. (a) Phase intensities applied to loop $\boldsymbol{v}$ and $\boldsymbol{u}$ for time steps $\boldsymbol{m} = \mathbf{1}, \mathbf{10}, \mathbf{20}, \mathbf{30}, \mathbf{40}, \mathbf{50}$ and $\mathbf{60}$. (b) Height of the phase modulation protocol as a function of synthetic transverse direction $\boldsymbol{x}$ and time step $\boldsymbol{m}$ up to 60. (c) Width of a Gaussian envelope increases as a function of time steps $\boldsymbol{m}$, where the dashed black lines represent a Gaussian fit curve. AM: amplitude modulator, PM: phase modulation. (d) Normalized amplitude of a Gaussian wave packet at the time step $\boldsymbol{m} = \mathbf{60}$ prepared by using the phase modulation protocol. (e) 2D image of normalized intensities of a Gaussian wave packet prepared by using the phase modulation protocol.

The analytical approximation of Equation (32) is only valid provided that $0.1 \leq C \leq 0.5$ so that the width of the distribution w rapidly increases $\propto \sqrt{m\rho/C}$, as shown in dashed black lines in Figure 13(c). Both techniques (amplitude and phase protocols) exploit diffusive processes accessible in the system from its inherent characteristics. Whereas amplitude protocol produces a Gaussian distribution having a width $\propto \sqrt{m}$ (see brown curve in Figure 13(c)), the phase modulation protocol generates a broader distribution in a shorter period of roundtrips, or even broader if the parameter C is reduced. However, the phase modulation protocol is quite sensible to high input power due to additional phase shift acquired by self-phase modulation since Equations (29) and (30) primarily do not consider nonlinear phase increments.

2.2. Light Confinement via Kapitza Potential

2.2.1. Theoretical Model

In 1951, Kapitza predicted that a classical pendulum pointing upward can be in a stable position when subject to a periodic external torque [72]. Also referred to as a dynamic stabilization effect, Kapitza oscillating potential is an alternative approach of trapping classical or quantum particles that cannot be easily captured by static potentials [73]. Mathematically speaking, the Kapitza effect arises from the influence of fast scales on slow ones, a phenomenon for instance exploited in the Paul trap for particles [74], [75]. The emergence of an effective potential is not restricted to classical dynamics but is also observed in quantum mechanics −i.e. for waves ψ satisfying the Schrödinger equation [76], [77]

$$i\hbar\frac{\partial}{\partial t}\psi = -\frac{\hbar^2}{2M}\frac{\partial^2}{\partial x^2}\psi + \mathcal{U}(x)f(t)\psi, \tag{33}$$

with $f(t+T) = f(t)$. In this case, the Kapitza potential is given by [78]

$$\mathcal{U}_{\mathrm{Kap}}(x) = \frac{T^2}{2M}\left(\frac{\partial \mathcal{U}}{\partial x}\right)^2 \sum_{n\neq 0}\frac{|f_n|}{2n^2\pi^2}, \tag{34}$$

where f_n are the coefficients of the Fourier series of $f(t)$. In the literature, the Kapitza effect has been theoretically predicted in waveguide arrays [73], multilayer stacks [79], periodically modulated waveguides [78], optical resonators [80], twisted anisotropic materials [81], and high-harmonic generation [82]. In special, Kapitza potential was predicted also in photonic structures periodically modulated along the propagation distance z, provided that electromagnetic fields in the paraxial approximation obey the Schrödinger equation with a photonic potential given by $V = -k_0\Delta n$ and an effective mass of $k_0 n_0$, where k_0 denotes the vacuum wavenumber and $\Delta n = n - n_0$ is a small deviation from an average refractive index n_0 [83].

By using 1D photonic mesh lattice, this project models the Kapitza potential like a continuous Pauli-Schrödinger-like equation and experimentally confirms that when the transverse modulation is bell-shaped but with vanishing average along the propagation direction, light undergoes transverse localization, in agreement with the Kapitza stabilization effect [69]. First, let consider the 1D evolution equations in Equations (4) and (5) for a fixed 50/50 splitting ratio ($C = 0.5$). A phase modulation, in agreement with Equation (34), is applied to loop v and u in the form of $\phi(m,x) = f(m)\Phi(x)$, which consists of a sinusoidal

modulation along the propagation direction m and a Gaussian profile along the transverse direction x, written as

$$f(m) = \cos(2\pi m/T'),$$
$$\Phi(x) = Ae^{\left(-\frac{x^2}{2\sigma^2}\right)}, \tag{35}$$

where T', A and σ stands for oscillation period, height, and width of the potential, respectively (see Figure 14). The discrete set of Equations (4) and (5) in the absence of any phase modulation (i.e. $\phi(m,x) = 0$) results in pseudo-spinors $\psi_x^m = (v_x^m; u_x^m)$ decomposed into eigenstates as $\psi_x^m = \psi_{\text{mode}} e^{-i(\theta m - k_x)}$. As demonstrated in Equation (14), respective eigenvalues or quasi-energies θ are arranged in two mirror-symmetric bands separated by a gap given by $\cos(\theta) = \cos(k_x)/\sqrt{2}$ (see Figure 10(a)). In the case of the band edges, i.e. for $k_x = 0$, the two modes $\psi_{\text{mode}} = \psi_\pm = (1; \pm 1)/\sqrt{2}$ correspond to diagonal and anti-diagonal pseudo-polarizations. To apply Kapitza's concept, Equations (4) and (5) are modeled with the continuous Schrödinger equation in Equation (33). To this end, it is assumed a broad excitation of a single band with flat phase $\psi_{\text{x}}^{\text{m}} = \psi(m,x)\psi_\pm$ (see Section 2.1), resulting in a spectrum centered on the Γ point (k_x = 0). For such excitation, it restricts the model to an expansion of the band structure up to the second-order, such as

$$\theta(k_x) = \pm\left(\frac{\pi}{4} + \frac{{k_x}^2}{2}\right), \tag{36}$$

where the signs are determined by the chosen dispersion band −i.e. lower (defocusing) or upper (focusing) bands.

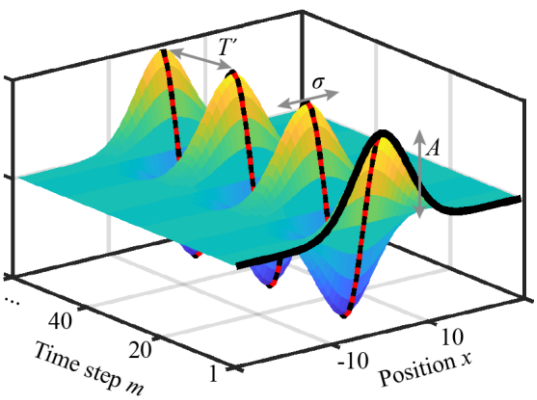

Figure 14: Sketch of the external oscillating phase modulation $\boldsymbol{\varphi(m,x)}$ for light confinement as a continuous function of space ($\boldsymbol{x}$) and propagation coordinate ($\boldsymbol{m}$), featuring three free parameters $\boldsymbol{A}$, $\boldsymbol{\sigma}$ and $\boldsymbol{T'}$.

Importantly, assuming that variations between subsequent roundtrips in Equation (35) are small, m and x are now regarded as continuous quasi-time and space, respectively.Still, a respective evolution equation must reproduce the band structure approximated by Equation (36) and in case of smooth changes of modulation should induce a phase evolution similar to that in Equations (4) and (5), defined as

$$i\frac{\partial}{\partial m}\psi = \pm\left(\frac{\pi}{4} - \frac{1}{2}\frac{\partial^2}{\partial x^2}\right)\psi + f(m)\Phi(x)\psi. \tag{37}$$

The constant quasi-energy of $\pm\pi/4$ in Equation (37) has no significant effect except for a trivial phase shift. A change of sign in front of the transverse derivative with respect to x caused by a band dependent effective mass, which is compensated by the complex conjugation of the whole Equation (37) and a sign flip of the effective potential $f(m)\Phi(x)$. Based on these considerations, a comparison between Equation (37) and Equation (33) allows for identifying the effective Kapitza potential by setting $\hbar$ and M to 1 as

$$\Phi_{\mathrm{Kap}}(x) = \frac{T'^2}{16\pi^2}\left(\frac{\partial\Phi(x)}{\partial x}\right)^2. \tag{38}$$

The effective Kapitza potential $\Phi_{\mathrm{Kap}}(x)$ for the phase modulation provided by Equation (35) is depicted in Figure 15 (dashed blue lines) for two different sets of parameters. The shape of $\Phi_{\mathrm{Kap}}(x)$ is an inverted W and, given that we are following the quantum mechanical convention in accordance with Equation (33), the field is attracted by regions where the potential is lower. Strictly speaking, no bound states are supported by this effective potential because its minimum value is equal to $\lim_{|x|\to\infty}\Phi_{\mathrm{Kap}}(x) = 0$ [84], but for realistic propagation distances the two potential walls are high enough to confine the field. Interesting to note that Equation (38) is independent of the sign of the original potential and as well as of the chosen band. We can thus expect similar effects including spatial confinement for both bands having opposite effective masses [61], which would not be possible for a conventional potential. Although the stationary component of the quasi-mode is governed by the longitudinally constant potential given by Equation (38), minor differences arise when the higher harmonics of the field are considered [78], [85].

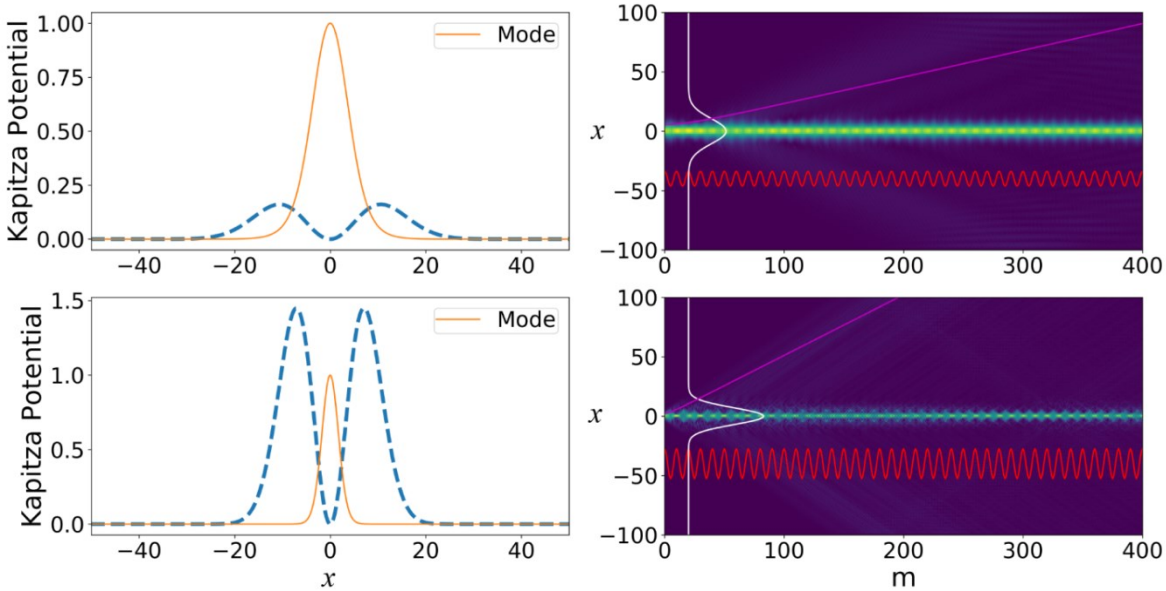

Figure 15: Simulated quasi-mode propagation for $\boldsymbol{T' = 20}$. Left column: profile of the effective potential given by Equation (38) (blue dashed line) and the corresponding quasi-mode (orange solid line) versus synthetic coordinate x. Right column: optical propagation computed via Equations (4) and (5) when the quasi-mode showed in the left column is launched at $\boldsymbol{m = 0}$. White, magenta, and red solid lines are the instantaneous potential $\boldsymbol{\Phi}$ versus $\boldsymbol{x}$, the beam width for vanishing phase modulation $\boldsymbol{\varphi = 0}$ versus $\boldsymbol{m}$, and the instantaneous potential variation versus m, respectively. The parameters of the potential are ($\boldsymbol{A = 2\pi, \sigma = 15}$) and ($\boldsymbol{A = 4\pi, \sigma = 10}$) for top and bottom rows, respectively.

The numerical simulation depicts the propagation of quasi-modes for the original discrete system ruled by Equations (4) and (5) stemming from the effective potential in Equation (38) (dashed blue lines in Figure 15). The inverted W-shaped potential computed from Equation (38) supports only leaky modes −i.e. trapped modes undergoing decay along propagation due to the coupling with radiation modes [84]. To compute the leaky modes of this structure, it is considered only the central lobe of the potential, artificially flattening the potential for $|x|$ larger than the positions corresponding to the potential maxima [78]. Such an approximation is accurate if the calculated quasi-mode is confined between the two lobes. Otherwise, the leaky mode will be subject to strong losses, inhibiting field trapping along the synthetic coordinate x [78]. Figure 15 shows the computed quasi-modes for two sets of parameters where this approximation holds valid −e.i. quasi-guided modes exist. Next, computed profiles are used as the initial condition for the discrete field (u, v) propagating according to Equations (4) and (5). As shown in Figure 15, the beam is trapped around $x = 0$ as predicted, with minimal losses occurring both at the input interface and during propagation. Furthermore, the confined beam propagating is breathing synchronously with the phase modulation, in agreement with the Bloch-Floquet theory.

2.2.2. Experimental Results

First, let us consider a broad excitation by promoting a selective population within the center ($k_x = 0$) of the upper band. For this particular project, a broad Gaussian distribution is generated by using an amplitude modulation protocol (see Section 2.1.1). Given a Gaussian envelope $\psi(m = 0, x) = G_0 \exp\left(-\frac{x^2}{2w_0^2}\right)$ (see green dotted curve in Figure 16(b)), where both the field amplitude (G_0) and width along x (w_0, defined via the $1/e$ drop in intensity) can be tuned.

Without any phase modulation (see Figure 16(a)), a Gaussian wave packet experiences linear diffraction, and its width w_0 is doubled after a certain number of roundtrips given by the effective Rayleigh distance $L_D \approx w_0^2$. For a proper periodical modulation, diffraction is suppressed and the field at $m = 200$ has still the same size as the input distribution, see Figure 16(b). Light confinement can be clearly observed in Figure 16(c), where the beam width does not increase along propagation due to the Kapitza effect. In Figure 16, the field confinement is demonstrated for one periodic potential, after fixing the width σ and the amplitude A.

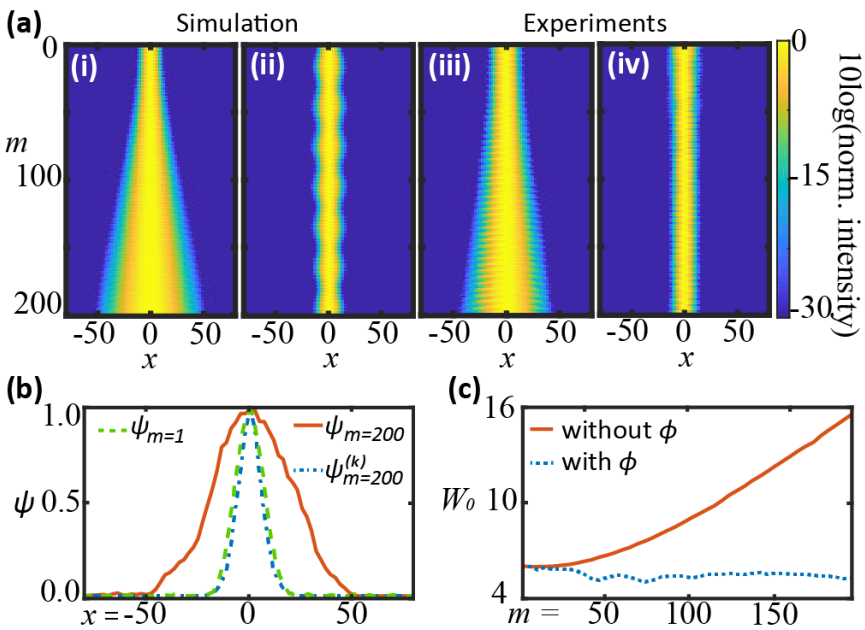

Figure 16: Light confinement via the Kapitza effect. (a) Simulation and experimental results of the propagation of a wave packet without (i and iii) and with (ii and iv) the periodic phase potential $\boldsymbol{\phi}$ given by Equation (35), with $\boldsymbol{T' = 26}$, $\boldsymbol{A = \pi}$, and $\boldsymbol{\sigma = 18}$. The plots are in algorithmic scale, with the intensity being normalized with respect to the actual maximum. (b) Profile $|\boldsymbol{\psi(m, x)}|$ (peak normalized to unity, linear scale) versus $\boldsymbol{x}$ for the initial field distribution (green dashed line, $\boldsymbol{\psi_{m=1}}$), and for fields at $\boldsymbol{m = 200}$ without potential (red line, $\boldsymbol{\psi_{m=200}}$) or in the presence of a confining potential (blue line, $\boldsymbol{\psi^{(k)}_{m=200}}$). (c) Wave transverse width versus m without (red line, pure diffraction) and with (blue dotted line, confined field) the periodic potential $\boldsymbol{\phi}$.

Next, numerical simulation computes which values of the parameters in Equation (35) Kapitza confinement will occur. Systematically, two main requirements have to be fulfilled to achieve light confinement utilizing a periodic phase modulation [78]. First, the period T' of the temporal modulation (i.e. along propagation direction m) has to be smaller than the diffraction length L_D of a given wave packet: if this condition is not satisfied, higher-order terms in the Floquet expansion of the quasi-mode cannot be neglected anymore. Physically speaking, the field spreading during the repelling half-period of the instantaneous potential is too strong to be compensated during the following half period where the potential is confining. Second, the potential width σ should not be too small: in fact, too narrow central lobes imply a significant spatial overlap between the quasi-mode and the lateral lobes, thus inhibiting confinement due to the high radiation losses.

To quantitatively investigate the confinement degree as a function of A, σ and T', we determined the amount of guided power P_c remaining after 200 steps of propagation as the integral of the intensity over a region of $4w_0$ around $x = 0$. Consequently, a guiding efficiency $\eta = P_c/P_{\text{in}}$ is determined as the ratio between the guided power P_c and the launched power P_{in} in that region as

$$\eta = \frac{P_c}{P_{\text{in}}} = \frac{\sum_{x=-2w_0}^{2w_0}(|u_x^{m=200}|^2 + |v_x^{m=200}|^2)}{\sum_{x=-2w_0}^{2w_0}(|u_x^{m=1}|^2 + |v_x^{m=1}|^2)}, \tag{39}$$

where $\eta = 1$ means that all the power is confined around $x = 0$. The numerically computed η is plotted in the logarithmic scale in Figure 17. A Gaussian wave packet with a width $w_0 \approx 7$ ($L_D \approx 49$) is considered as initial input. In agreement with the first requirement, the field confinement worsens as the modulation period T' becomes comparable with the Rayleigh distance of the input beam (compare Figure 17(a)-(d)). Concerning the second condition, P_c increases as the potential becomes wider: in fact, in each panel η tends to unity moving from left to right −i.e. when σ increases.

Furthermore, Figure 17(a)-(d) shows how larger amplitudes of the potential A improve the confinement, in accordance with Equation (38). For instance, when $T' = 26$ (see Figure 17(a)) for weak ($A < \pi$) but wide ($\sigma > 20$) phase modulation, the wave packet experiences weak confinement and power is radiated away, yielding linear spreading (see Figure 17 inset (i)). In contrast, for $\Phi(x)$ stronger (large A) and narrower (smaller σ), the wave is strongly focused owing to the mismatch between the input waist and the width of the fundamental mode, resulting in a strong width variation along m (see Figure 17 inset (iii)).

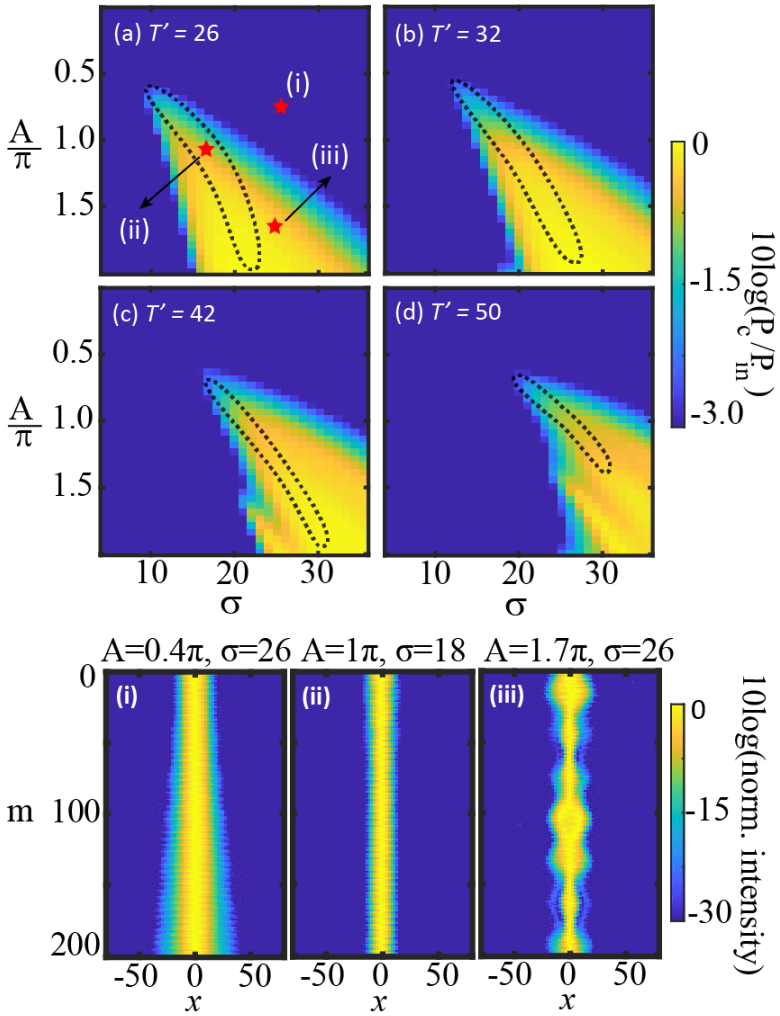

Figure 17: Numerically determined regions of light confinement as a function of $\boldsymbol{A}$ and $\boldsymbol{\sigma}$ for oscillation periods $\boldsymbol{T'}$ of (a) 26, (b) 32, (c) 42, and (d) 50, computed via Equations (3),(4). The input is a Gaussian pulse with $\boldsymbol{W_0} = \boldsymbol{7}$. $\boldsymbol{P_{in}}$ is the total initial power. Dotted lines encircle the parameter region where a quasi-shape-preserving beam is excited; in these regions, the variation of the amplitude and width of the field distribution are lower than 10%. Bottom row: experimental verification of light propagation when (i) no confinement occurs, (ii) mono-modal quasi-guiding is achieved, and (iii) the multi-modal regime (parameters correspond to red stars in (a)) is reached.

Thus, although the power is localized around the origin, the field can undergo strong variations while propagating. In fact, the effective potential can be multimodal when the central lobe is deep enough and not too narrow −i.e. for large A and for σ larger than the fundamental mode itself. Accordingly, the simultaneous presence of more than one mode yields additional breathing due to intermodal interference. To address intermodal interference, in Figure 17(a)-(d) the regions where the localized field (specifically, its width σ and amplitude A) barely varies with respect to the initial input are bound by the dotted black lines. To confirm the experimental results, light propagation is tested in three different points, each of them corresponding to a different propagation regime. It is selected a potential too weak to induce confinement (Figure 17 inset (i)), nearly-invariant propagation in the mono-

modal regime (Figure 17 inset (ii)), and confinement in the presence of multiple quasi-modes (Figure 17 inset (iii)).

2.3. Optical Thermodynamics in Nonlinear 1D Multimodal Mesh Lattice

Recently, there has been a resurgence of interest in nonlinear multimode optical systems [86]–[91]. While the role of thermodynamics in optics has a long and rich history, it has so far been primarily confined to black-body settings and other open systems, which allows for heat exchange with their surroundings [92]. Quite recently, the prospect of observing an intriguing class of all-optical thermodynamic phenomena based solely on photon-photon multimodal interactions has been put forward [87], where the complex nonlinear response of highly multimode optical systems has attracted considerable attention [93], [94]. To an extent, what has motivated this interest is a quest for high-power optical sources that have been enabled by a sequence of new developments in multimode technologies related to both guided-wave structures [95], [96] and photonic cavities [97], [98]. As lately indicated in several studies, the action of nonlinearity in such multimodal arrangements can lead to a host of novel effects that have no counterpart whatsoever in single-mode settings [99]–[101]. Possible examples include geometric parametric instabilities [100], [102], spatiotemporal mode-locking [103], [104], new Cherenkov dispersive wave lines [105] and supercontinuum generation [106], [107], to mention a few.

At the same time, a new set of theoretical challenges has been arisen in terms of understanding and predicting the complex nonlinear response of such systems −especially when hundreds or thousands of modes are involved [108]. Clearly, to harness this class of configurations, one has to address firstly several crucial issues associated with the power distribution and exchange among all possible modes [91], [109]. Lately, a self-consistent optical thermodynamic theory has been considered capable of describing such complex phenomena utilizing thermodynamics [86], [91]. By deploying entropic arguments, this formalism can predict several intriguing processes that are uniquely relevant to such large-scale nonlinear optical multimodal systems. Among these processes is the thermalization towards a Rayleigh-Jeans distribution that explains the effect of beam self-cleaning [93], [94] −a process that has been so far remained poorly understood. Resulting quasi-thermal distributions are uniquely characterized by chemical potentials μ and temperatures T, which in principle can be either positive or negative [86], [87]. In addition, this theory suggests the prospect of isentropic (adiabatic) expansions/compressions [87] along with irreversible Joule expansions. These elementary mechanisms can, in turn, be judiciously leveraged to implement thermodynamic Carnot cycles [87] for either heating or cooling an optical system [86] −i.e. aspects that could be useful for improving the brightness of optical sources. Yet, as

of now, there has been no experimental confirmation of such unusual behavior in the optical domain.

Here, we demonstrate, for the first time, a set of archetypical optical thermodynamic processes in a nonlinear multimodal photonic mesh lattice – all unfolding at temperatures that have nothing to do with the actual thermal environment [110]. These include optical thermalization at both positive and negative temperatures, isentropic expansions and compressions as well as Joule photon-gas expansion. In addition to shedding light on fundamental issues associated with the physics of complex nonlinear highly multimode systems, these results also open up new perspectives to realize a novel class of all-optical thermal engines based on entropic principles.

2.3.1. Thermodynamic Conditions

In general, nonlinear multimode optical waveguides support a finite number of M bound states, called modes, which propagate along the axial direction z. Relevant configurations can be continuous, such as a strip of an extended layer confined between cladding ones [111], or discrete, such as multicore optical fibers [112] or waveguide arrays [95]. Despite modeling differences, all configurations present eigenmodes associated with a particular propagation constant, determined via the solution of an eigenvalue problem [96]. In the lossless case, optical power (P) is conserved, and also the system's Hamiltonian remains constant provided that system parameters do not change. The latter one consists of linear (H_{L}) and nonlinear (H_{NL}) components, which continuously exchange their energies during a nonlinear propagation ($H = H_{\mathrm{L}} + H_{\mathrm{NL}}$). Here, we assume optical thermodynamic effects utilizing weak nonlinearities causing an adiabatic exchange of power between modes. In this case, the Hamiltonian is dominated by the linear contribution ($H \approx H_{\mathrm{L}}$) and the conserved internal energy (U) of a multimodal system is defined as $U = -H_{\mathrm{L}}$. This approximation is analogous to a "diluted gas of particles approach" whose internal energy is dominated by its kinetic part [87], [91]. In contrast, high nonlinearity enables solitonic structures to form, a situation for which this approximation is not valid anymore.

The system's eigenmodes are described by their occupation $|c_k|^2$, where c_k stands for the complex coefficients of the field distribution, and propagation constants θ_k. Additionally, as a conserved system, total power and internal energy are completely determined by initial excitation conditions and thus they are written as $P = \sum |c_k|^2$ and $U = -\sum \theta_k |c_k|^2$, respectively. These thermodynamical variables, such as P, U, M, and the θ_k are connected

with each other by the optical temperature T and the chemical potential μ associated to the system [91] by the relation

$$U - \mu P = MT, \tag{40}$$

which involves the number of modes M and their propagation constants θ_k, and thus Equation (40) is analogous to that of an ideal gas [87] −e.g. $pV = Nk_{\mathrm{B}}T$ [110]. The extensive variables in Equation (40) can be used to determine both T and μ of a nonlinear multimodal system at a thermal equilibrium since P and U are initially specified. In such an arrangement, the system reaches thermal equilibrium by maximizing its entropy and forcing its modal occupancy to follow a Rayleigh-Jeans distribution

$$|c_k|^2 = -\frac{\alpha T}{\theta_k + \mu} \ , \tag{41}$$

where α is simply a coefficient used for convenience.

2.3.2. 1D multimodal Mesh Lattice and Initial State Excitation

Similar to Equations (4) and (5), a 1D photonic mesh lattice with finite positions can be modeled, in the linear ($\chi \approx 0$) case, by the following set of equations:

$$u_x^{m+1} = (t_x^m u_x^m + i r_x^m v_x^m) \exp(i\varphi_0), \tag{42}$$

$$v_x^{m+1} = (t_{x-1}^m v_{x-1}^m + i r_{x-1}^m u_{x-1}^m), \tag{43}$$

$$u_x^{m+2} = (t_{x+1}^{m+1} u_{x+1}^{m+1} + i r_{x+1}^{m+1} v_{x+1}^{m+1}) \exp(-i\varphi_0), \tag{44}$$

$$v_x^{m+2} = (t_x^{m+1} v_x^{m+1} + i r_x^{m+1} u_x^{m+1}), \tag{45}$$

where φ_0 is the phase shift applied by phase modulators, and t and r are transmission and reflection coefficients of the optical coupler from Equation (2). Given that the periodicity of the mesh lattice is two, a pulse only returns to its starting point after two roundtrips and, consequently, a full period of mode evolution requires two roundtrips.

A finite number of modes M in the system is achieved by truncating the mesh lattice in Equations (42)-(45) at predefined reflective boundaries ($r = 1; t = 0$). Therefore, the first and last elements is set to $t_{x=-\frac{N}{2}} = t_{x=\frac{N}{2}} = 0$ and $r_{x=-\frac{N}{2}} = r_{x=\frac{N}{2}} = 1$ in order to reflect pulses back to the mesh lattice, where N represents the lattice size. Altogether, the matrix of

eigenmodes Ψ ($2N+2$ elements) of a given lattice configuration based on φ_0 and t/r is determined by calculating the eigenvalues of the propagating matrix $\mathcal{M}$ of Equations (42)-(45) from time step m to $m+2$

$$[\Psi_k, \theta_k] = \mathrm{eig}\left(\widehat{\mathcal{M}}(\varphi_0, C)\right), \tag{46}$$

where C is the splitting ratio of the optical coupler ($C = t^2 = 1 - r^2$) and θ_k is the propagation constant from which each eigenmode is occupied. Therefore, each eigenmode is composed of a set of complex vector $(V, U)^{-1}$ denoting a stationary field distribution in loop v (V) and u (U) and it replicates itself after two roundtrips except for a trivial phase ($e^{i\theta_k}$).

Figure 18 shows the distribution of eigenvalues θ_k as a function of phase modulation (φ_0) and splitting ratio (C). Each eigenmode derived from Equation (46) possesses a propagation constant, which converges to a Floquet band structure for an infinite system (see Section 1.2 and Figure 10). In addition to phase modulation, C can be tuned by reducing or increasing in the coupling strength, resulting in compressing or extending of the eigenmodes over the propagation constant θ span (compare Figure 18(a) for $C = 0.5$ (purple), 0.3 (yellow) and 0.1 (green) for $\varphi_0 = \pi$). Additionally, the number of system's eigenmodes is directly proportional to the mesh lattice size (see Figure 18(b) for $N = 10$ and 20).

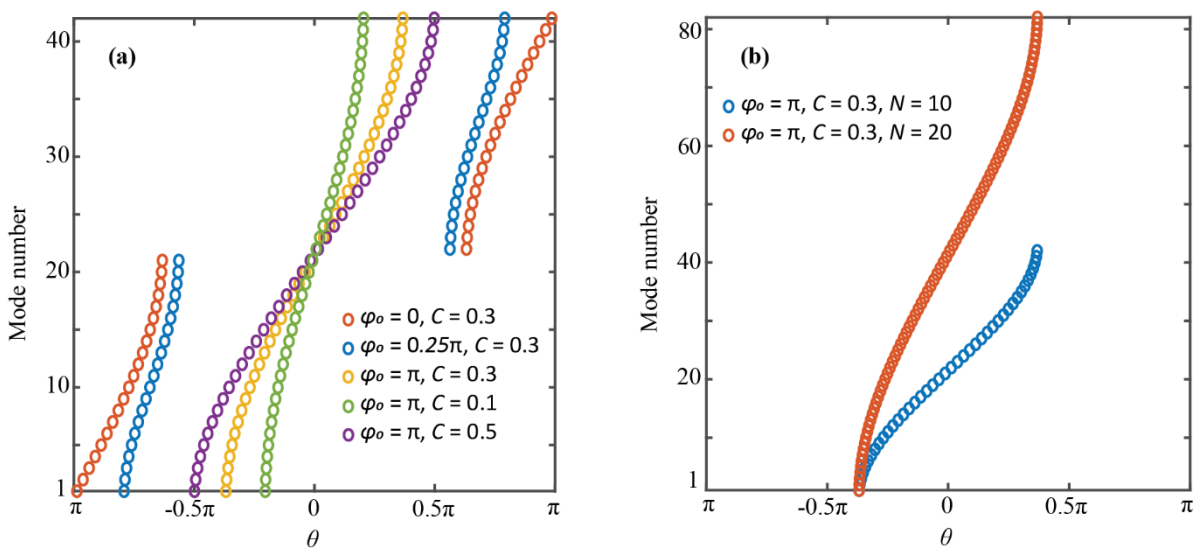

Figure 18: (a) Eigenmodes distribution as a function of phase modulation $\boldsymbol{\varphi_0}$ and coupling ratio $\boldsymbol{C}$ for a finite mesh lattice of **21** positions. (b) Mode distribution in case of increasing the number of lattice positions of **21** (blue) to **41** (red).

In such a system, the modal occupancy $|c_k|^2$ is obtained via

$$|c_k^m|^2 = |\Psi_k^{-1} * \psi^m|^2. \tag{47}$$

where ψ^m denotes the complex amplitude distribution in loop v and u at the time step m

$$\psi^m = \left[v_{x=-\frac{N}{2}}^m \quad \cdots \quad v_{x=0}^m \quad \cdots \quad v_{x=\frac{N}{2}}^m \quad u_{x=-\frac{N}{2}}^m \quad \cdots \quad u_{x=0}^m \quad \cdots \quad u_{x=\frac{N}{2}}^m\right]^{-1}. \tag{48}$$

Since Equation (46) yields the eigenmodes of the system, it is possible to select each one individually or assemble them in a multimodal arrangement for propagating through the photonic mesh lattice. In order to prepare the initial state, let consider an initial state $\psi^{m=1}$ as a superposition of a given set of eigenmodes of Equation (48) as follows

$$\psi^{m=1} = \sum_{k=1}^{2N+2} s_k \Psi_k = \binom{V'}{U'}, \tag{49}$$

where s_k denotes a complex number with an absolute value of either 0 or 1 (mode empty or occupied) and a random phase $e^{i2\pi R}$, in which R is a uniformly distributed pseudorandom number on the open interval [0,1].

Experimentally, the initial state $\psi^{m=1}$ reproduced in Equation (49) is prepared inside the fiber-coupled loop for avoiding any phase decoherence between optical pulses (see Section 2.1). First, a broad Gaussian distribution with a flat phase is generated by using the phase modulation protocol (see Section 2.1.2) during 60 roundtrips. At $m = 60$, the prepared Gaussian distribution (see red dashed line in Figure 19(a)) is truncated to finite positions (i.e. $N + 1$) and shaped to the initial distribution $\psi^{m=1}$ by judiciously amplifying or attenuating (see Figure 19(b)) each pulse in loop v (V') and u (U')

$$\Lambda_v(x) = \frac{|V'|_x}{|v|_x^{m=60}} \text{ and} \tag{50}$$

$$\Lambda_u(x) = \frac{|U'|_x}{|u|_x^{m=60}}. \tag{51}$$

However, the amount of amplification accessible in the experiments relies on the idle transmission ratio (Υ) from AMs (see Section 1.5). For lower values of Υ, a net gain $\Lambda_{v,u}$ is bigger but requires a higher amount of EDFA amplification for restoring the conservative quasi-energy of the system. Usually, the EDFAs produce more ASE noise for higher

amplification rates, which worsens the signal-to-noise ratio (SNR). Consequently, Υ is chosen at the best value of 0.5 [35], in which EDFA compensates its 3dB loss at a reasonable noise figure whereas maximum net gain $\Lambda_{v,u}$ goes up to 2.

Please, note that it is hard to generate modes that have high amplitudes on their edges due to the exponentially decaying tails of a Gaussian distribution and $\Lambda_{v,u}$ is practically limited to a certain value. Thus, a pre-selection of mode distributions, which can be generated in the experiments, is evaluated as

$$\psi^{m=1} \text{ is valid if} \begin{cases} 0 < \Lambda_v(x) < \sqrt{2} \\ 0 < \Lambda_u(x) < \sqrt{2} \end{cases}. \tag{52}$$

As an illustration, the blue curve in Figure 19(a) depicts a specific mode $\psi^{m=1}$ in loop v to be excited in the mesh lattice. The amplitude modulation Λ_v required to amplify or attenuate each position x is shown in Figure 19(b), where an amplification and attenuation, for instance, of 1.4 and 0.5 are applied to the positions $x = -8$ and 0, respectively. Afterward, a phase modulation is applied to match the complex amplitudes of $\psi^{m=1}$ (see Figure 19(c)). By numerical simulation, a large number of $\psi^{m=1}$ was randomly generated ($n \approx 100{,}000$ ensembles) from Equation (49) (with the same modal occupancy) and analyzed by Equation (50)-(52), from which a few $\psi^{m=1}$ were selected for the set of measurement ensembles to be used in the experiments ($n \approx 50$).

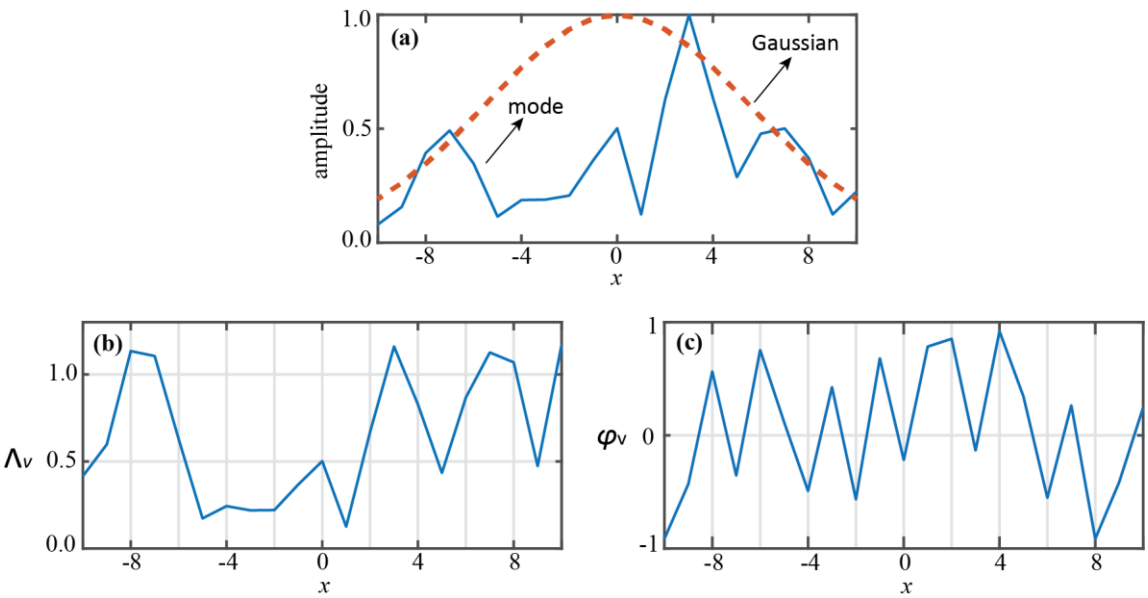

Figure 19: Initial excitation prepared from a Gaussian distribution. (a) Truncated Gaussian distribution (red dashed line) generated in the experiments ($\boldsymbol{w} \approx \mathbf{6}$) and an example of a resulting mode distribution $\boldsymbol{\psi}^{\boldsymbol{m=1}}$(blue color; only loop v is displayed). (b) Amplitude and (c) phase modulation applied to that Gaussian to generate the $\boldsymbol{\psi}^{\boldsymbol{m=1}}$ selected to the measurement set.

2.3.3. Nonlinear Interaction, Hamiltonian and Entropy

In the linear case ($\chi \approx 0$), modes propagate through the mesh lattice without exchanging energy, and the initial modal occupancy $|c_k^{m=1}|^2$ is preserved for any time step m. On the other hand, a weakly nonlinear regime ($\chi > 0$) allows for the adiabatic exchange of energy between modes. Following Equations (4) and (5), we introduce a power-dependent nonlinear phase shift $\varphi_{\mathrm{NL}} = e^{i\chi|\psi^m|^2}$. For a weak nonlinearity, $H_{\mathrm{NL}} \approx 0$ and the internal energy U is still determined by the linear Hamiltonian as

$$U(m) \approx -H_{\mathrm{L}}(m) = -\sum_{k=1}^{2N+2} (\theta_k * |c_k^m|^2). \tag{53}$$

Additionally, the entropy Ω of the system is estimated as

$$\Omega(m) = \sum_{k=1}^{2N+2} ln\left(\overline{|c_k^m|^2}\right), \tag{54}$$

where $\overline{|c_k^m|^2}$ is the mean value of $|c_k^m|^2$ determined by evaluating n measurement ensembles. Thus, U and Ω are used as indicators to verify if the initial modal occupancy reached its thermodynamic equilibrium [86], [87]. At this point, Ω reaches its maximum value [90] since it is analogously governed by the second law of thermodynamics [110].

2.3.4. Nonlinearity Estimation and Phase Recovery

In numerical simulations, the total power $E_T(m) = \sum(|c_k^m|^2) = \sum(|v_x^m|^2 + |u_x^m|^2)$ is fixed to unity and nonlinearity χ is a variable unconstrained. On the other hand, in the experiments, χ has a fixed value and is based on the system's fiber nonlinearity (see Section 1.6), whereas the only quantity accessible to tune the system from quasi-linear ($\varphi_{NL} \approx 0$) to nonlinear ($\varphi_{NL} > 0$) is the initial optical power [35].

From Equation (49), each eigenmode of the system comprises a vector $(V, U)^{-1}$ of complex numbers (i.e. by an absolute value ($|v_x|$ and $|u_x|$) and angle argument ($\exp(i\phi_v)$ and $\exp(i\phi_u)$). In the experiments, optical pulses are quantified by their intensities after photodetection in loops v and u. Hence, the phase information $\exp(i\phi_{v,u})$ has to be estimated by a post-processing algorithm to measure the modal occupancy in Equation (47).

First, the photodetected optical intensities are organized in matrices as follows

$$I_v(m,x) = |v_x^m|^2,$$
$$I_u(m,x) = |u_x^m|^2, \tag{55}$$

where $|v_x^m|^2$ and $|u_x^m|^2$ represent the intensity of an optical pulse photodetected in loop v and u at time step m and position x, according to Equation (1). Thus, I_v and I_u are normalized by the total input power as

$$I_v'(m,x) = \frac{I_v(m,x)}{\sum_{x=-N/2}^{N/2}(|v_x^{m=1}|^2 + |u_x^{m=1}|^2)},$$
$$I_u'(m,x) = \frac{I_u(m,x)}{\sum_{x=-N/2}^{N/2}(|v_x^{m=1}|^2 + |u_x^{m=1}|^2)}, \tag{56}$$

resulting in a sum of scaled intensities $\sum_x\left(I_v'(m,x) + I_u'(m,x)\right)$ of approximately 1, at any time step m, with a deviation of $\pm 10\%$ due to ASE noise from amplifiers. The normalization given in Equation (56) is realized to convert the experimental results into comparable data for the numerical simulations, where initial power is set to unity and χ is kept unconstrained. Furthermore, given an error vector computed by

$$\mathrm{EV}(\chi) = \sum_{m=0}^{m_{MAX}} \sum_{x=-N}^{N} \left(\left|I_v'(m,x) - I_v^{\mathrm{NS}}(m,x,\chi)\right| + \left|I_u'(m,x) - I_u^{\mathrm{NS}}(m,x,\chi)\right|\right)\Bigg|_{\chi=[0:\pi]}, \tag{57}$$

where m_{MAX} denotes the maximum measurement roundtrip and I_v^{NS} and I_u^{NS} are the intensity matrices from the numerical simulations by using the same $\psi^{m=1}$, and identical phase and coupling modulation from Equations (42)-(45). Thus, the nonlinear coefficient in the experiments χ_{EXP} is estimated at the minimum point of $\mathrm{EV}(\chi)$ as follows

$$\chi_{EXP} = \min\left(\mathrm{EV}(\chi)\right) \tag{58}$$

since $\mathrm{EV}(\chi)$ present a parabola-shaped curve at its minimum centered at χ_{EXP} (see Figure 20). Essentially, the minimum point of $\mathrm{EV}(\chi)$ tends to zero at χ_{EXP} and that minimum accumulative error appears due to ASE noise.

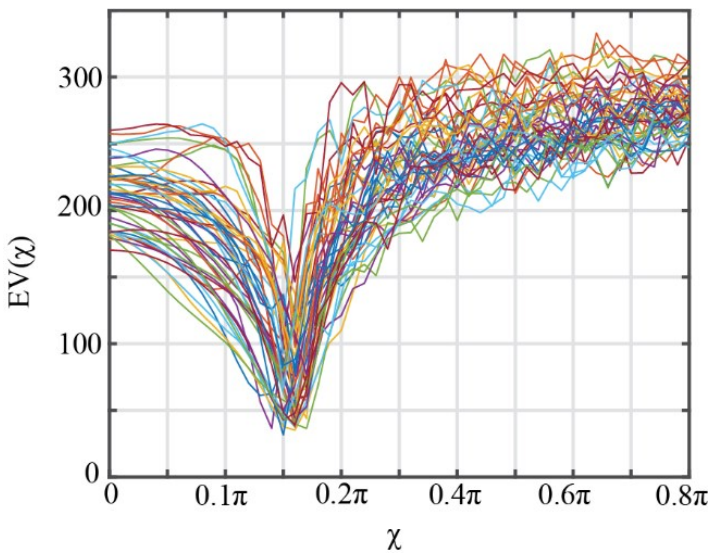

Figure 20: Experimental estimation of nonlinearity $\boldsymbol{\chi}$ based on an error vector computed by numerical simulations (each color displayed in the chart is a measurement ensemble $\boldsymbol{n}$).

According to Equation (42)-(45), and provided that the system works as a self-aligning interferometer, one can state that the phase dynamics at each time step m is completely deterministic in the linear regime due to phase coherence of the optical components used in the experiments (see Figure 5), regardless of the initial amplitude and phase distribution. However, the nonlinear phase dynamics are not deterministic since the additional nonlinear phase shift depends on the nonlinearity and optical power. Since total power is normalized to unity and nonlinearity in the experiments χ_{EXP} is estimated, nonlinear phase dynamics can be now determined by a post-processing algorithm based on Equations (56)-(58). Another mathematical tool for minimizing the error of the searching phase algorithm is to check the relative phase[4] $\phi_{uv}(m,x)$ between loop v and u from time step m to $m+1$

$$\phi_{uv}(m,x) = \phi_u(m,x) - \phi_v(m,x) =$$
$$\sin^{-1}\left(\frac{I'_u(m+1,x-1) - I'_v(m+1,x+1) - (2C_x^m - 1)\big(I'_u(m,x) - I'_v(m,x)\big)}{4\sqrt{I'_u(m,x)I'_v(m,x)\big(C_x^m - C^{2}{}_x^m\big)}}\right), \quad (59)$$

where C_x^m is the modulated coupling coefficient of the variable coupler. However, the compiled relative phase ϕ_{uv} displays only numbers between $\left[{}^{-\pi}/_{2}, {}^{\pi}/_{2}\right]$ due to $\sin^{-1}$ is multivalued, which thus may result in an ambiguity phase error of $\pm\pi$. Besides, ensuring that the nonlinear phase shift φ_{NL} is weak in the experiments, smooth nonlinear phase increments can be observed by the phase difference ϕ_{uv}. Therefore, a tracking phase algorithm built-in

[4] See Appendix D.

Equations (56)-(58) and assisted by Equation (59) carries out the phase information in loop v (ϕ_v) and u (ϕ_u), taking into consideration the estimated nonlinear coefficient χ_{EXP} and initial amplitude/phase distribution $\psi^{m=1}$. Consequently, the vector distribution ψ^m in the experiments is thus reconstructed as

$$\psi^m = \begin{pmatrix} \sqrt{I_v'(m,x)}e^{i\phi_v(m,x)} \\ \sqrt{I_u'(m,x)}e^{i\phi_u(m,x)} \end{pmatrix}. \tag{60}$$

2.3.5. Photonic Multimodal States in Thermal Equilibrium

Formally, a vanishing phase modulation ($\varphi_0 = 0$) results in a bandgap in the center of the Brillouin zone, but the lower and upper dispersion branches are still connected at the Brillouin zone edges since the band structure is periodic in the θ direction (see Figure 10). Therefore, only $\varphi_0 > 0$ ensures that both lower and upper parts of the band structure are isolated, suppressing energy transfer between them. Similarly, $C < 0.5$ can be wisely chosen in order to accelerate the optical thermalization process to thermal equilibrium since it shrinks the eigenmodes −e.i. decrease the coupling strength− and thus facilitates the energy transfer among them during the nonlinear interaction. The photonic mesh lattice configuration is thus chosen as 20 positions, phase modulation $\varphi_0 = 0.25\pi$ and splitting ratio $C = 0.3$ to accommodate a suitable experimental realization for up to 500 roundtrips. The experimental setup is based on Figure 5 and the variable coupler (VC) is modulated in the time domain for generating reflecting boundaries. Since our VC has a maximum switching speed of 1 MHz and a rise/fall time of ~200 ns, the fiber loop length was increased to allow for a larger length difference $\Delta L = 110$ m, resulting in a pulse spacing of $\Delta T = 275$ ns.

As an illustration of a thermal equilibrium process, numerical simulations generate 100 ensembles (n) of the initial distribution $\psi^{m=1}$ based on Equation (49). Each $\psi^{m=1}$ has the same modal occupancy $|c_k^m|^2$, but differs in its phase distribution. Numerically, these initial distributions propagate through the system based on Equations (42)-(45). Here, two scenarios of optical thermalization processes are shown with different initial modal occupancies: 10 eigenmodes equally excited in the lower band (see red stars in Figure 21(a)-(c)) and 10 eigenmodes equally excited in the upper band (see red stars in Figure 21(d)-(f)).

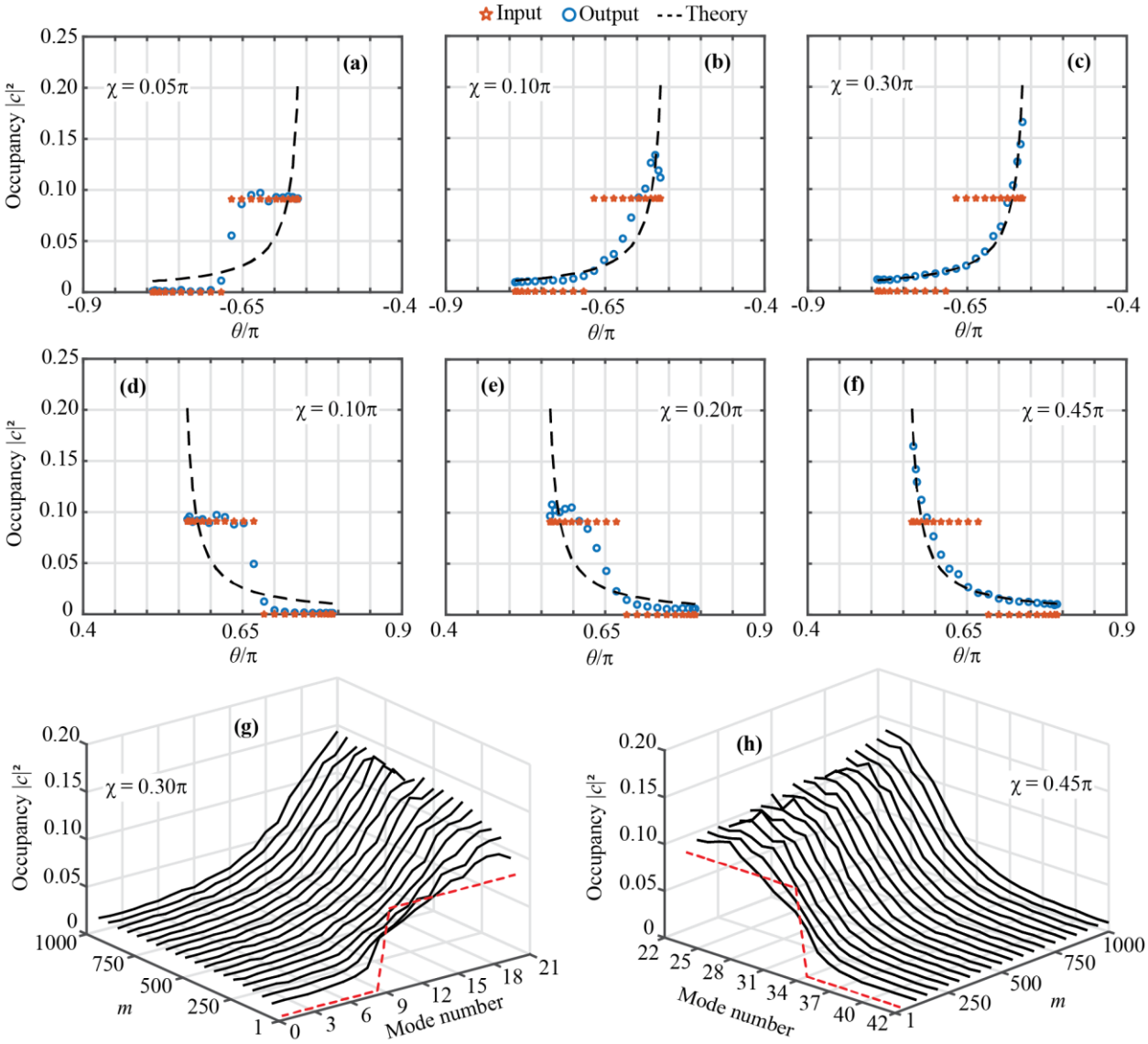

Figure 21: Numerically simulated thermalization processes. (a)-(c) Lower band excitation: initial (red stars) and final modal occupancy (blue circles) after $\mathbf{1000}$ roundtrips for at (a) $\boldsymbol{\chi = 0.05\pi}$, (b) $\boldsymbol{\chi = 0.1\pi}$ and (c) $\boldsymbol{\chi = 0.3\pi}$. (d)-(e) Upper band excitation: initial (red stars) and final modal occupancy (blue circles) after $\mathbf{1000}$ roundtrips for at (a) $\boldsymbol{\chi = 0.1\pi}$, (b) $\boldsymbol{\chi = 0.2\pi}$ and (c) $\boldsymbol{\chi = 0.45\pi}$. Modal occupancy as a function of time steps $\boldsymbol{m}$ for (g) lower band excitation ($\boldsymbol{\chi = 0.3\pi}$) and (h) upper band excitation ($\boldsymbol{\chi = 0.45\pi}$).

A weak nonlinearity χ allows for the adiabatic transfer of energy among modes during nonlinear propagation, which becomes faster for an increase of χ (Figure 21(a)-(f)). Surprisingly, modal occupancy always reaches thermal equilibrium provided that $\chi \neq 0$ (Figure 21(g) and (h)), yet noticeably bigger χ speed up the process. It is observed that entropy grows every time step m in Figure 22(a) and (b) until it reaches its maximum value −e.i. a thermal equilibrium. Additionally, modal occupancy reaches thermal equilibrium by following a Rayleigh-Jeans distribution given by Equation (40).

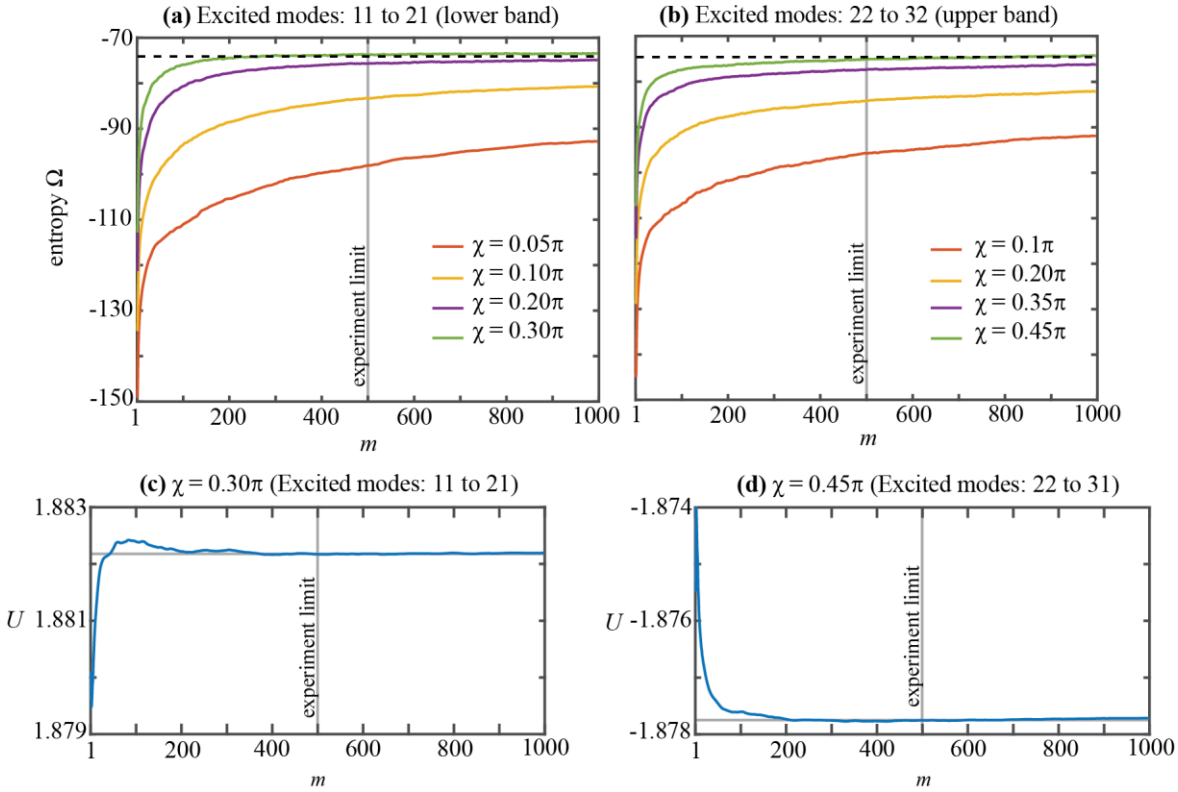

Figure 22: Entropy ($\boldsymbol{\Omega}$) of a (a) lower and (b) upper band excitation as a function of time steps $\boldsymbol{m}$ for different nonlinearity values. Internal energy ($\boldsymbol{U}$) of a (c) lower ($\boldsymbol{\chi = 0.3\pi}$) and (d) upper ($\boldsymbol{\chi = 0.45\pi}$) band excitation as a function of time steps $\boldsymbol{m}$.

As described by Equation (40), the thermodynamic equilibrium is characterized by the intensive parameters T and μ, which are related to the initial parameters, such as P and U. For the initial excitation (lower band) depicted in Figure 21(a), $P = 1$ and $U \approx 1.8795$ result in a theoretical modal distribution (see dashed line in Figure 21(a)-(c)) based on a positive temperature $T = 0.75$ and chemical potential $\mu = 1.77$ extracted from Equation (39) and plotted by Equation (40). A similar effect is expected for the initial excitation (upper band) depicted in Figure 21(c), where $P = 1$ and $U \approx -1.874$. Consequently, for this configuration, a negative temperature $T = -0.75$ and chemical potential $\mu = -1.77$ appears. Due to noise from the EDFAs, our experimental realization is limited to 500 roundtrips for which the noise floor remains comparably low.

Experimentally, a broad Gaussian distribution is prepared for 60 roundtrips by using the phase modulation protocol (see Section 2.1.2). A pre-selection of $n = 50$ ensembles of the initial distribution is carried out by Equations (50)-(52) (see Section 2.3.2). The initial distribution $\psi^{m=1}$ is realized at $m = 60$ with amplitude and phase modulators, and thus propagates through the mesh lattice for 500 roundtrips (see Figure 23(e)). Here, four scenarios of photonic modal states are prepared with 10 eigenmodes equally excited in the

lower (see red stars in Figure 23(a) and (b)) and upper (see red stars in Figure 23(c) and (d)) band, where the initial modal occupancy slightly differ due to fluctuating power from ASE noise. By using Equations (56)-(60), nonlinearity (χ_{EXP}) and correspondent phase (ϕ_u and ϕ_v) from the complex distribution in loop v and u are recovered and estimated, while Equation (47) calculates the modal occupancy.

It is worth noticing that each initial excitation reaches thermal equilibrium at $m = 500$ (see blue curve in Figure 23(a)-(d)) with inherent characteristic parameters of T and μ. Essentially, entropy as a function of m is analyzed to verify that it always increases towards a stationary value –namely a thermal equilibrium (see Figure 24).

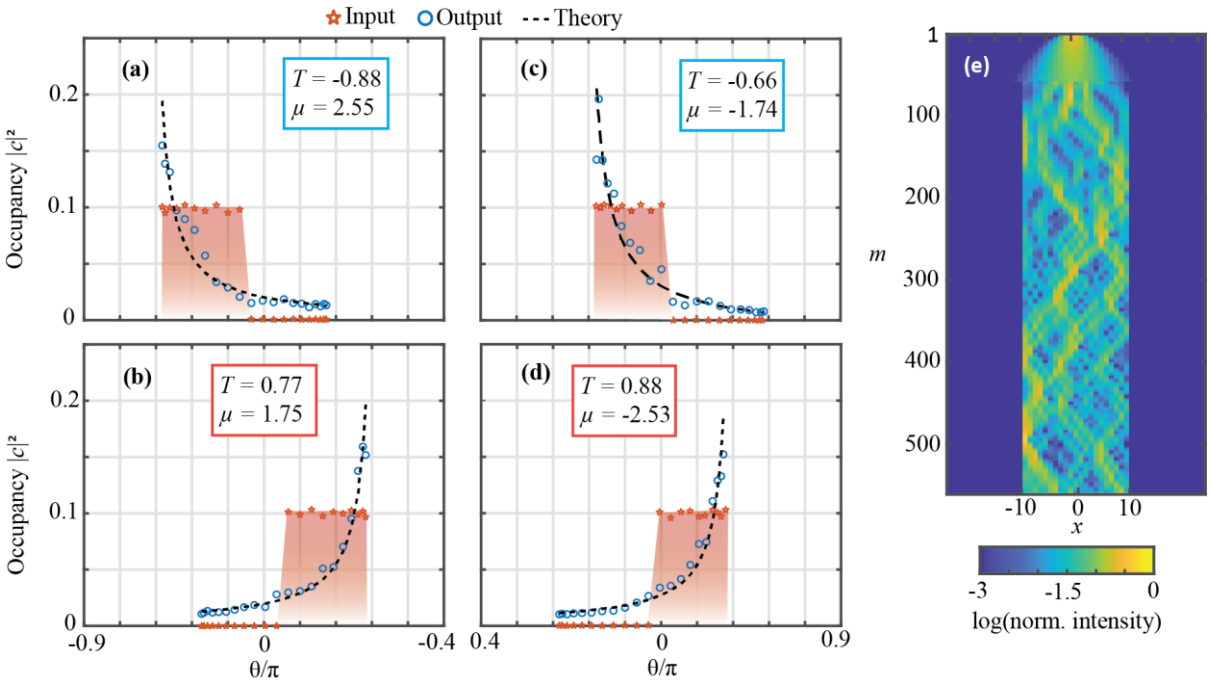

Figure 23: Experimental realization of photonic modal states in thermal equilibrium. The 10th (a) first and (b) last eigenmodes equally excited in the lower band. The 10th (c) first and (d) last eigenmodes equally excited in the upper band. Blue circles and red stars denote initial and final modal occupancy, respectively. (c) Intensity distribution $\boldsymbol{I_v(m,x)}$ in the logarithmic scale as a function of $\boldsymbol{m}$ in loop $\boldsymbol{v}$.

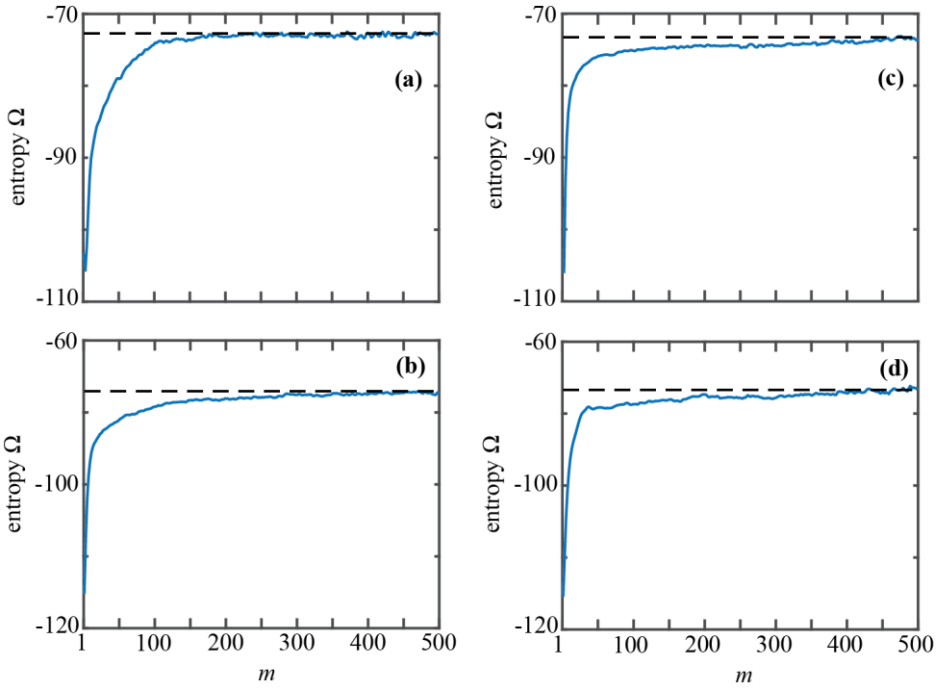

Figure 24: Entropy ($\boldsymbol{\Omega}$) as a function of $\boldsymbol{m}$ for different initial excitations: the 10th (a) first and (b) last eigenmodes equally excited in the lower band, whereas the 10th (c) first and (d) last eigenmodes equally excited in the upper band.

2.3.6. Isentropic Expansion and Compression

Isentropic processes as adiabatic expansion or compression can also be realized in an optical setting as part of a Carnot-like cycle [87]. During such a process, the number of modes remains the same, while the internal energy U is subject to a negative or positive change during expansion or compression, respectively, as a result of the reduction or rise in e.g. of the coupling strengths. Since it should be an adiabatic process, the entropy is kept constant, and thus the modal occupancy $|c_k^m|^2$ remains invariant. Additionally, as a characteristic of an isentropic expansion and compression, the relation of μ/T and U/T remain constant during the process. Therefore, the optical "gas" heats up or cools down during isentropic compressions or expansions, respectively. Based on Equation (49), we numerically generated 200 ensembles (n) of initial distributions $\psi^{m=1}$, each one being in thermal equilibrium and possessing the same modal occupancy $|c_k^{m=1}|^2$, but different random phases. We first numerically simulated the propagation (see Figure 25) with a phase modulation of $\varphi_0 = \pi$ to close the bandgap in the center of the Brillouin zone. During propagation, we change the coupling C starting at 0.3 and adiabatically increasing/decreasing to 0.5/0.1 during expansion and compression processes, respectively.

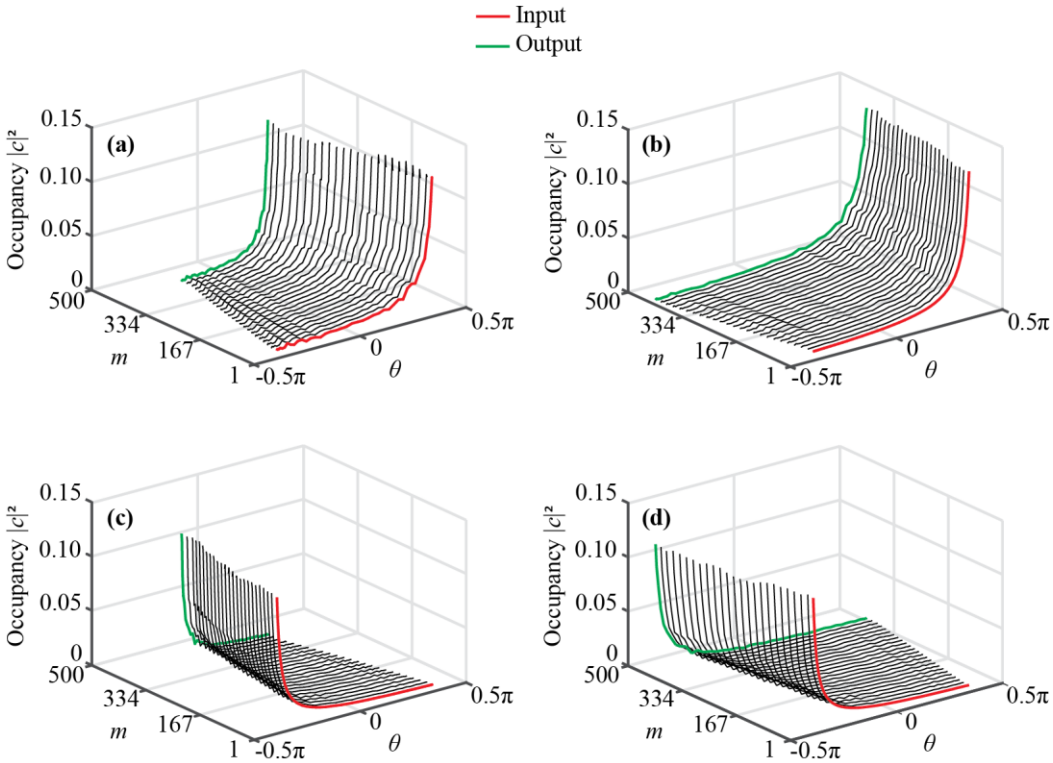

Figure 25: Modal occupancy in thermal equilibrium as a function of $\boldsymbol{m}$ under isentropic (a), (c) compression, and (b), (d) expansion.

We indeed numerically observed isentropic expansion and compression with thermalized modal occupancies comprising negative and positive temperatures (see Figure 25 and Figure 26). Starting with a modal occupancy in thermal equilibrium (i.e. following a Rayleigh-Jeans distribution) at negative temperature and after an adiabatic expansion/compression from $m = 40$ to 440, the splitting ratio C was increased/decreased, resulting in occupancies as shown in Figure 25(a) and (b)). During these processes, internal energy grew/declined until C ceased to change (see Figure 26(a)), whereas μ and T adjusted simultaneously to remain its relation μ/T constant (see Figure 26(c) and (d)). A similar effect occurred for a modal occupancy in thermal equilibrium at positive temperature (see Figure 25(c) and (d) and Figure 26(b), (d), and (f)).

Experimentally, both isentropic expansion and compression processes are investigated at negative and positive temperatures. Similarly, a broad Gaussian distribution is prepared for 60 roundtrips by using the phase modulation protocol (see Section 2.1.2) and a pre-selection of 50 ensembles (n) of the initial distribution is carried out by Equations (50)-(52) (see Section 2.3.2). The initial distribution $\psi^{m=1}$ is prepared as usual at $m = 60$ with amplitude and phase modulators and thus propagates through the mesh lattice for 500 roundtrips.

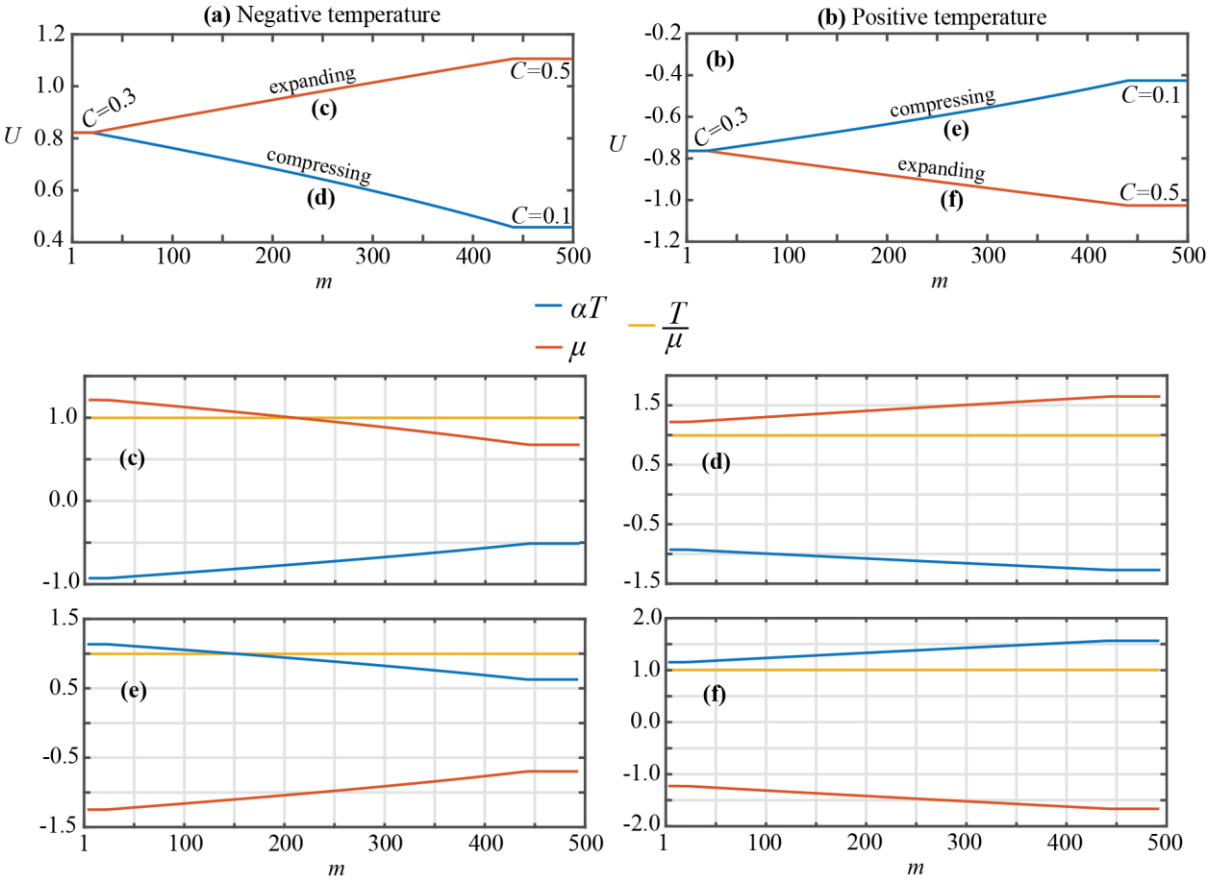

Figure 26: Numerical simulation of the evolution of the internal energy ($\boldsymbol{U}$) as a function of $\boldsymbol{m}$ for (a) negative and (b) positive temperature. (c)-(f) $\boldsymbol{T}$ and $\boldsymbol{\mu}$ increase or decrease during isentropic expansion and compression in order to remain its relation $\boldsymbol{\mu/T}$ constant. $\boldsymbol{\alpha = 10^2}$ is a coefficient used for convenience.

Here, $\psi^{m=1}$ consists of a modal occupancy being already in thermal equilibrium with an initial temperature T_1 and chemical potential μ_1 (see red stars in Figure 27(a)-(d)). Under isentropic expansion/compression, C grows/declines from 0.3 to 0.5/0.1 during time steps m from 80 to 440. After 500 roundtrips, modal occupancy is extracted using Equation (47) (see blue curves in Figure 27(a)-(d)). As expected, internal energy increases/decreases during expansion/compression (see Figure 27(e) and (f)). The theoretical curve from Figure 27(a)-(d) is given by Equation (40).

In the experiment, the ratio between initial and final temperatures and chemical potentials is $(T_1/\mu_1)/(T_2/\mu_2) \approx 0.88$ and not unity as predicted. This discrepancy is caused by the ASE noise from the amplifiers, inducing small deviations in the field distributions u_x^m and v_x^m.

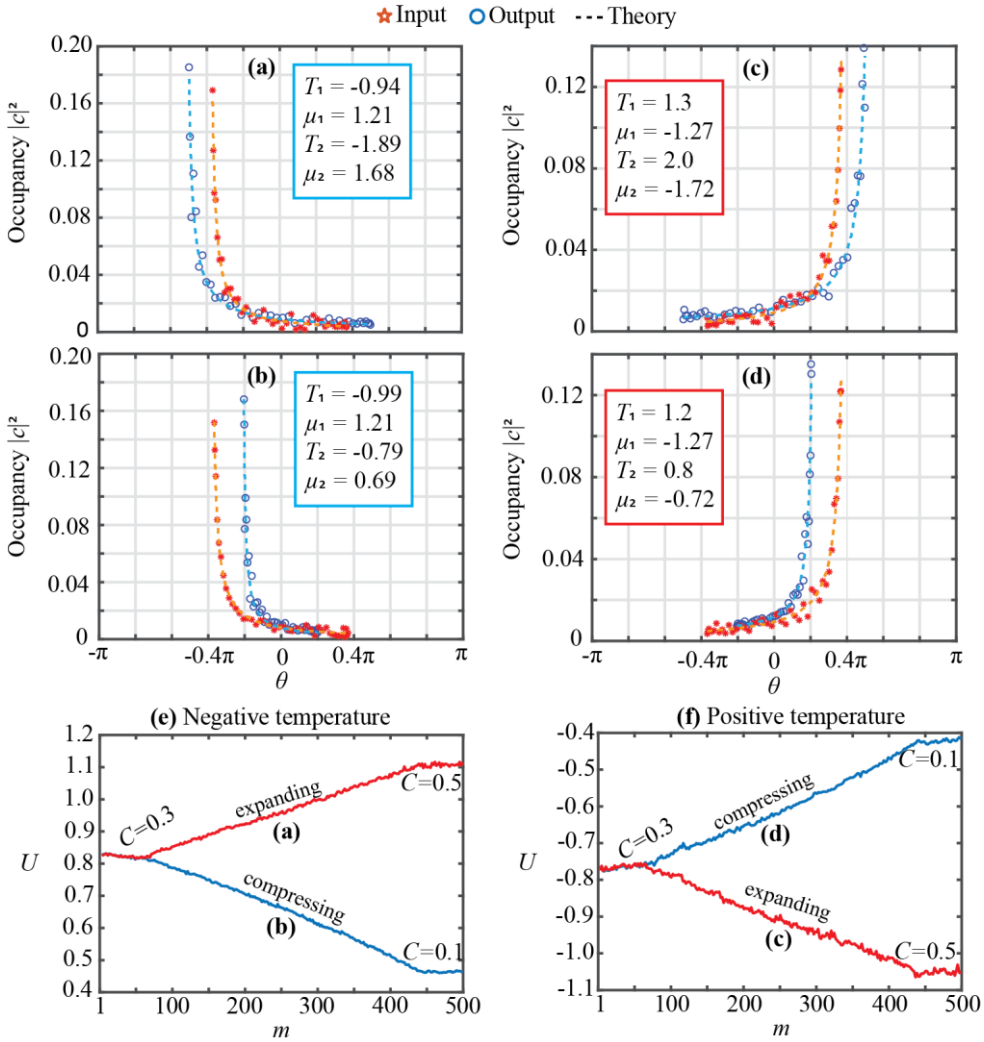

Figure 27: Experimental realization of isentropic expansion and compression in a photonic mesh lattice. Isentropic expansion for (a) negative and (c) positive temperature. Isentropic compression for (b) negative and (d) positive temperature. Internal energy $\boldsymbol{U}$ as a function of $\boldsymbol{m}$ for (e) negative and (f) positive temperature.

2.3.7. Joule Photon-gas Expansion

Contrary to isentropic expansion/compression, Joule photon-gas expansion is connected with heat exchange and comprises a sudden increase in the number of modes ($M_1 \rightarrow M_2$) realized by an expansion of the mesh lattice positions ($N_1 \rightarrow N_2$), while optical power, φ_0 and C are kept constant. The number of associated eigenmodes increases accordingly, i.e. $M = (2N + 2)$.

Here, similar to the isentropic configuration, we choose $\varphi_0 = \pi$ and $C = 0.3$. We first numerically simulated the propagation of a modal occupancy in thermal equilibrium (see blue curve in Figure 25 for negative (a) and positive (b) temperatures), where a sudden increase of mesh lattice positions ($N_2 = 2N_1$) occurs at $m = 60$.

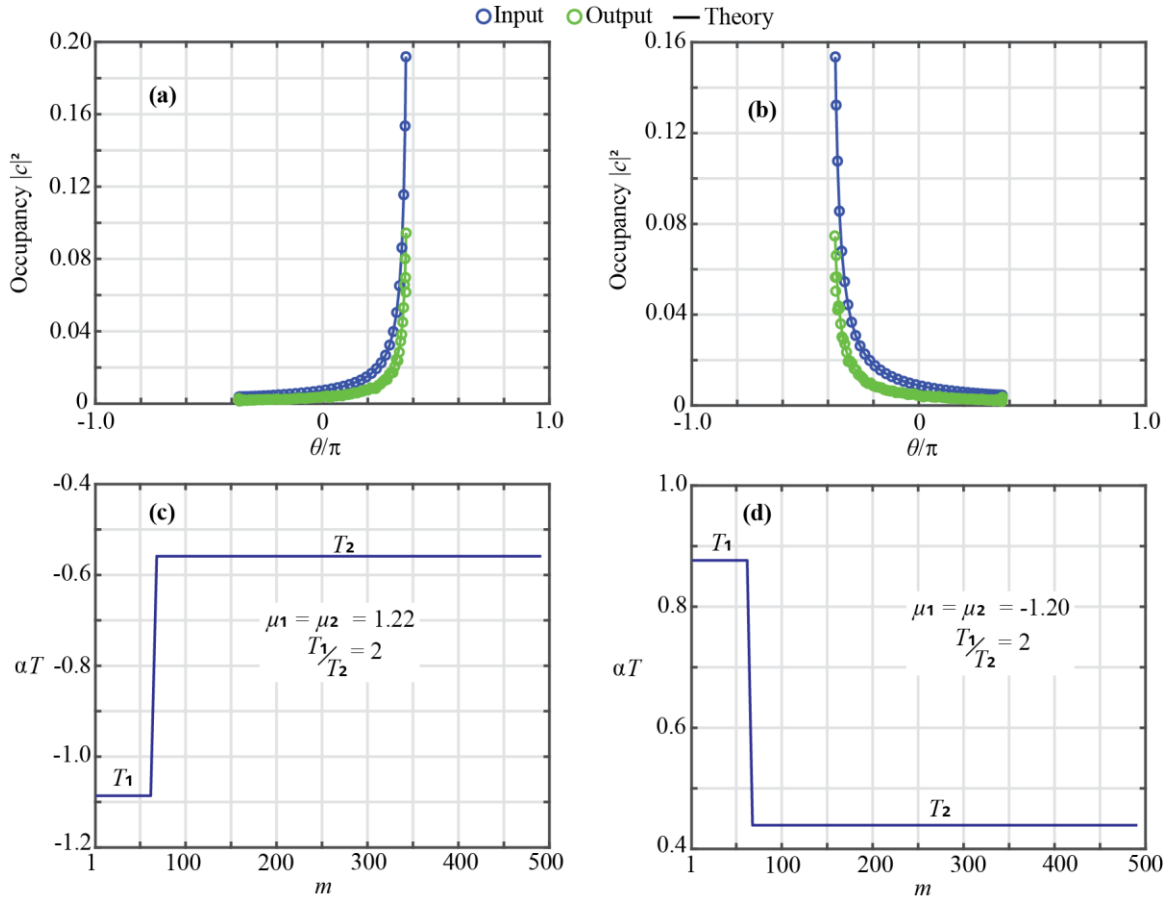

Figure 28: Joule photon-gas expansion. (a)-(b) The entropy in thermal equilibrium is changed by Joule expansion, whereas the final temperature $\boldsymbol{T_2}$ increases proportionally to the expanded mesh lattice position, without changing the chemical potential $\boldsymbol{\mu_1 = \mu_2}$. (e)-(f) Initial (blue) and final (green) modal occupancy distribution after Joule expansion. $\boldsymbol{\alpha = 10^2}$ is a coefficient used for convenience.

Consequently, T increases proportionally to M_2/M_1, while μ remains constant (see Figure 28(c) and (d) for $M_2 = 2M_1$). At the end of this process, the final modal occupancy still exhibits a Rayleigh-Jeans distribution and thus it is in thermal equilibrium, but at a different temperature T_2 and the same chemical potential $\mu_2 = \mu_1$ (see the green curve in Figure 28(a) and (b)). This effect is exceptionally connected to the relative entropy associated with the photonic "monoatomic" chain network, where $\Omega \propto Mln(1/M)$ [87], [91], [110]. As a result, the corresponding temperature T and relation of μ/T in such configuration are proportional to $1/M$ and M, respectively [87]. The resulting photonic response is thus in stark contrast to the Joule expansion behavior expected from ideal monoatomic gases, where the temperature is constant and the chemical potential substantially changes.

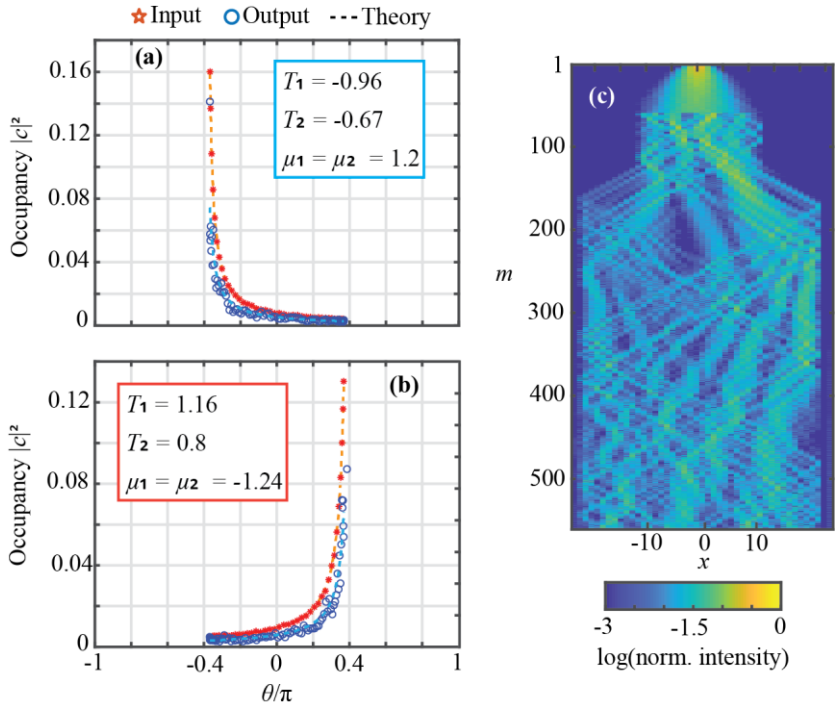

Figure 29: Experimental realization of Joule photon-gas expansion for (a) negative and (b) positive temperature. (c) Intensity distribution (in logarithm scale) as a function of $\boldsymbol{m}$ in loop $\boldsymbol{v}$.

Experimentally, two scenarios are selected starting with a thermal equilibrium at negative and positive temperatures, as shown in Figure 29. As before, a broad Gaussian distribution is prepared for 60 roundtrips by using the phase modulation protocol (see Section 2.1.2) and a pre-selection of 50 ensembles (n) of the initial distribution is carried out based on Equations (50)-(52) (see Section 2.3.2). The initial distribution $\psi^{m=1}$ is prepared at $m = 60$ with amplitude and phase modulators and thus propagates through the mesh lattice for 500 roundtrips.

Here, $\psi^{m=1}$ consists of a modal occupancy being already in thermal equilibrium with an initial temperature T_1 and chemical potential μ_1 (see the red curve in Figure 29(a) and (b)). At $m = 120$ (i.e. 60 roundtrips after the initial distribution preparation, see Figure 29(c)), the mesh lattice suddenly double its size ($N_2 = 2N_1$), whereas φ_0 and C are kept constant. After 500 roundtrips, modal occupancy is extracted following Equation (47) as depicted by blue curves in Figure 29(a) and (b). During such a process, the system's temperature decreases to $T_2/T_1 \approx 0.66$ without changing the chemical potential $\mu_1 \approx \mu_2$. Similarly, the experimental results show that the ratio between the initial and final temperatures slightly differ from the theoretically predicted value of 0.5 due to ASE noise from the amplifiers, which causes small deviations in the field distributions u_x^m and v_x^m.

2.4. Quantum Interference with Entangled Time-bin Photons

The classical theory of information and computation proposed in the last decades relies on independent bit-by-bit macroscopic terms and Boolean operations for transmitting and processing pieces of information from one point to another [113]–[116]. However, the amount of information generated has been exponentially growing every year due to new demanding communication technologies, such as the so-called internet-of-things [117]–[119] and 5G/6G wireless communication [120]–[124]. To overcome the bottleneck associated with classical information processing and computing [125], new approaches using the versatility of quantum mechanics have been theoretically proposed towards a new branch of quantum communication and computation [126]–[128].

By exploiting the degrees of freedom offered by quantum mechanics, such as uncertainty, interference, and entanglement, an enormous amount of information can be encoded in strings of quantum bits (*qubits*), instead of unitary bits as in the classical counterpart [26], [129], [130]. By definition, a classical bit is comprehended of a binary signal (0 or 1) and generally modulated and transported by one or more continuous parameters, such as frequency, phase, or intensity of an electrical signal [116]. On the other hand, quantum data use *qubits* and exploits microscopic systems, such as nuclear spins, atoms, or photons [14], [131]–[135]. Whereas the classical information can be represented by Boolean states 0 and 1, quantum-mechanically this can be done by employing distinguishable states of the *qubits*, e.i. $\langle 0|$ and $\langle 1|$, given, for example, by the polarization or wavelength of light [133], [136], [137]. Quantum information also is represented by a superposition of linear combinations of those basis states, such as $\alpha\langle 0| + \beta\langle 1|$, which allows for extending the information capacity to intermediate states [16], [138], an impossible approach in the classical counterpart based on predefined parameters. With regard to quantum data measurements, the likelihood of measurable entities is based on their probabilities, such as $|\alpha|^2$ and $|\beta|^2$, and pairs of *qubits* add a new "dimension" for exploiting information and operation capacity [139]. Quantum processing also allows for speeding-up computation, particularly quadratic and exponential speed-up for searching and factoring, respectively [131]. Additionally, quantum entanglement, as opposite to the straightforward classical information, can connect any two points in space-time due to its ability towards sharing the same information, providing a new framework on how pieces of information can be judiciously distributed and efficiently processed [140], [141].

Despite logical operations in a classical computation yield a sequence of Boolean operations by logical gates, such as NOT and AND gates [142], nonclassical processors can be also expressed by a sequence of quantum gates, acting on a string of *qubits* [143]–[145]. However, an experimental realization of quantum gates and operations is still challenging due to environmental and propagation losses [14], [146]. Remarkably, photons are not affected by thermal and electromagnetic noises (compared to trapped ions [147], [148]) and thus represent a promising candidate for quantum processors and quantum key distribution (QKD) due to the possibility of exploiting the high-speed telecommunication devices and optical network already distributed worldwide [146]. In optics, a quantum gate can be efficiently implemented by means of linear optics with phase modulation and beam splitters [149]. In particular, fiber-loop systems are thus a powerful tool for performing stable interference measurements [36], [150] and overcoming high losses in spatial waveguide arrays [30], [151]. Provided that information is encoded in the time domain [45], [60], a fiber-loop coupled by a variable beam splitter resembles a photonic mesh lattice, which can perform a variety of quantum measurements, such as controlled-NOT quantum gates [152], boson samplings [15], quantum data compression [153], to mention a few.

Here, a 1D quantum walk setup exploits the discrete arrival times of a single photon as its internal state [18] since the coupled-fiber loop inherently possesses a time-multiplexing approach for encoding and propagating temporal packages into the system. Consequently, encoding quantum information in terms of relative arrival times of light pulses (e.i. time-bin degree of freedom) present a robust kind of single-photon *qubits* [154]. The advantages of time-bin-encoded *qubits* follow:

- High stability and scalability in terms of linear-optical quantum computing (LOQC) implementations since it employs a single optical path (or optical fiber) rather than a maze of multiple paths [155].
- Allowing for universal quantum computing with logical gates based on Knill, Laflamme, and Milburn (KLM) scheme [154].
- Robust to long-distance quantum communication if compared to polarization and frequency degrees of freedom [156].

This project in collaboration with Professor Roberto Morandotti (INRS-EMT) in Montreal, Canada, utilizes the time-bin degree of freedom due to discrete arrival time (i.e. as

an internal state) is fully compatible with a photonic mesh lattice encoded by the time-multiplexing technique. It is proposed a modified 1D coupled-fiber loop for generating and propagating time-bin entangled photons, following Roberto's recent work in [157]. Ultimately, it is proposed an all-optical architecture based on a 1D coupled-fiber loop for generating and processing time-bin *qubits*, which aims for exploiting a large variety of quantum interference measurements, such as quantum gates [149], [158], and a circuit boson-sampling network [15] without changing its physical configuration due to the use of high-speed telecommunication equipment, such as phase modulators and beam splitters.

2.4.1. Modified Coupled-fiber Loop for Time-bin States

With regard to proposed schemes in literature [154]–[157], this one introduces a new approach of all-optical fiber architecture based on quantum interference [159] and entanglement [160], of which the goal ultimately is to carry out an adaptive photonic mesh lattice featuring quantum operation properties. The proposed scheme is composed of a coupled-fiber loop (see Figure 30(a)) and uses time-bin entangled photons generated by spontaneous parametric down-conversion (SPDC) in a periodically poled lithium niobate (PPLN) [161]. The system presents a stable approach due to the fiber-coupler loops act as a self-aligning interferometer as well as adaptive since it possesses an intrinsic ability to prepare entangled quantum states and perform quantum interference measurements along its propagation direction in different time frames (see Figure 30(b)).

As the process of interference requires a precise arrival time of two-photon beams at the variable coupler, external photon sources and quantum gates based on interferometer waveguide arrays need an extreme precision in length [126], which makes it a challenging approach due to imperfection in fabrication. On the other hand, fiber-loops can overcome this issue provided that the system is re-utilized by using it as a source for generating identical time-bins before the quantum measurement set, maintaining all photon-bins in the time domain equally spaced and matching them with the time delay of that coupled-fiber loop (see Figure 30(a) and (b)).

Schematically, a seed bright pulse at a central frequency (f_0) is injected into loop u by an optical switcher (gate 1 in Figure 30(a)). Throughout two roundtrips, gates 1 and 2 are kept at full transmission stage (e.i closed), where two optical pulses spaced by ΔT in the time domain (e.i. due to loop length difference ΔL) are generated by a free LW event.

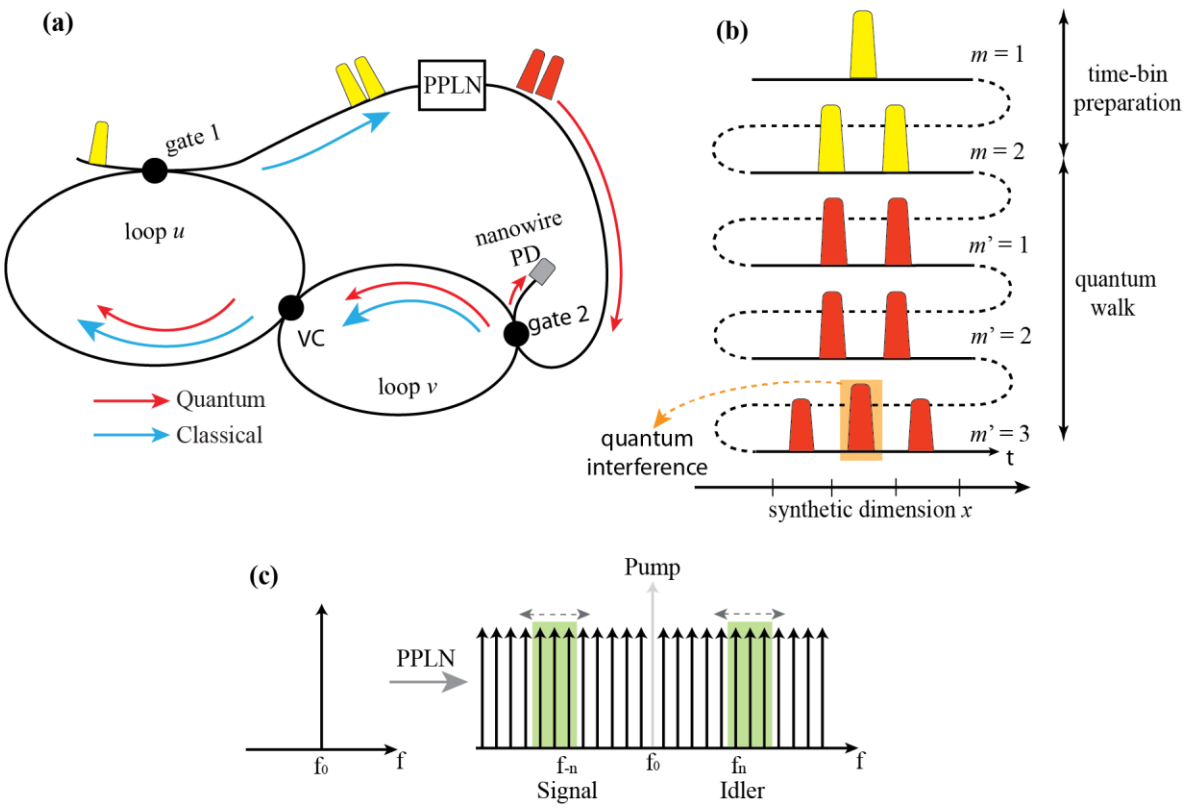

Figure 30: Preparation and quantum measurement of the proposed coupled fiber-loop, where stable quantum interferences are acquired due to a perfect timing match between photon bins. (a) The proposed architecture utilizing a fiber-loop system for preparing time-bin photons and measuring quantum interferences. (b) Representation of two-stage measurement set: time-bin preparation (yellow pulses) and quantum walk measurement (red pulses). (c) In the frequency domain, a frequency carrier at $\boldsymbol{f_0}$ inserted into the periodically poled lithium niobate (PPLN) at a proper input power creates entangled photon-pairs by the nonlinear process spontaneous parametric down-conversion (SPDC). Symmetric optical bands are selected individually (green boxes) by a programmable optical filter to measure the biphoton joint-coincidence spectral correlations.

Afterward, gate 1 is set to full reflection (i.e. open) and two bright pulses leave the coupled-fiber loop and enter the PPLN. At a proper input power, SPDC generates a broad frequency comb, including single-photon pairs at signal (f_{-n}) and idler (f_n) frequencies (see Figure 30(c)) [162]. Finally, a programmable optical filter selects this signal and idler pair for injection (in the opposite direction of classical LW) into loop v by an optical switcher (gate 2) to perform a quantum walk (see Figure 30(b) for $m' = 1, 2$ and 3).

Essentially, a single photon interference in a Mach-Zehnder interferometer is often referred to as a classical interference since it produces a phase-dependent probability to measure a single photon at its output, similar to a wave propagating through two paths and interfering with itself. On the other hand, the biphoton interference, namely referred to as quantum interference, results in a phase-dependent probability to measure two-photon coincidences, which has no classical analogy [163]. This concept was first exploited by the so-called Hong-Ou-Mandel (HOM) effect, where two photons enter two different ports of a beam splitter [164]. If those photons are indistinguishable (e.i. there is no information on

which photon entered which port of the beam splitter), they will exit always together at the same output port. This results in a two-photon bunch and zero probability to detect coincidences between detectors connected with the different output ports of the splitter since the likelihood of photons crossing each other are canceled for identical photons [165]. Instead, coincidences can be detected if a temporal delay between the photons is introduced, making them temporally distinguishable and thus allowing them to exit different output ports.

A time-bin entanglement is a discrete form of energy-time entanglement [160], [166] and a photon pair is generated in a coherent superposition of two time-bins referred to as first $|1\rangle$ and second $|2\rangle$, according to our setup (please, note that the notation used in [157] for these two time-bins is ascribed as short $|S\rangle$ and long $|L\rangle$ and it has been changed in this dissertation in order to not confuse with short/long loops in our set-up). Consequently, the quantum state generated at the PPLN is a coherent superposition written as

$$|\Psi\rangle = \frac{1}{\sqrt{2}}\left(|1,1\rangle + e^{i\varphi}|2,2\rangle\right), \tag{61}$$

where $|1,1\rangle = |1\rangle_{\text{signal}}|1\rangle_{\text{idler}}$ denotes the signal and idler photons both being in the first time-bin, and $|2,2\rangle$ in the second time-bin. Here, φ is a phase shift introduced by PM to the second time-bin only. The state $|\Psi\rangle$ injected into the fiber-coupled loop is interfered after two roundtrips ($m' = 3$ in Figure 30(b)), where the central peak corresponds to a projection on a superposition of both time-bins, namely $|\Psi_C\rangle = \frac{1}{\sqrt{2}}\left(|1\rangle + e^{i\varphi}|2\rangle\right)$ [167].

2.4.2. Experimental Results

The proposed coupled-fiber loop set-up in the experiments is depicted in Figure 31(a). The system is redesigned with shorter loops due to limited integration time and the number of experimentally achievable time steps. The limiting characteristic here is the switching speed of those commercially available optical switchers (gate 1 and 2) and variable coupler (Nanona™ optical switcher from BATi) with a response time of 60 ns and insertion loss of 1 dB. Another limiting factor is a balancing threshold between fiber loop length/roundtrips and integration time, in which longer loops result in a smaller repetition rate (f_{rep}) of that seed pulse injected into the system and thus bigger integration time. The two fiber loops are coupled by a variable coupler. They have an average length of $L \approx 110$ m ($T \approx 550$ ns) and differ in lengths by $\Delta L \approx 22$ m ($\Delta t \approx 110$ ns).

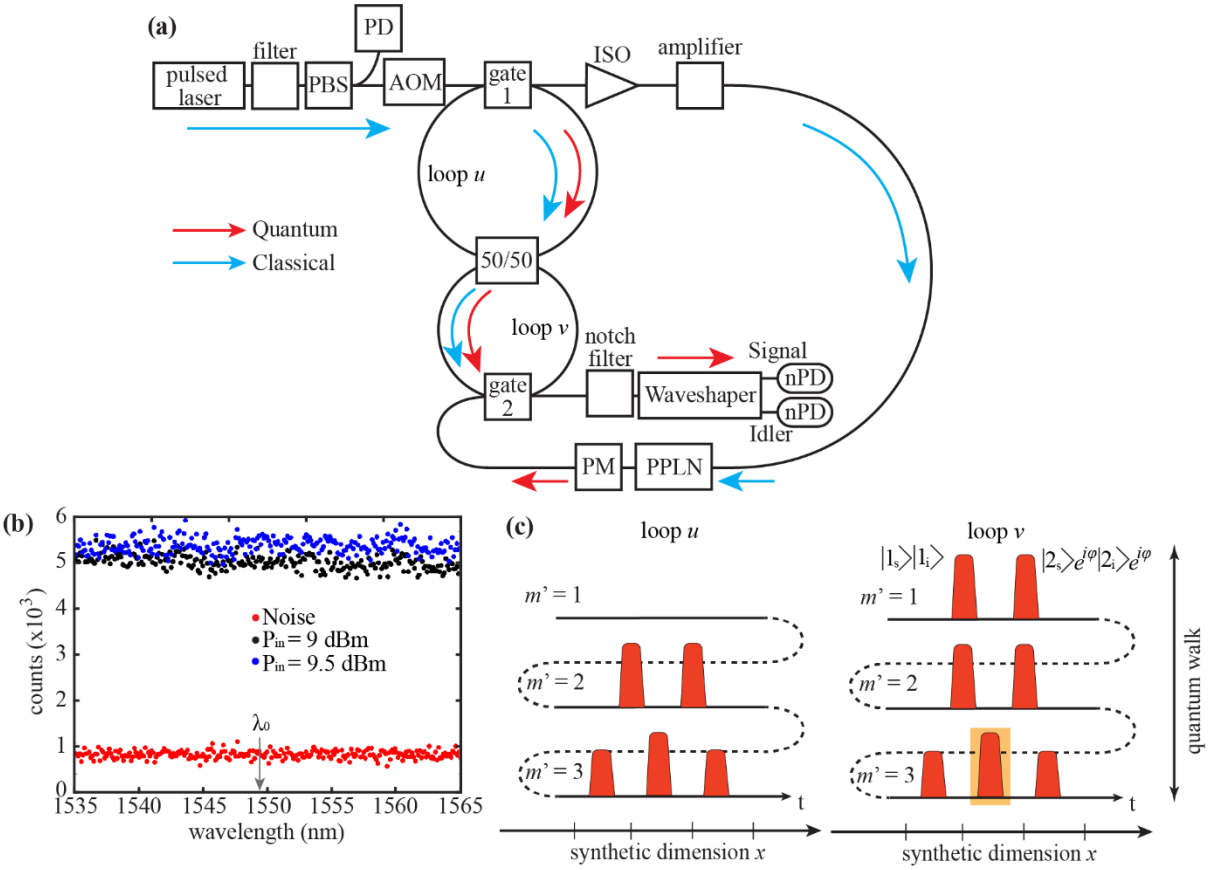

Figure 31: Experimental realization of a quantum walk based on a modified coupled-fiber loop for generating and propagating entangled single photons. (a) Experimental set-up. (b) Single-photon spectrum measurement after the PPLN. Red dotted curve represents the measurement of nPD's dark count rate and $\boldsymbol{\lambda_0 = 1549.44}$ nm is the pump wavelength ($\boldsymbol{f_0 = 193.48}$ THz). (c) Time-bin-encoded photon pairs are injected into loop $\boldsymbol{v}$ to perform quantum interference, where coincidence is analyzed on the interfered central peak (orange box) at $\boldsymbol{m' = 3}$. VC: variable coupler, ISO: optical isolator, PBS: polarizing beam splitter, nPD: superconducting nanowire detector. PD: photodetector.

In this case, f_{rep} is configured to 200 kHz (i.e. a seed pulse every 5 μs) to allow for 7 roundtrips per measurement set, from which three roundtrips are for preparation and four for a quantum walk. Initially, a sequence of coherent pulses at f'_{rep} of 10 MHz from a pulsed laser (PriTel Femtosecond Fiber Laser series) at $\lambda_0 = 1549.44$ nm ($f_0 = 193.48$ THz) is carved into $f_{\text{rep}} = 200$ kHz by an AOM (40-dB suppression ratio). An optical passband filter reduces the optical signal bandwidth to 0.3 nm to match the maximum phase-matching bandwidth of the PPLN system. A PBS ensures the same polarization of light since the whole set-up utilizes polarization-maintaining SMF.

The coupled-fiber loop in the first stage of preparation works with classical light pulses and, throughout its light walk dynamics in a clockwise direction, can create two bins in the time domain spaced by ΔT. After the preparation stage, the generated time-bins are decoupled out of the loop u by the gate 1, amplified and transmitted to a dual-stage PPLN

system (see Figure 32), where the first PPLN converts the pump frequency from 1549.44 nm (see Figure 32(a)) to 774.7 nm (see Figure 32(b)) by parametric up-conversion.

Next, the second PPLN generates broadband signal/idler photon pairs (~8 THz) symmetrically with respect to the pump frequency. Figure 31(b) shows the single-photon spectrum measurement, which consists of swiping a 25-GHz bandwidth of a programmable optical filter (Finisar Waveshaper 4000s) over the entire operating frequency range (~8 THz) and photodetecting by a superconducting nanowire detector (nPD) at the output of the second PPLN. Finally, a notch filter (100-dB suppression at ~1549.52 nm) removes any residual pump frequency (e.g. back-reflections) to the nPDs and a PM can be used to tune the phase difference between two of those time-bins.

For all measurements, we used nPDs from Quantum Opus with ~80% detection efficiency (corresponding to 0.96 dB detection loss) and 50 ps timing jitter. The detector signals were acquired with a Time to Digital Converter (TDC) from PicoQuant (HydraHarp 400) with a 1 ps timing resolution.

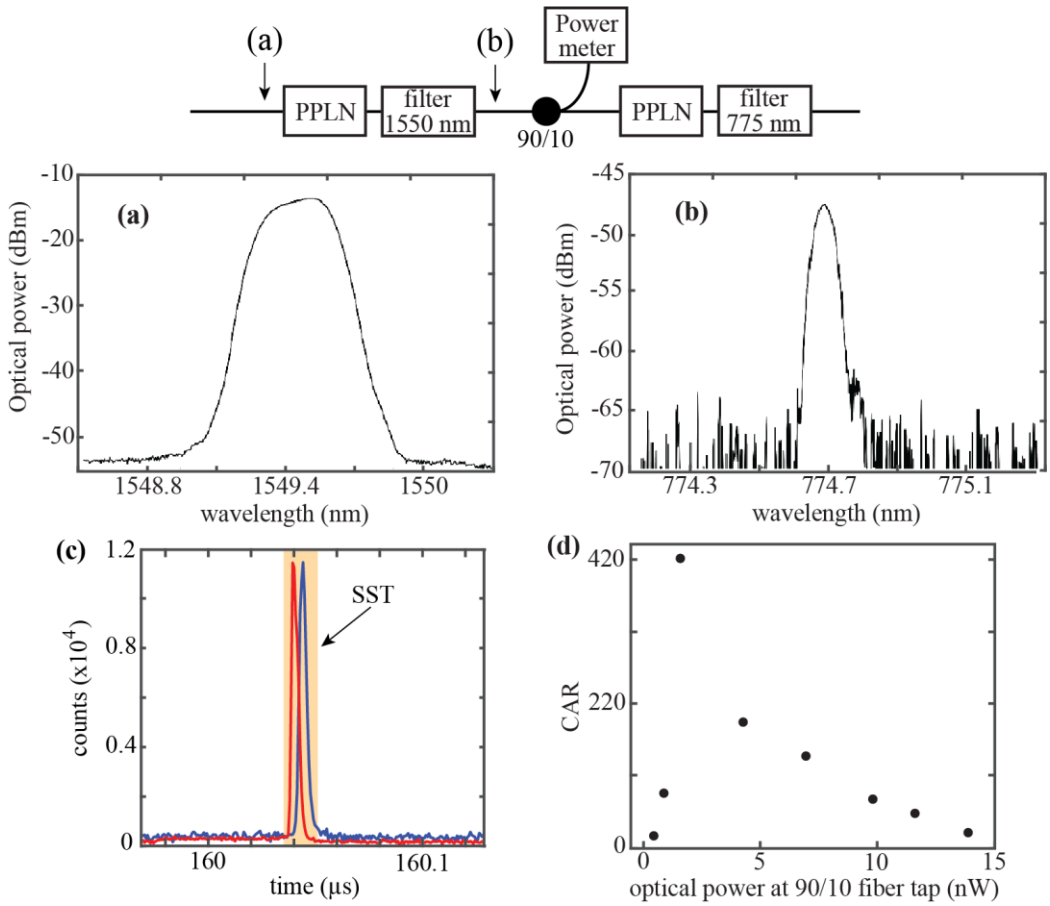

Figure 32: Two-stages PPLN system. Optical bandwidth (a) before and (b) after the first PPLN. (c) Histogram of a single photon detection with superconducting nanowire detectors for a single pulse injected into the PPLN at $f_{rep} = 200$ kHz (without passing through the coupled-fiber loops). The start-stop-time (SST) span is illustrated as an orange box. (d) Correspondent coincidence-to-accidental ratio (CAR) as a function of the input power.

The losses for the photons in the quantum walk measurement relies on the number of roundtrips m' employed and add up to $(5.96 + 2m')$ dB, which breaks down as follows: 5 dB for the programmable optical filter (Finisar Waveshaper 4000s), 0.96 dB detection loss (Quantum Opus detectors), and 1 dB per optical switcher. The first measurement consists of inserting a single bright pulse into the PPLN at $f_{\mathrm{rep}} = 200$ kHz (without passing through the coupled-fiber loop) to verify the optimal input power for maximum coincidence spectral correlations of a photon-pair.

Figure 32(c) depicts the histogram of photon counts detected by an nPD (integration time of 15 minutes) for 1.2 THz bandwidth of signals (f_{-n}) and idlers (f_n) frequencies. By a post-processing algorithm built-in Matlab, the time-tagged time-resolved (TTTR) data acquisition records all individual pulses, and in particular their arrival times [168]. Since this system employs a fixed synchronization rate based on f_{rep}, the data acquired during an integration time are recorded in time tags of a time-correlated single-photon counting (TCSPC) time, namely T3 analysis from Pico-Quant manufacturer [169]. By a T3 analysis, coincidences are counted when a photon detected from both nPDs arrives at the same start-stop-time (SST) span, whereas accidentals are added when a photon is not simultaneously detected over that considered SST span (see orange boxes in Figure 32(c)). The coincidence-to-accidentals ratio (CAR) is measured as a function of the input power, as shown in Figure 32(d). Furthermore, the two time-bin-encoded photon-pairs are injected into loop v by gate 2 to perform a quantum walk, as shown in Figure 31(a) and (c). A phase modulator placed after the PPLN modulates the second time-bin only by a phase shift of φ.

Figure 33 shows the quantum interference measurement of the photons in loop v at time step $m' = 3$. At $m' = 3$, a quantum interference between the first and second bin occurs and it is proportional to φ. According to [157], [166], the coincidence counts of a two-photon interference is expected to be proportional to $1 - V\cos(\phi + \varphi_s + \varphi_i)$ in the SPDC case, where V is the interferometry visibility, ϕ is the phase shift applied at the pump frequency, and φ_s and φ_i are the phases for the signal and idler frequencies, respectively. For this particular set-up configuration, $\phi \approx 0$ and $\varphi_s \approx \varphi_i = \varphi$ due to the signal and idler frequencies receive the same phase on the phase modulator. Therefore, the phase shift φ introduced on the second time-bin by a PM (see Figure 31(a)) governs the quantum interference between both time-bin-encoded photon-pairs.

The measurement set consists of selecting three different signal/idler bands of 420 GHz (3.3 nm) by a programmable optical filter (see Figure Figure 33(a)) to be photodetected over

an integration time of 4 hours for each phase shift φ. Provided that $\varphi > 0$ (see Figure 33(b)), the coincidence counts increases until it reaches its maximum value for $\varphi \approx \pi/4$ and $3\pi/4$, while the minimum values are achieve for $\varphi \approx 0, \pi$ and 2π. Yet, by analyzing the coincidence counts in Figure 33(b) as a function of φ, the observed entanglement visibility of 95% is found for the first band (blue curve) and 75% for the second (red curve) and third (green curve) bands. The resulting interference effect clearly exceeds $1/\sqrt{2} \approx 71\%$, which represents a violation of the Bell inequality for a biphoton interference [162], [170] and demonstrates that the twin photons are time entangled and realize quantum interference [156], [171]. Additionally and contrary to the optical delay line scheme demonstrated in [139], [157], the proposed coupled-fiber loops generated and measured time-bin-encoded photon-pairs without the need for any external interferometry stabilization mechanism.

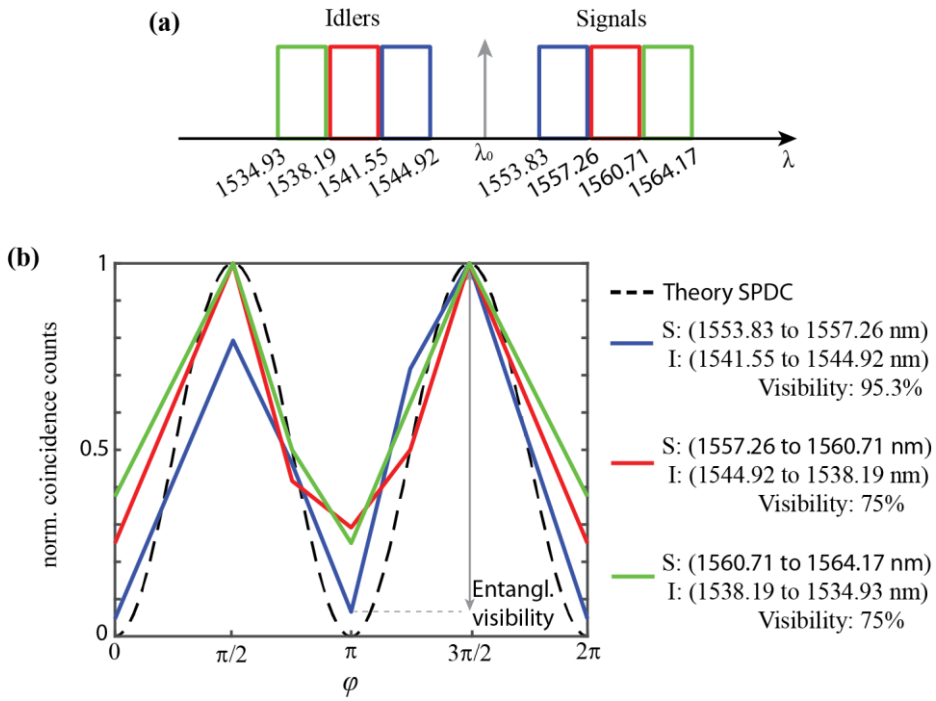

Figure 33: Quantum interference measurements of time-bin-encoded photon-pairs by using a coupled-fiber loop. (a) The optical bandwidth of signals/idlers (420 GHz) is selected by a programmable optical filter. (b) Normalized coincidence counts as a function of $\boldsymbol{\varphi}$ for three different signal/idler bands.

2.4.3. Outlook: Quantum Walk Approach for Quantum Information Processing

As the typical information is time-bin-encoded, the 50/50 optical coupler can be replaced by a temporally modulated variable coupler (see Figure 34(a)) for modeling any type of spatially lumped coupling ratios, thus creating an adaptive quantum photonic measurement platform (see Figure 34(b), where the indices below the interferometers indicate their splitting ratio). Therefore, a photonic mesh lattice can be reconfigured and controlled at the working speed of telecommunication devices. Due to the latter feature, time and frequency entanglement can be also prepared and fully exploited for information processing in hyper-entanglement states [16], [138], [139], featuring the all-optical architecture shown in Figure 31. The adaptive quantum photonic platform depicted in Figure 34(b) can be used as a quantum circuit for information processing, exploiting time-frequency entanglement and quantum interference measurement for quantum gates [149], [158], or a circuit boson-sampling network [15]. The transverse (x) and propagation (m) direction of a resembled photonic mesh lattice can be easily configured as required without changing its physical configuration.

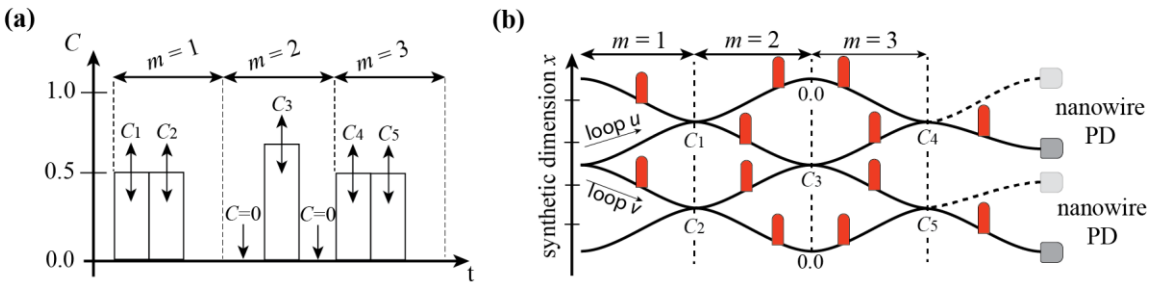

Figure 34: All-optical architecture based on a 1D coupled-fiber loop. (a) Variable coupler modulation in the time domain for modeling any type of spatially lumping coupling ratios, resulting in (b) an adaptive quantum photonic measurement platform.

3. Two-dimensional Photonic Mesh Lattice Projects

3.1. Generation of a 2D Gaussian Wave Packet as an Initial Distribution

In general, all experiments using a 2D broad excitation in this present dissertation employed an amplitude modulation protocol similar to the 1D approach (see Section 2.1). The working principle of this protocol is based on the fact that blocking inner and outer loops alternately every time step results in diffusive equations, as explained in the following for the linear system ($\chi = 0$) without external phase modulation ($\varphi_0 = 0$). At time step $m = 1$, a single pulse is inserted into the system. For $m = 1$ until $m = M$ time steps, path A and B are blocked in an alternating way resulting in the following evolution equations:

$$a_{x,y}^{m+1} = \frac{1}{2}\left(\underbrace{a_{x+1,y+1}^{m}}_{=0,\text{ for even}(m)} + i\,\underbrace{b_{x+1,y+1}^{m}}_{=0,\text{ for odd}(m)} + i\,\underbrace{b_{x+1,y-1}^{m}}_{=0,\text{ for odd}(m)} - \underbrace{a_{x+1,y-1}^{m}}_{=0,\text{ for even}(m)} \right), \tag{62}$$

$$b_{x,y}^{m+1} = \frac{1}{2}\left(\underbrace{b_{x-1,y-1}^{m}}_{=0,\text{ for odd}(m)} + i\,\underbrace{a_{x-1,y-1}^{m}}_{=0,\text{ for even}(m)} + i\,\underbrace{a_{x-1,y+1}^{m}}_{=0,\text{ for even}(m)} - \underbrace{b_{x-1,y+1}^{m}}_{=0,\text{ for odd}(m)} \right), \tag{63}$$

where paths C and D are maintained constant. For a double step starting at $m = 1$, this results in a diffusive equation

$$a_{x,y}^{m+2} = \frac{i}{4}\left(b_{x+2,y+2}^{m} - b_{x+2,y-2}^{m}\right) \tag{64}$$

$$b_{x,y}^{m+2} = -\frac{1}{4}\left(b_{x,y-2}^{m} + 2b_{x,y}^{m} + b_{x,y+2}^{m}\right) \tag{65}$$

along the y-direction (see Figure 35(a)-(c)). After the first M time steps, the same scheme is applied to paths C and D while A and B are not modulated anymore.

$$c_{x,y}^{m+1} = \frac{1}{2}\left(\underbrace{c_{x+1,y+1}^{m}}_{=0,\ \text{for even}(m)} + \underbrace{i d_{x+1,y+1}^{m}}_{=0,\ \text{for odd}(m)} + \underbrace{i d_{x-1,y+1}^{m}}_{=0,\ \text{for odd}(m)} - \underbrace{c_{x-1,y+1}^{m}}_{=0,\ \text{for even}(m)} \right), \tag{66}$$

$$d_{x,y}^{m+1} = \frac{1}{2}\left(\underbrace{d_{x-1,y-1}^{m}}_{=0,\ \text{for odd}(m)} + \underbrace{i c_{x-1,y-1}^{m}}_{=0,\ \text{for even}(m)} + i\,\underbrace{c_{x+1,y-1}^{m}}_{=0,\ \text{for even}(m)} - \underbrace{d_{x+1,y-1}^{m}}_{=0,\ \text{for odd}(m)} \right). \tag{67}$$

Again, for a double step starting from an even $m = M$ this results in diffusion equations

$$c_{x,y}^{m+2} = \frac{i}{4}\left(d_{x+2,y+2}^{m} - d_{x-2,y+2}^{m}\right) \tag{68}$$

$$d_{x,y}^{m+2} = -\frac{1}{4}\left(2d_{x,y}^{m} + d_{x-2,y}^{m} + d_{x+2,y}^{m}\right) \tag{69}$$

along the horizontal direction (see Figure 35(d)-(f)). In this way, after M time steps along the vertical and another M time steps along the horizontal direction, a broad Gaussian distribution

$$a_{x,y}^{m} = \frac{1}{\sqrt{\frac{\pi}{2}M}} e^{-\frac{x^2+y^2}{2M}} \tag{70}$$

is created provided that $M \gg 1$. The width of the distribution w is symmetric in xy coordinates and increases $\propto \sqrt{M}$.

At the time step $2M - 1$, one of the paths C and D is blocked for the last time and consequently, when passing next time the 50/50 at the beginning of time step $m = 2M$, the Gaussian distribution is split with an equal intensity into two parts propagating through paths A and B. A phase shift of $\pi/2$ introduced by the optical coupler (see Equations (7)-(10)) is compensated by the phase modulator in path D at time step $2M$. Additionally, in order to excite an eigenstate of the system, an amplitude and phase relation[5] has to be adjusted between paths A and B at the time step $2M$ by the modulators according to the eigenstate in Equation (19) and Table 1. For instance, considering a phase modulation in Equation (18) for $\varphi_0 = \pi/2$, the eigenstate for exciting the center ($k_x = k_y = 0$) of the focusing band should have an amplitude ($|A|/|B|$) and phase ($\arg A/B$) relation of 1.93185 and $-\pi/4$, respectively.

Table 1: Amplitude and phase difference between loop ***A*** and ***B*** at the time step $2M$ in order to excite the center of the Brillouin Zone ($k_x = k_y = 0$) of the focusing band for different modulated system configurations.

φ_0	$\lvert A\rvert/\lvert B\rvert \; at \; m = 2M$	$\arg(A/B) \; at \; m = 2M$
$\pi/6$	2.35625	$-5\pi/12$
$\pi/3$	2.1889	$-\pi/3$
$\pi/2$	1.93185	$-\pi/4$
$2\pi/3$	1.61803	$-\pi/6$
$5\pi/6$	1.29177	$-\pi/12$

[5] See Appendix B.

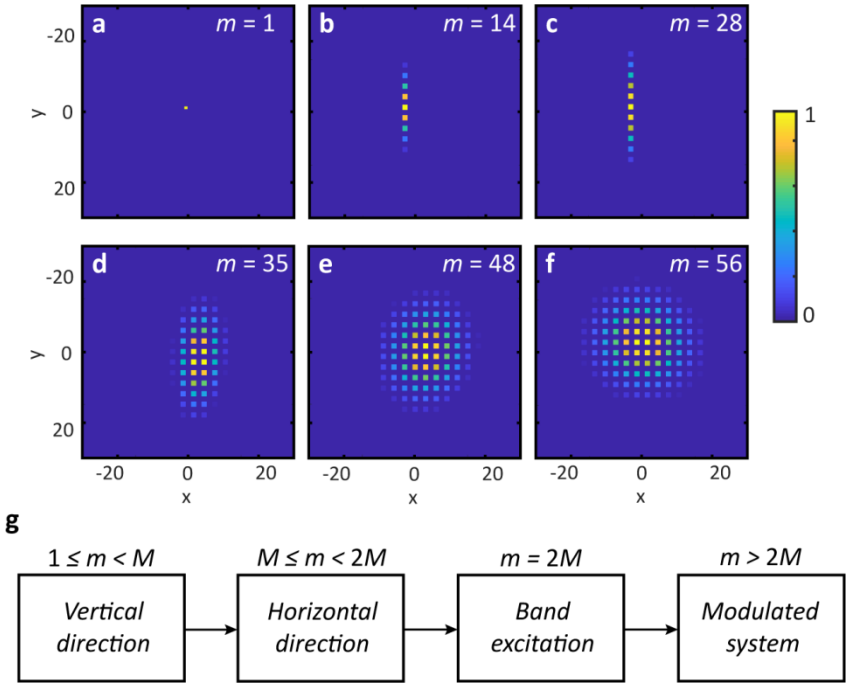

Figure 35: Protocol used for creating pulse chains with a Gaussian envelope. (a)-(c) Discrete points with a Gaussian envelope expand in $\boldsymbol{y}$-direction. (d)-(f) A Gaussian envelope expands in $\boldsymbol{x}$-direction. (g) Flowchart of the preparation and measurement set for Gaussian beam analysis.

3.2. Nonlinear dynamics in a 2D Conservative Photonic Mesh Lattice

Power-induced wave collapse is one of the most fascinating phenomena in optics as it provides extremely high intensities, thus stimulating a range of nonlinear processes [172]. For low power levels, propagation of beams in bulk media is dominated by diffraction, while above a certain threshold self-focusing is steadily enhanced by the action of a positive nonlinearity [53]. Pulses propagating in optical fibers, a genuine 1D system, tend to form solitons, an effect well described by the nonlinear Schrödinger equation (NLS) [172], [173]. Here, the balance of nonlinearity and dispersion imposes an unambiguous relationship between amplitude, energy, and width of stable pulses. In contrast to fiber solitons, stationary states of the 2D NLS can be scaled arbitrarily in amplitude and width, while energy stays constant [174]–[176]. An autocatalytic blow-up occurs by self-focusing nonlinearity, which is only stopped by saturation of the nonlinearity [177], material damage [178], or the inherent medium discreteness [179]. In the latter case, this leads to energy localization on a single site [45]. In such a situation, the beam compresses during propagation, while the amplitude increases, and consequently enhances the effect of the cubic nonlinearity in an autocatalytic way, ultimately ending in a blow-up of the nonlinear wave [172], [175], thus potentially leading to stable solitons for quadratic [180], thermal [181] or photorefractive nonlinearities [182], [183]. The collapse also finds its end when the field structure is so far compressed that it resolves the discreteness of the underlying system, resulting in the formation of an extremely spiked single lattice site soliton [184]–[187]. In 2D waveguide arrays, nonlinear pulse compression [188], discrete solitons [189], [190], and even light bullets for temporal dispersion [191] were reported.

3.2.1. Theoretical Model

Following the Vlasov-Petrishchev-Talanov theorem [172], collapse only occurs if $(p-1)D \geq 4$, with p being the order of the nonlinearity and D the dimension of the system. In particular, collapse and the resulting boost of nonlinear phenomena is not expected for genuine one-dimensional fiber systems ($D = 1$) with cubic nonlinearity ($p = 3$). Therefore, this project follows the introduced concept of synthetic dimensions to experimentally demonstrate that a genuine 1D system formed by coupled-fiber loops can resemble an extended effective lattice with two artificial transverse dimensions. Consequently, a suitable band structure enables the investigation of nonlinear propagation effects, leading to a collapsing wave.

For this project, the experimental setup follows the scheme presented in Figure 3, and, consequently, pulse dynamics are described by the generalized four discrete evolution equations in Equations (7)-(10). From Equation (20), a passive band structure ($\varphi_0 = 0$) in absence of any phase modulation consists of a closed bandgap and Dirac points on the edges of the Brillouin Zone (see Figure 36(a)). As solitons are localized states with exponentially decaying tails, they can only exist in the presence of a bandgap, in which their propagation constant is situated [176]. As nonlinearity shifts propagation constants away from linear waves in a defined direction, a certain sign of the band curvature is mandatory for the soliton's propagation constant to reach the gap [172]. As shown in Figure 36(b), the two bands of the system feature opposite curvatures ($\varphi_0 = \pi/2$). Given that the fiber nonlinearity is positive, only the upper (focusing) band allows for soliton formation when excited in the center of the Brillouin zone by a broad Gaussian wave packet with narrow momentum spread (see red circle in Figure 36(b)). Here, an overall phase modulation of $\varphi_0 = \pi/2$ is chosen, which guarantees a broad gap of width $\Delta\theta = 2\pi/3$ and for which the upper band has a constant positive curvature in a wide momentum range and thus resembles the dispersion relation of waves propagating in bulk materials.

Consequently, provided that only a single band is excited close to the Γ point ($k_\mathrm{x} = 0, k_\mathrm{y} = 0$) and that changes between subsequent roundtrips are small, this quasi-continuous case can be covered by an effective Schrödinger equation as

$$\left[i\frac{\partial}{\partial m} + \frac{1}{4\sqrt{3}}\left(\frac{\partial^2}{\partial x^2} + \frac{\partial^2}{\partial y^2}\right) + \frac{4}{3}\chi|U|^2\right]U = 0. \tag{71}$$

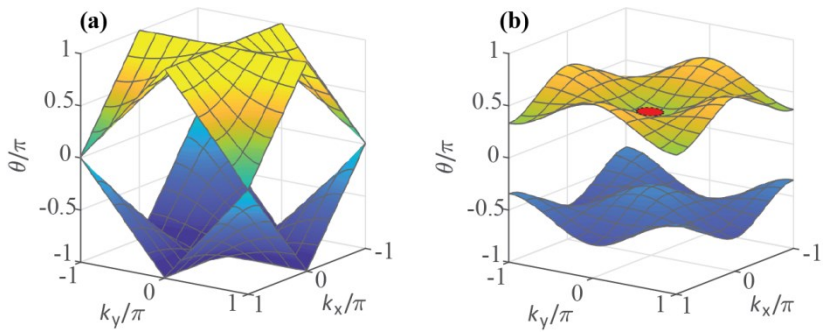

Figure 36: Band structure of the 2D mesh lattice. Due to the Floquet nature of the system, not only the Bloch momenta $\boldsymbol{k}_{x/y}$, but also the propagation constant $\boldsymbol{\theta}$ are periodic within $[-\boldsymbol{\pi}; \boldsymbol{\pi}]$. (a) Passive band structure in the absence of any phase modulation. (b) By applying a phase modulation $\boldsymbol{\varphi_0 = \pi/2}$ alternating every time step, the Dirac cone at $\boldsymbol{k}_x = \boldsymbol{k}_y = \pm\boldsymbol{\pi}$ opens up and a gap appears. The red circle on the upper (focusing) band represents a selective excitation of a Gaussian wave packet in the center of the Brillouin Zone.

It is a result of the lowest order of expansion of the band structure in the Γ point and of an averaging of the nonlinear action over two roundtrips. *U* stands for the amplitude of a unit vector of one band. Here, experiments and calculations have been performed for phase modulation of $\varphi_0 = \pi/2$.

3.2.2. 2D Solitons and Wave Collapse in a Conservative Lattice

In contrast to a single lattice site excitation, which populates the complete band structure including the upper and lower band, a specific point of the Brillouin zone is excited by a spatially broad wave packet with a narrow momentum spread. To investigate the wave propagation, a sequence of pulses is launched corresponding to a Gaussian envelope $G_w(x, y) = A_w \exp[-(x^2 + y^2)/w^2]$ along x and y-axis (see Figure 37(a)-(c)) with a variable amplitude (A_w) and a fixed width (w) of 6 positions $(1/e$ drop of intensity), where selective excitation centered on the Γ point $(k_\mathrm{x} = 0, k_\mathrm{y} = 0)$ of the upper band is realized (see Section 3.1).

At low optical power (0.3 mW), the field distribution spreads similarly to a Gaussian beam diffracting in free space (see Figure 37(d)-(f)) to a width of about 9 positions. Physically speaking, this spreading is based on pulses acquiring new positions in the time domain (compare Figure 37(d) with Figure 37(a)). For a medium power level (1 mW), the positive nonlinearity of the fiber shifts nonlinear waves into the gap, thus isolating them from the linear spectrum and providing the conditions for localization. Hence, nonlinearity starts suppressing the coupling (see Figure 37(g)), resulting in the formation of a solitonic structure (see Figure 37(h) and (i)), which propagates for up to 60 roundtrips in the experiment, provided that the initial power has been adjusted carefully.

Yet, even in computer simulations, numerically optimized soliton profiles finally decompose and either self-compress or broaden. Note that this behavior is well-known for the unstable Townes soliton of the continuous 2D NLS [192], [193]. To illuminate the soliton behavior, it is determined numerically the whole family of lattice solitons inside the bandgap (see Figure 38(k)). Following experimental conditions, the size of the computational domain was 80 positions in both x and y directions and periodic boundary conditions were used for termination. To find the solutions in an iterative way, we used an in-built MatLab iterative algorithm ("trust-region-dogleg") based on "trust regions" with the Jacobian matrix derived numerically from the objective function [45]. Throughout the calculation, nonlinear coefficient χ was fixed to unity, while the field intensity was kept unconstrained.

First, it is concentrated on the unstable Townes-like soliton that generally collapses or broadens if its energy fluctuates towards a higher or lower value, respectively. Width w, amplitude A (here $\chi = 1$), and propagation constant θ of the soliton can vary. If $w \gg 1$, the soliton enters the continuous limit, where it can be well described by the 2D NLS and thus becomes the genuine Townes soliton [172], [192]. Since the latter has an intensity profile very similar to the Gaussian function $\mathrm{G}_w(x,y) = \exp[-(x^2+y^2)/w^2]$, the numerical model uses as a trial

$$\begin{pmatrix} a_{x,y}^{m=0} \\ b_{x,y}^{m=0} \end{pmatrix} = A_w G_w(x,y) \frac{1}{\sqrt{1+|\sigma|^2}} \begin{pmatrix} \sigma \\ 1 \end{pmatrix}, \tag{72}$$

where it approximates the field distribution in the loops by the eigenvector of the upper band at the center of the first Brillouin zone and thus use σ as given by Table 1. The corresponding linear eigenvalue is $\theta_\mathrm{c} = \pi/3$ according to the notation introduced in Equation (19). The trial values of A_w and w are first guessed for the case of a very weak nonlinearly-induced change of the propagation constant $\theta_\mathrm{w} = \theta_\mathrm{c} + \delta$. Given the soliton to have a double periodicity of the lattice, the following optimization task has to be solved:

$$\begin{cases} a_{x,y}^{m=2} - a_{x,y}^{m=0} e^{i(\theta_c+\delta)} \to 0 \\ b_{x,y}^{m=2} - b_{x,y}^{m=0} e^{i(\theta_c+\delta)} \to 0 \end{cases}, \tag{73}$$

where the increment δ should be much smaller than θ_c and $(a_{x,y}^{m=2}, b_{x,y}^{m=2})$ is the field calculated after one full period.

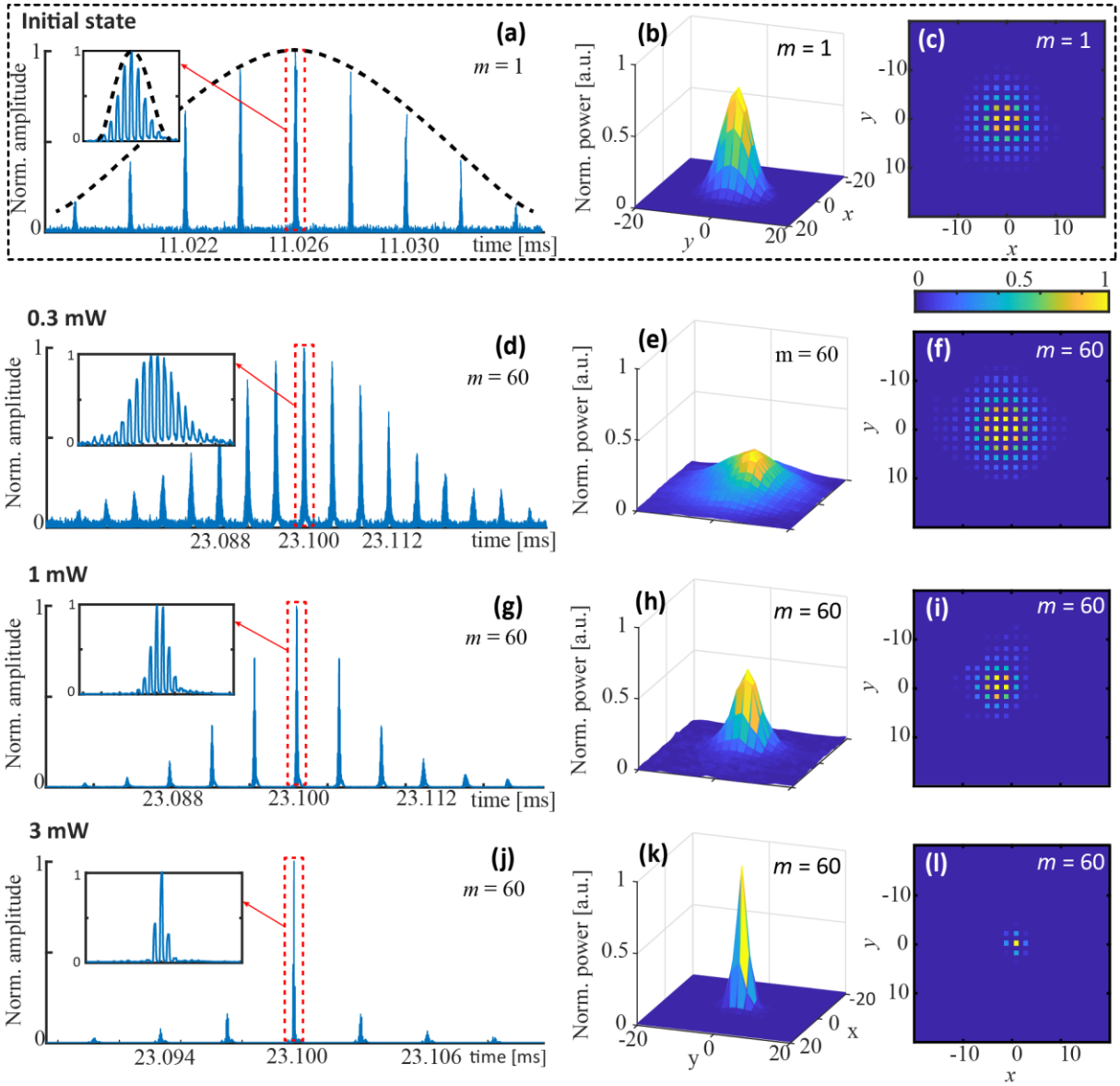

Figure 37: Experimentally detected evolution of a broad excitation in the presence of a gap ($\boldsymbol{\varphi_0 = \pi/2}$) and for different power levels demonstrating wave collapse at mW power level (bottom row). The system is excited with a sequence of pulses with a Gaussian envelope (black dashed line) as shown in the (a) time domain, (b) a 3D surface plot and (c) a 2D image with normalized scaled colors. (d)-(f) Linear diffraction of a Gaussian beam on the lattice (time step $\boldsymbol{m = 60}$, $\mathbf{0.3}$ mW input power). (g)-(i) Townes-like soliton for intermediate power (time step $\mathbf{m = 60}$, $\mathbf{1.0}$ mW input power). (j)-(l) Collapse of the field distribution into a single lattice site at the highest power level (time step $\boldsymbol{m = 60}$, $\mathbf{3}$ mW input power).

Importantly, after the optimized soliton is obtained, it is further used as a trial for searching a soliton with a slightly higher propagation constant. Next, the obtained solution is again used as a trial for a larger propagation constant, and so on until the edge of the lower band is encountered. Thus, the family of solutions is continuously traced inside the bandgap with the width $\Delta\theta = 2\pi/3$. The outcome is provided in Figure 38(k). In general, several nonlinear solutions are found, both stationary and oscillating ones. The stationary solutions return to their initial shape after the shortest recovery period of the lattice −i.e. after two

roundtrips. In contrast, the oscillating ones recover after 4 or even 6 roundtrips. In the experiments, it is always observed the Gaussian excitation evolves around stationary states and, therefore, we restrict the discussion of these solitary structures.

Two stationary structures are established: a Townes-like soliton, which tends to collapse, and an extremely localized solution, which usually marks the final state of the evolution. In the limit $\theta \to \theta_c$, the Townes-like soliton spreads to infinite width and thus converges to its continuous counterpart. However, as it investigates a limited square domain (80×80), the energy curve even shows a little increase below $\theta \approx 0.31\pi$. Unlike the continuous case, where the total energy of a Townes soliton is constant and independent of its propagation constant, discreteness causes the energy to increase with growing θ, while the width of the solution and thus the energy portion in the central spike remains almost constant (see Figure 38(k)). Although stationary, the Townes soliton is found to degrade during propagation as expected. Still, its lifetime is the highest close to the edge of the upper band ($\theta \lesssim 0.3\pi$). For propagation constants close to the upper band $\theta \to \theta_{\mathrm{linear}} = \pi/3$, solitons with infinite width are found and their shape approaching that of the continuous counterpart the Townes-like soliton. As expected, these solutions are weakly unstable, and this instability is even boosted by discreteness. However, computed lifetimes ($m > 100$) are still much larger than that accessible in the experiment, which explains the experimental accessibility.

By choosing even higher input power in the experiment (3 mW, see Figure 37(j)-(l)), nonlinear self-focusing dominates already at the beginning, thus resulting in a strong contraction of the field distribution (compare linear and nonlinear propagation plots in Figure 38(a)-(j)). As the system is inherently discrete, this collapse is stopped at the single lattice site. While some excess radiation is shed away into the lattice, most of the power remains concentrated, thus forming an extremely localized and almost stationary state (see Figure 37(j)).

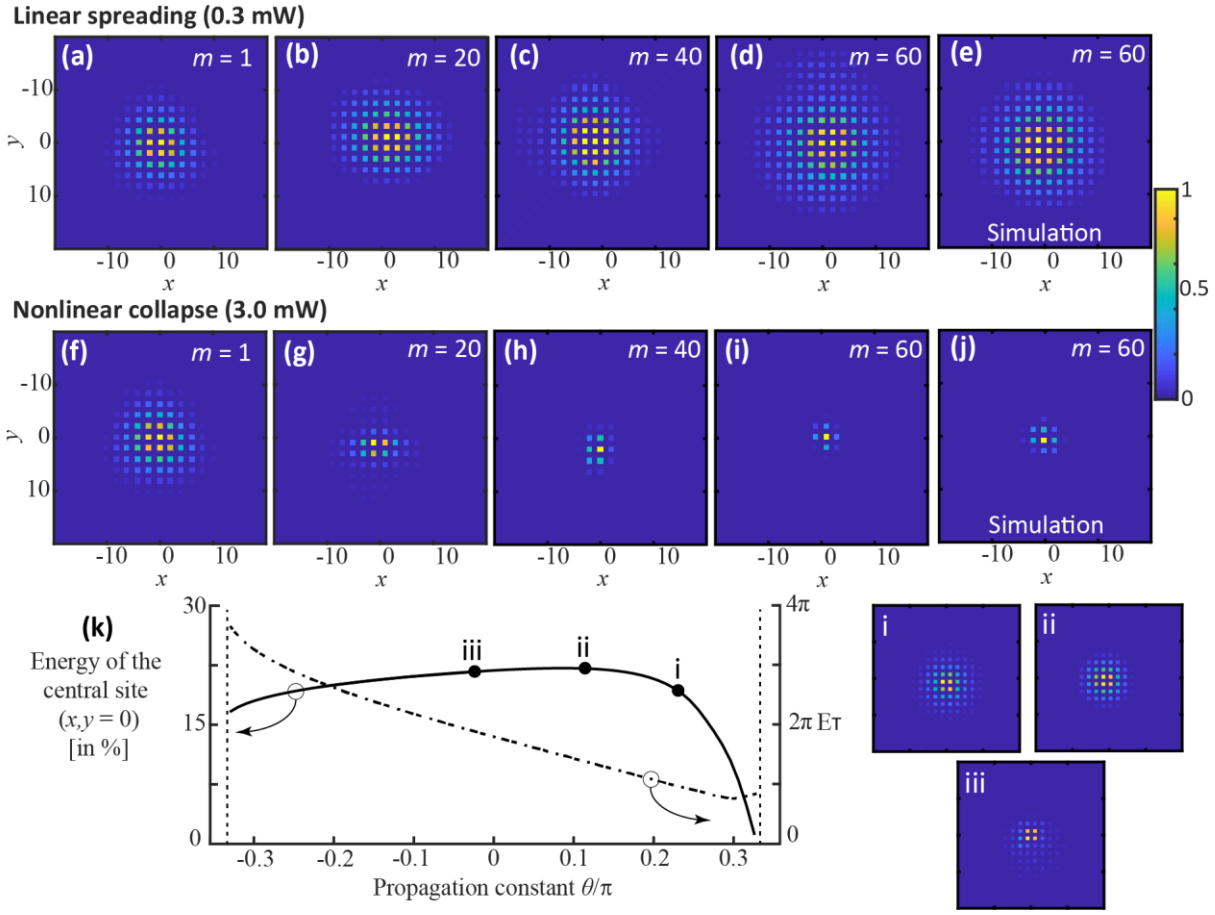

Figure 38: Propagation plots of linear (input power $\mathbf{0.3}$ mW) spreading (a)-(d) and nonlinear (input power $\mathbf{3}$ mW) collapse (f)-(i) of a broad excitation ($\boldsymbol{\varphi_0 = \pi/2}$) in agreement with (e),(j) numerical simulations. (k) The fraction of total energy situated in the central side and total energy for a numerically determined soliton profile as a function of propagation constant (nonlinear coefficients $\boldsymbol{\chi}$ was set to unity, respective soliton profiles are given on the right).

Numerically, in the lower half of the gap, any perturbation of the soliton profile results in an almost immediate blow-up of the field causing a transformation into a less energetic and more stable highly localized stationary solution. This evolution is observed both in numerical simulations and in experiments. As a collapse of the field distribution is finally terminated by discreteness above a certain power threshold, it always ends up with a highly localized stationary solution. Its power as determined numerically is almost completely concentrated in a central spike $(x, y = 0)$. Its total energy grows slowly with increasing propagation constant except for a small range of propagation constants close to the lower band edge (see Figure 38(k)). Here, the solution appears to be unstable, while for all other cases the highly localized states seem to mark the stable end-point of the evolution. Interestingly, such self-compressing instability in a time-multiplexing system corresponds to a transfer of all the energy of a sequence of pulses into a single high-power flash of light (see Figure 37(j)).

Additionally, it is worth proving that this extreme self-localization is generic to quasi-2D nonlinear systems with a gap and does not depend on the shape of the initial excitation. Given a single pulse injected into the left outer loop (see Figure 39(a)), corresponding to the center of the lattice ($x = 0, y = 0$, see Figure 39(b) and (c)), it results in the whole band structure excitation. As expected, at low input power (0.3 mW), the initial pulse spreads on the 2D photonic mesh lattice (see Figure 39(d)-(f)). Nevertheless, above a certain power threshold, diffraction is compensated and the same extremely localized state appears (see Figure 39(g)-(i)).

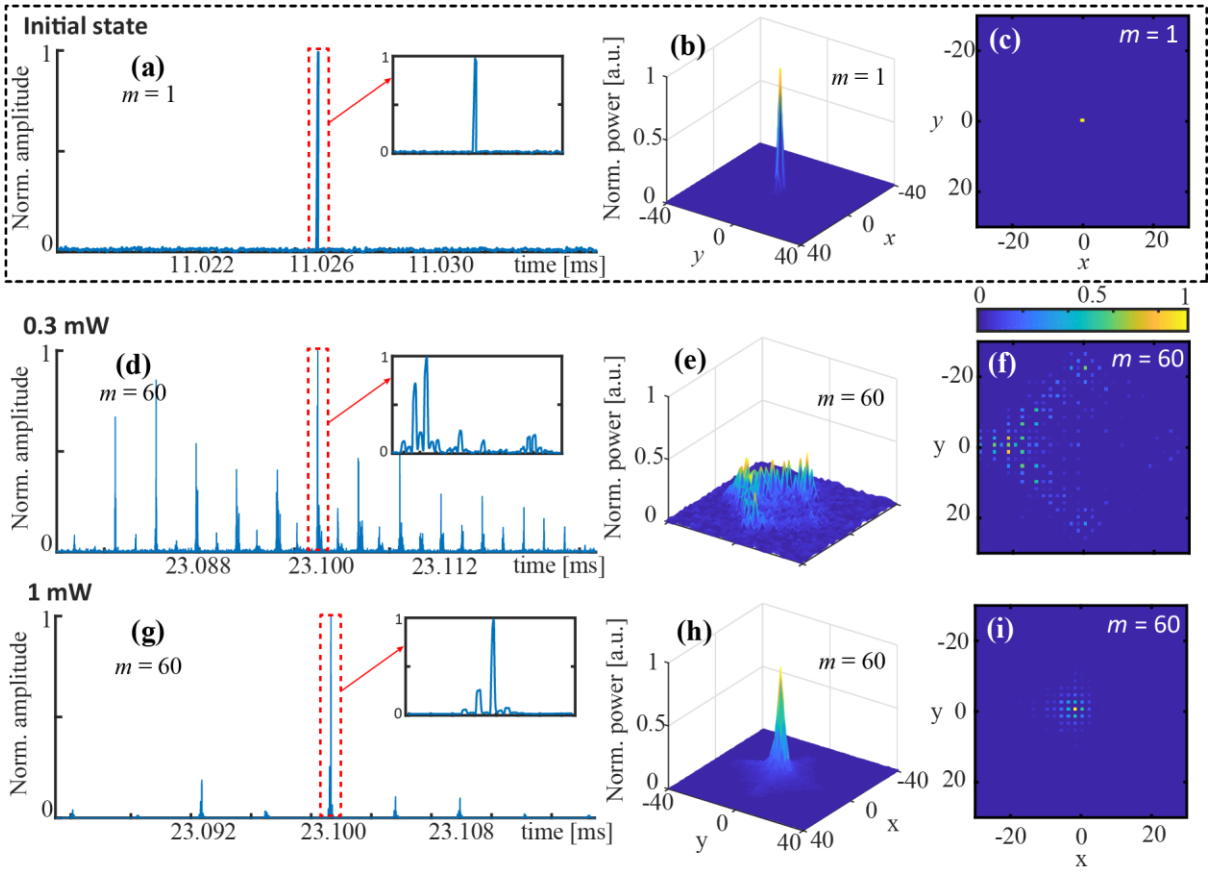

Figure 39: Evolution of a single lattice excitation in the presence of a gap ($\boldsymbol{\varphi_0 = \pi/2}$) demonstrating nonlinearly induced localization for high input power. The system is excited with a single pulse as shown in the (a) time domain, (b) a 3D surface plot, and (c) a 2D image with normalized scaled colors. (d)-(f), Linear pulse spreading onto the lattice (time step $\mathbf{m = 60}$, 0.3 mW input power). (g)-(i) Nonlinearly driven localization at a single lattice site (time step $\boldsymbol{m = 60}$, 1 mW input power).

3.3. Nonlinear Dynamics in a 2D Nonconservative Photonic Mesh Lattice

Over the last few years, parity-time ($\mathcal{PT}$) symmetry has been the focus of considerable attention [194]. Whether or not non-Hermitian Hamiltonians can still have real spectra was first proposed by Carl Bender [195], [196]. Unlike their Hermitian counterparts, nonconservative systems do not exhibit *a priori* real eigenvalues and hence unitary evolution [195]. However, once $\mathcal{PT}$ symmetry is introduced, such dissipative systems can surprisingly display a real eigenspectrum, thus ensuring energy conservation during evolution [197]. The symmetry is based on parity ($\mathcal{P}$) and time-reversal ($\mathcal{T}$) operators applied on a wave function [196]

$$\mathcal{P}\psi(x,t) = \psi(-x,t)$$
$$\mathcal{T}\psi(x,t) = \psi^*(x,-t) \tag{74}$$

where $\mathcal{P}$ flips the sign of one spatial coordinate and $\mathcal{T}$ reverses the flow of time and applies complex conjugate. Ever since, pseudo-Hermitian notions have permeated several fields ranging from optics [60], [197]–[201], to atomic and topological physics [202]–[204], optomechanics [205], electronics [206] as well as microwave photonics [207], [208], to mention a few. In optics, $\mathcal{PT}$ symmetry can be readily established by incorporating, in a balanced way, regions having an equal amount of optical gain and loss [209]. However, thus far, almost all optical realizations of $\mathcal{PT}$ symmetry have been restricted to systems with a single transverse dimension, such as, for example, arrays of optical waveguides [210], [211], and active coupled-cavity arrangements [212], [213]. In most cases, only the loss function was modulated [197], [214], [215] −a restrictive aspect that is only appropriate for linear systems.

Absorption and diffraction have always been limiting factors in fully exploiting the potential of light in both science and technology [53]. In addressing these two fundamental problems, two main avenues have been pursued: (i) optical amplification to overcome losses [177] and (ii) usage of optical solitons to compensate for dispersive forces via optical nonlinearities [51]. While each of these components alone has been successful in dealing with these issues, the combined use of these two approaches has been thus far quite challenging [172]. This is because any restoration of conservative features requires a delicate adjustment

of the spectrum. In case this condition is not met, this leads to decay or explosive amplification, which is eventually limited by gain saturation [216]. In the latter scenario, dissipative solitons can appear in the system −occasionally resting on a constant background because of stability requirements [217]. In contrast, in $\mathcal{PT}$-symmetric systems [218], [219], it is possible to restore a quasi-conservative setting that is free of such constraints. In recent years, several studies have shown that optical systems endowed with $\mathcal{PT}$ symmetry can enable unusual and previously unattainable light propagation features [60], [208], [209], [220]–[234]. These include among others, double refraction and band merging [37], [235], unidirectional invisibility [201], [236], abrupt phase transitions and power oscillations [35], [237], as well as unidirectional propagation [233], [234]. Naturally, by introducing nonlinearity, one could expect an even richer ground for new and unexpected phenomena. In this respect, it has been suggested, in several works, that entire soliton families do exist in one- and two-dimensional $\mathcal{PT}$-symmetric arrangements with Kerr nonlinearities [35], [198], [238], [239]. However, experimental observation of such effects possesses high difficulty −especially in 2D periodic configurations where soliton behavior depends critically on the lattice dimensionality [175], [240]. To some extent, one can appreciate this emerging complexity by considering the properties of the conservative nonlinear Schrödinger equation with a focusing Kerr nonlinearity [241]. While the soliton energy in the 1D system is inversely proportional to their width, in the 2D this quantity remains constant [172]. Even more importantly, in the latter case, the field distribution can undergo a catastrophic collapse, as the contraction does not require additional power [172]. In this project, these intriguing properties are experimentally observed in 2D $\mathcal{PT}$-symmetric photonic mesh lattices built through an internal gain/loss and index modulation. Besides, fiber nonlinearity enables nonlinear localization and a unique class of solitonic solutions, ultimately resulting in 2D $\mathcal{PT}$-symmetric solitons as well as the first observation of 2D self-accelerating nonlinear wave packets [70].

3.3.1. 2D $\mathcal{PT}$-symmetric Mesh Lattice

Given a 1D Schrödinger equation: $i\hbar\partial_t\psi = \mathcal{H}\psi$, where its Hamiltonian $\mathcal{H}$ is written as

$$\mathcal{H} = -\frac{\hbar}{2m}\frac{\partial^2}{\partial x^2} + V(x) \tag{75}$$

where ψ, $\hbar$ and m are the wave function, reduced Plank constant, and particle mass, respectively. The potential $V(x)$ in a $\mathcal{PT}$-symmetric condition, according to Equation (74), states that $V(\mathrm{x}) = V^*(-\mathrm{x})$ [209]. In optics, electromagnetic wave propagation under a slowly varying envelope is described by the paraxial equation:

$$i\frac{\partial E(x,z)}{\partial z} = \left[-\frac{1}{2k_0 n_0}\frac{\partial^2}{\partial x^2} + V(x)\right]E(x,z) \equiv \mathcal{H}E(x,z), \tag{76}$$

where z is the propagation distance, $E(x,z)$ denote the transverse component of the electric field and k_0 and n_0 stand for free-space wave vector and refractive index, respectively. In analogy to Equation (75), the complex optical potential $V(x) = k_0\big(n_{\mathrm{R}}(x) + in_{\mathrm{I}}(x)\big)$ is composed by real (n_{R}) and imaginary (n_{I}) part of the refractive index [194], [242], [243]. Thus, $V(x)$ under $\mathcal{PT}$-transformation is satisfied if $n(x) = n^*(-x)$ along the transverse coordinate x, where real and imaginary part [194] are written as

$$n_{\mathrm{R}}(x) = n_{\mathrm{R}}(-x) \text{ and } n_{\mathrm{I}}(x) = -n_{\mathrm{I}}(-x). \tag{77}$$

Since the two opposite sign of n_{I} represent optical gain and loss, a $\mathcal{PT}$-symmetric potential is achieved by a refractive index modulation −i.e. a balanced gain and loss profile [35], [209], [210], [244]. A similar analogy is expected also in the 2D configuration [197], [245], which is governed by the paraxial Helmholtz equation of electromagnetism for the electric field amplitude $E(x,y,z)$ [83]

$$i\frac{n_0}{2k_0}\frac{\partial E(x,y,z)}{\partial z} = -\frac{n_0}{2k_0^2}\nabla^2 E(x,y,z) - n(x,y,z)E(x,y,z), \tag{78}$$

where the $\mathcal{PT}$-symmetric configuration of the complex refractive index follows

$$n(x,y,z) = n^*(-x,-y,z). \tag{79}$$

Therefore, the real part $\Re\big(n(x,y,z)\big)$ should be mirrored to the 2D central symmetry point at $x = y$, while the imaginary part $\Im\big(n(x,y,z)\big)$ follows an antisymmetric distribution [214], [243]. In a coupled-fiber loop scheme, the 2D photonic mesh lattices featuring $\mathcal{PT}$-symmetric structure is illustrated Figure 40, in which the path A (horizontal arrows pointing to the right), path B (horizontal arrows pointing to the left), path C (vertical arrows pointing upward) and path D (horizontal arrows pointing downward) are marked by red (gain G) and

blue (loss $1/G$) colors. Similarly, the green spots on the mesh lattice represent the phase modulation with height φ_0. Note that the imaginary part of the potential satisfies the $\mathcal{PT}$ symmetry condition because that gain/loss pattern is antisymmetric concerning central symmetry point $x = y$. According to $\mathcal{PT}$ symmetry in Equation (79), the phase modulation should be symmetric with respect to a flip around the line $x = y$ and the conjugation does not change the modulation since it corresponds to the real part of the potential.

The phase modulation shown in Figure 40 extends the unit cell (compared to Figure 3(d)) for fulfilling $\mathcal{PT}$ symmetry and it corresponds to the simplest modulation scheme that only uses 4 of 8 components of the unit cell [70]. To certify that Figure 40 possesses an authentic $\mathcal{PT}$ symmetry, it is applied time-reversal $\mathcal{T}$ and then parity $\mathcal{P}$ transformations to the mesh lattice as illustrated in Figure 41. The Bloch eigenvector comprises eight components L_1, L_2, L_3, L_4, L_5, L_6, L_7 and L_8, which describes the complex amplitude in paths A and B of the unit cell (see Figure 41(a)). Note that paths C and D is not necessarily represented in this model since they are an intermediate step between $m \to m + 1$ (see Equation (16) and (17)).

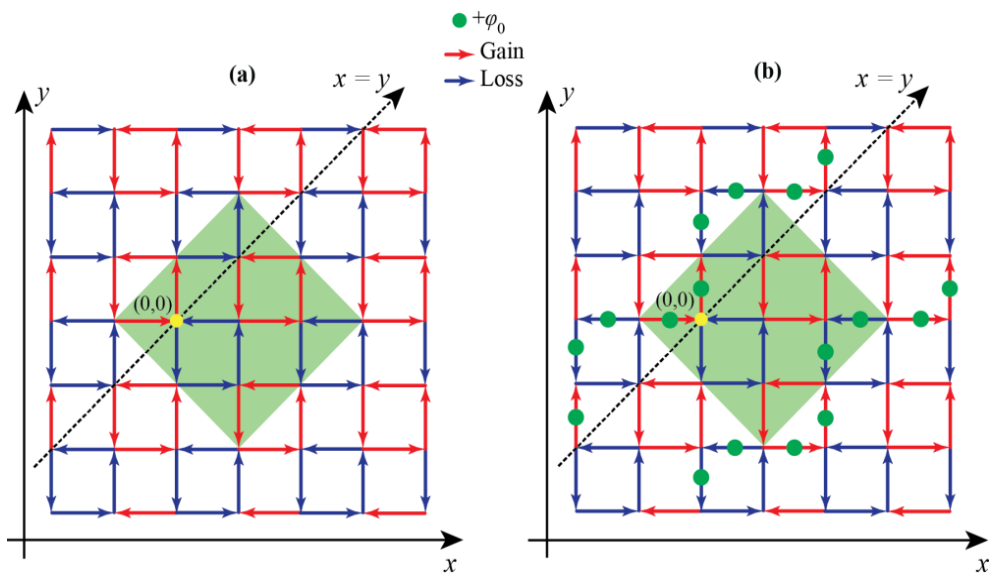

Figure 40: 2D $\mathcal{PT}$-symmetric photonic mesh lattice. (a) Arrangement of gain/loss and, (b) phase modulation potentials for fulfilling $\mathcal{PT}$ symmetry. The squared green area denotes the $\mathcal{PT}$-symmetric unit cell.

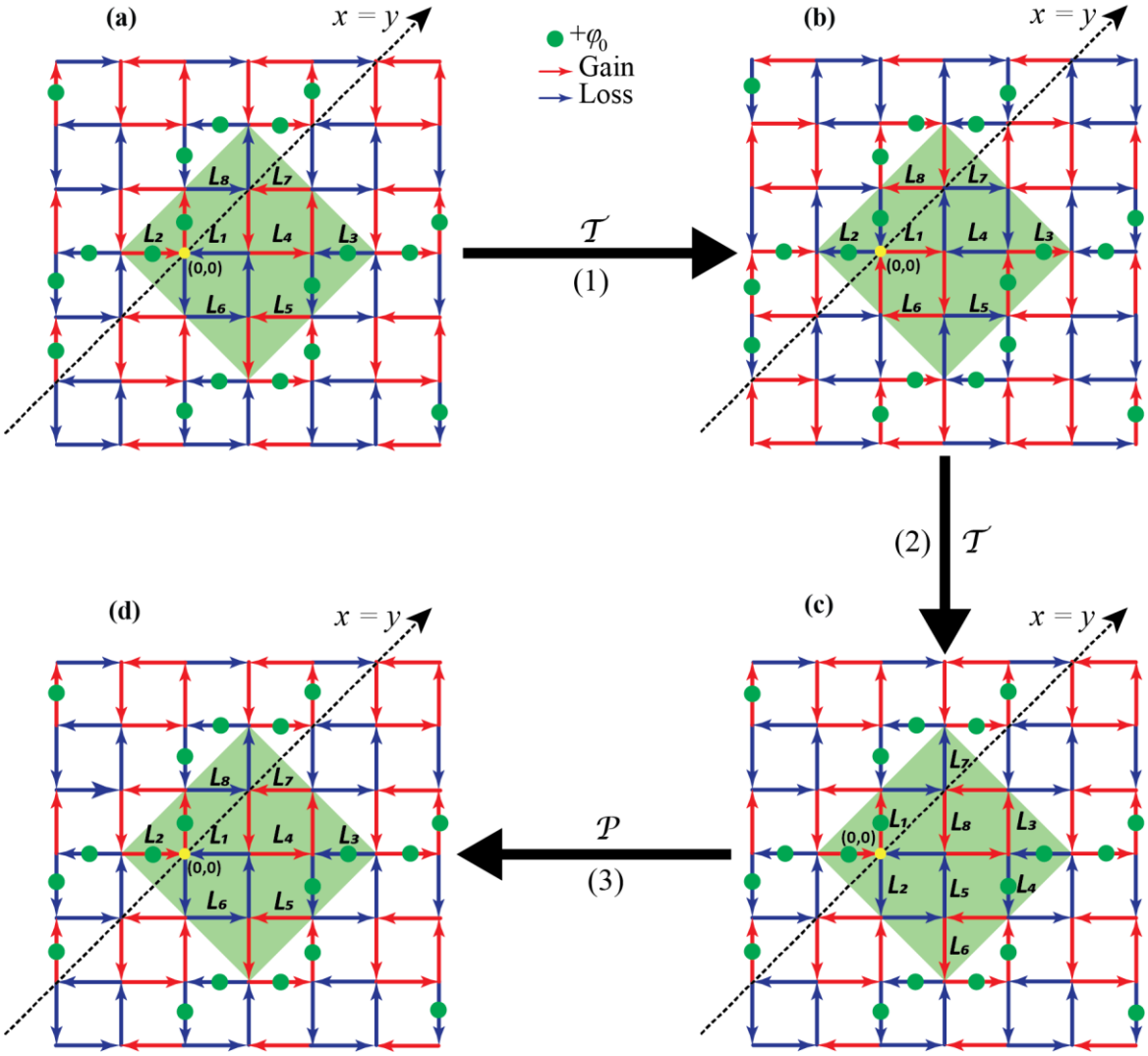

Figure 41: Retrieval of the $\mathcal{PT}$-symmetry operators for the 2D synthetic lattice in three steps. (a) $\mathcal{PT}$-symmetric mesh lattice. (b) First, the time-reversal operator flips the arrow toward opposite directions (flip of the momentum) and this in turn exchanges gain and loss (conjugation of the potential). (c) Second, the exchange of the momentum components corresponds to the flip of the mesh lattice around the line $\boldsymbol{x} = -\boldsymbol{y}$. (d) Third, the parity operator transformation brings the $\boldsymbol{C}$ and $\boldsymbol{D}$ components into A and B, respectively, yet without shifting the position.

First, the time-reversal $\mathcal{T}$ operator results in flipping the arrow toward the opposite direction (flip of the momentum), and this operation exchanges gain and loss (conjugation of the potential) (see Figure 41(b)). Subsequently, the exchange of the momentum components corresponds to the flip of the mesh lattice around the line $x = y$ (see paths A and B altering to C and D in Figure 41(c)). Finally, the exchange of the momentum components, realized through the parity $\mathcal{P}$ operator, corresponds to the flip of the mesh lattice around the line $x = y$. Therefore, the last transformation $\mathcal{P}$ is required to fulfill $\mathcal{PT}$ symmetry, which brings C and D components to A and B, respectively, but without shifting the position (see Figure 41(d)). Interestingly, this $\mathcal{PT}$-symmetric phase modulation creates zigzag-shaped potential

barriers along the mesh lattice, akin to those expected from Peierls-Nabarro (PN) effects [246], [247].

Under such $\mathcal{PT}$-symmetric configuration, the pulse dynamics in Equations (7)-(10) are rewritten to accommodate gain/loss and phase modulation. Similarly, the first part of the roundtrip represents a step to the left ($b_{x,y}^{m}$) and right ($a_{x,y}^{m}$) on the mesh lattice

$$a_{x,y}^{m} = \frac{\sqrt{G^{(-1)^m}}}{\sqrt{2}}\left(c_{x+1,y}^{m-1} + i d_{x+1,y}^{m-1}\right)\exp\left(i\frac{1}{2}\chi\left|c_{x+1,y}^{m-1} + i d_{x+1,y}^{m-1}\right|^2 + i\varphi_a(x,y)\right), \tag{80}$$

$$b_{x,y}^{m} = \frac{1}{\sqrt{2G^{(-1)^m}}}\left(d_{x-1,y}^{m-1} + i c_{x-1,y}^{m-1}\right)\exp\left(i\frac{1}{2}\chi\left|d_{x-1,y}^{m-1} + i c_{x-1,y}^{m-1}\right|^2 + i\varphi_b(x,y)\right), \tag{81}$$

whereas pulses traveling afterward through paths C ($c_{x,y}^{m}$) and D ($d_{x,y}^{m}$) move downwards or upwards. This results in the second set of evolution equations

$$c_{x,y}^{m} = \frac{\sqrt{G^{(-1)^m}}}{\sqrt{2}}\left(a_{x,y+1}^{m} + i b_{x,y+1}^{m}\right)\exp\left(i\frac{1}{2}\chi\left|a_{x,y+1}^{m} + i b_{x,y+1}^{m}\right|^2 + i\varphi_c(x,y)\right), \tag{82}$$

$$d_{x,y}^{m} = \frac{1}{\sqrt{2G^{(-1)^m}}}\left(b_{x,y-1}^{m} + i a_{x,y-1}^{m}\right)\exp\left(i\frac{1}{2}\chi\left|b_{x,y-1}^{m} + i a_{x,y-1}^{m}\right|^2 + i\varphi_d(x,y)\right). \tag{83}$$

Here, $G^{(-1)^m}$ stands for the net gain/loss introduced by the amplitude modulators (AOM and MZM), where $(-1)^m$ denotes an exchange of gain and loss after every roundtrip. For an idle transmission ratio of AOMs and MZMs of $\Upsilon = 0.8$ (see Section 1.5), all losses of the system are compensated by EDFA, thus restoring energy conservation and enabling a considerable increase in propagation steps. Still, pulses can easily be amplified [22] up to a value of $G_{MAX} = 1.25$ per round trip. The splitting ratio of both optical couplers are set to a 50/50 ratio. In each roundtrip, phase modulation protocols φ_{a}, φ_{b}, φ_{c} and φ_{d} are applied to the pulses, which depend on the position (x, y) in the lattice. Both gain/loss and phase modulation are applied to fulfill the $\mathcal{PT}$ symmetry condition. In this model, χ denotes an effective nonlinearity, in which the pulses acquire a nonlinear phase shift proportional to their optical power (see Section 1.6). Importantly, the pulses only accomplish one roundtrip after passing paths A, B, and afterward C, and D, and thus m is increased by one. Note that a pulse has to complete two roundtrips to return to its origin.

3.3.2. 2D $\mathcal{PT}$-symmetric Potential Protocols

The photonic mesh lattice with two transverse dimensions exploits the time-multiplexing technique, as described in Figure 3 and Section 1.3. The two synthetic dimensions are the result of a wise rearrangement of sequential pulses based on their arrival time, and any amplitude and phase manipulation on the 2D photonic mesh lattice is possible just by controlling those pulses in time. In this section, amplitude and phase modulation protocols are demonstrated, allowing for the experimental realization of the $\mathcal{PT}$-symmetric mesh lattice, described previously in Figure 40 and Equation (80)-(83).

According to the final schematic of $\mathcal{PT}$-symmetric potentials in Figure 40, the gain (red arrow), loss (blue arrow), and phase (green spot) potentials can be readily configured experimentally in the form of signal protocols in the time domain (see Figure 3 and Equation (6)). From Equations (80)-(83), the synthetic transverse coordinates are ascribed by path A (horizontal arrows pointing to the right), path B (horizontal arrows pointing to the left), path C (vertical arrows pointing upward) and path D (horizontal arrows pointing downward).

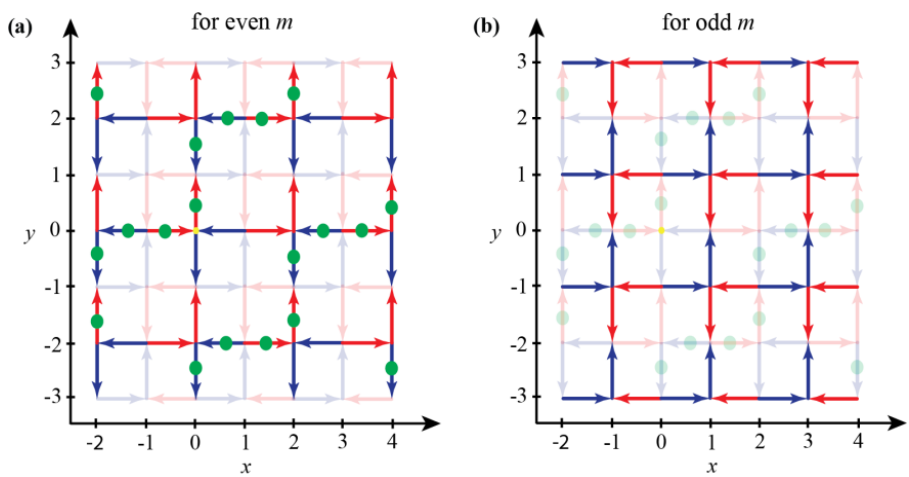

Figure 42: Separation of the mesh lattice into even and odd time steps $\boldsymbol{m}$. (a) For even $\boldsymbol{m}$, both gain/loss and phase modulation are applied. (b) For odd $\boldsymbol{m}$, only a gain/loss potential is applied.

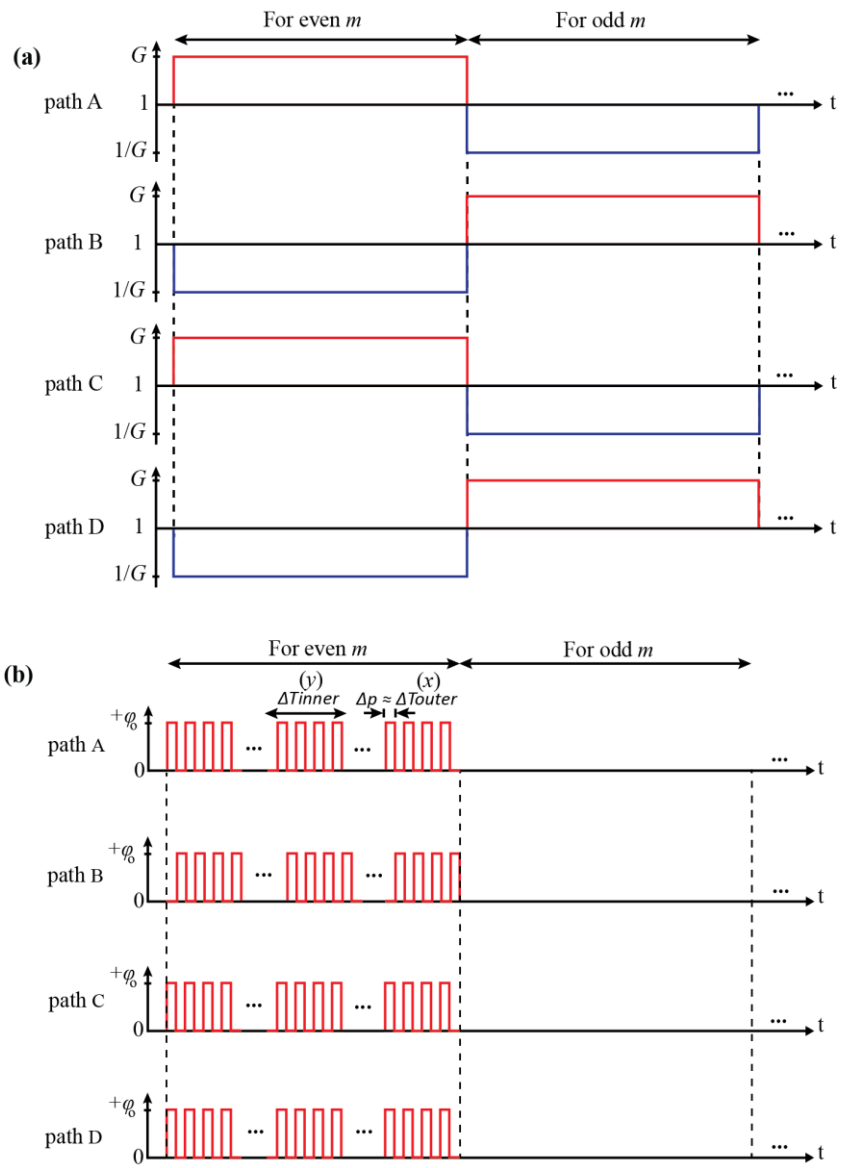

Figure 43: Experimental realization of $\mathcal{PT}$-symmetric potentials (gain/loss and phase modulation) in the form of signal protocols in the time domain. (a) Amplitude modulation arrangement emulating gain ($\boldsymbol{G}$) and loss ($\boldsymbol{1/G}$) potentials for each path. (b) Phase modulation arrangement for each path.

As mentioned, gain/loss and phase potentials are controlled in the experiment by using, respectively, amplitude and phase modulators in each loop (see Figure 7) and thus high sampling rate generators should be used to manipulate each pulse (~22 ns). In Figure 42, the 2D photonic mesh lattice is separated into even or odd time steps since the system depicts the periodicity of two. As depicted in Figure 8 and Equation (6), any position on the photonic mesh lattice on the 2D axes (x and y) can be taken in the time domain by multiplying $x.\Delta T_{\text{inner}}$ and $y.\Delta T_{\text{outer}}$, respectively. As shown in Figure 42, a gain G and loss $1/G$ are introduced in paths A and B, respectively, for every even time step m. The same pattern occurs for paths C and D. In contrast, odd time steps m, the gain and loss pattern in each path is swept (see Figure 42(a) and Figure 43(a)). In contrast to the gain/loss protocol, where the

modulation takes place on a slower time scale, the phase modulation should be varied on the position scale. For instance in Figure 42 and Figure 43(b), the phase modulation protocol applies only phase potential in the paths when a time step is an even number.

On path A, the first rolls $(y = 0)$ shows that consecutive pulses in time $(x \to x \pm 2)$ acquire a phase potential of φ_0 and 0 sequentially. In the next two rolls $(y \to y \pm 2)$, the consecutive pulses acquire a phase potential of 0 and φ_0 (mirrored). These pieces of information are understood as the phase potential (φ_0) is alternately varied in time $(x \to x \pm 2)$ with a width $\Delta p \cong \Delta T_{outer}$ during one ΔT_{inner}. For the next ΔT_{inner}, the sequential phase variation is kept the same yet mirrored. On the B path, the protocol is applied in the same way but inverted. However, path C is not mirrored concerning path D and, therefore, they display the same phase protocol as path A (see Figure 43(b)).

3.3.3. Broken and Recovered $\mathcal{PT}$-symmetric regions

The 2D photonic mesh lattice exhibits $\mathcal{PT}$ symmetry by using gain/loss and phase modulation, as shown in Figure 41. As a result of the modulation pattern, the unit cell of the lattice is doubled (see the squared green area in Figure 40) and thus the two original bands (for instance in Figure 11) of the linear spectrum split into four in total. Under linear conditions ($\chi = 0$), the band structure of the system is given by the following dispersion relation

$$\begin{aligned}\cos\theta = \pm\frac{1}{8}\Bigg(&-2\cos(g) + \cos(k_x - k_y) - 4\cos(\varphi_o)\sin^2\left(\frac{k_x + k_y}{2}\right)\\ &\pm\sqrt{2}cos\left(\frac{k_x + k_y}{2}\right)[14 - 6\cos(2\varphi_o) + 4\cos(\varphi_o - g)\\ &+4\cos(\varphi_o + g) + \cos(2\varphi_o - k_x - k_y) + 4\cos(\varphi_o + k_x - k_y)\\ &+4\cos(\varphi_o - k_x + k_y) + 4\cos(g - k_x + k_y) + 4\cos(g + k_x - k_y)\\ &-2\cos(k_x + k_y) + \cos(2\varphi_o + k_x + k_y)]^{1/2}\Bigg),\end{aligned} \tag{84}$$

which was obtained by inserting the evolution Equations (80)-(83) (following the simplification in Equations (16) and (17)) into a Floquet-Bloch ansatz of the form [55] (similarly to Equation (19)):

$$\widehat{U}_{\mathrm{PT}_{x,y}}(g,\varphi_0)e^{i(k_x x+k_y y)}\begin{pmatrix}A_1\\B_1\\A_2\\B_2\end{pmatrix}_{k_x,k_y} = e^{-i\theta}e^{i(k_x x+k_y y)}\begin{pmatrix}A_1\\B_1\\A_2\\B_2\end{pmatrix}_{k_x,k_y} . \tag{85}$$

Here $\widehat{U}_{PT_{x,y}}$ represents the evolution operator in the presence of a $\mathcal{PT}$-symmetric potential [70]. The phase and amplitude modulation intensities are denoted by φ_o and $g = -2i\ ln(G)$, respectively. θ stands for the propagation constant and k_x and k_y are the Bloch quasi momenta. The respective Bloch states are given by the double-step two-component vector $(A_{1,}, B_1, A_2, B_2)^{\mathrm{T}}_{k_x,k_y}$, which represents the field amplitudes in the inner loops for the two points contained in the unit cell of the mesh lattice[6]. Due to doubled unit cell, the Brillouin zone is reduced by half at their diagonal directions, as also visualized by $k_x \pm k_y$ from Equation (84).

Correspondingly, band structures stemming from the Floquet-Bloch theorem are demonstrated in Figure 44(a)-(f) at different φ_0 and G. As follows, $\mathcal{PT}$ symmetry is broken ($\Im(\theta) > 0$) at any $G > 1$ provided that $\varphi_0 < 0.5\pi$. On the other hand, if a phase modulation between $0.5\pi < \varphi_0 < \pi$ is applied, it eliminates the complex values, therefore, leading the system into a quasi conservative case ($\Im(\theta) = 0$, see Figure 44(d) and (e)). However, after a certain G threshold, the phase modulation cannot recover the system and thus $\mathcal{PT}$ symmetry is broken again (see Figure 44(f) and (g)).

Experimentally, the dynamics under broken and recovered band structures are shown in Figure 45. By injecting a single pulse in the C loop, which corresponding to a single point distribution at the center of the lattice ($x = y = 0$), results in an excitation of the entire band structure in momentum space −i.e. both upper and lower branches. In the passive and conservative case ($G = 1.0, \varphi_a, = \varphi_b = \varphi_c = \varphi_d = 0$), the system's eigenvalues are real (see Figure 44(a)) and hence light transport performs a 2D ballistic walk (see Figure 45(a)). However, for $G > 1.0$ and without any phase modulation, the band structure becomes complex ($\Im(\theta) > 0$) and hence $\mathcal{PT}$ symmetry is broken (Figure 44(b) and (c)) −e.i. causing the power to grow exponentially during propagation, as shown in Figure 45(b) and (c) for $\varphi_0 = 0$ and 0.3π.

[6] See Appendix C.

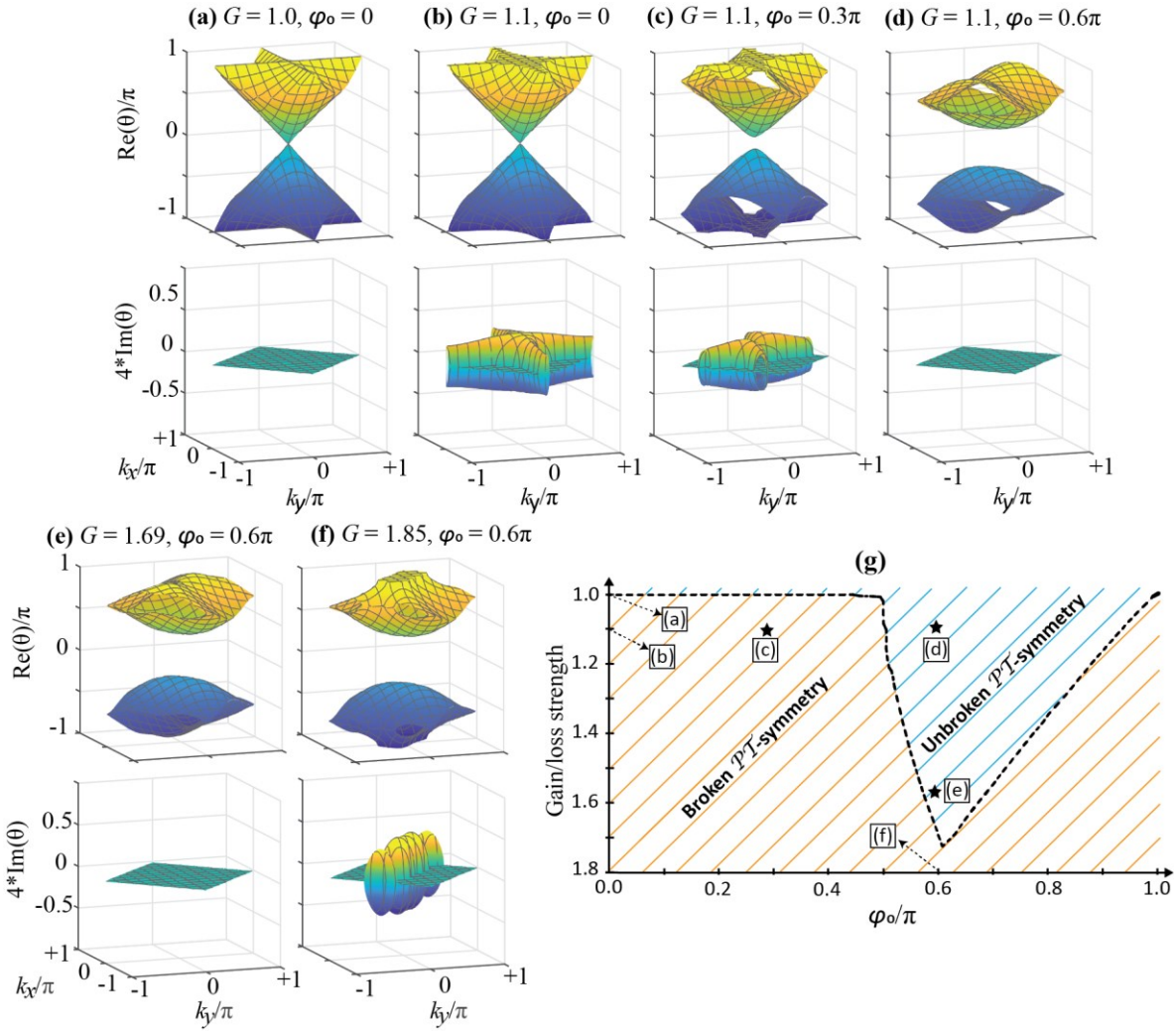

Figure 44: 2D band structures as a function of the gain/loss and phase modulation. (a) Free lattice configuration ($\boldsymbol{G = 1.0, \varphi_o = 0}$). (b)-(c) Broken $\mathcal{PT}$-symmetry ($\boldsymbol{\Im(\theta) > 0}$) when a gain $\boldsymbol{G > 1.0}$ is applied. (d)-(e) Recovered or unbroken $\mathcal{PT}$-symmetry ($\boldsymbol{\Im(\theta) = 0}$) when a recovering phase modulation of $\boldsymbol{\varphi_o = 0.6\pi}$ is applied. (f) Phase modulation cannot recover the system and $\mathcal{PT}$-symmetry is broken when $\boldsymbol{G = 1.85}$ and $\boldsymbol{\varphi_o = 0.6\pi}$. (g) Broken and recovered $\mathcal{PT}$-symmetry region as a function of gain/loss potential and phase modulation.

To restore pseudo-Hermiticity, the symmetric phase potential must be strong enough, so that $\mathcal{PT}$ symmetry is recovered (see Figure 44(d) and Figure 45(b) and (c) for $\varphi_0 = 0.6\pi$). Again, the average energy is conserved during propagation (see Figure 45(d)), which is consistent with a real-valued band structure ($\Im(\theta) = 0$). Similar to the 1D case, the phase modulation must exceed a gain/loss dependent threshold to recover the real eigenspectrum and quasi-conservative dynamics, as shown in Figure 44(g).

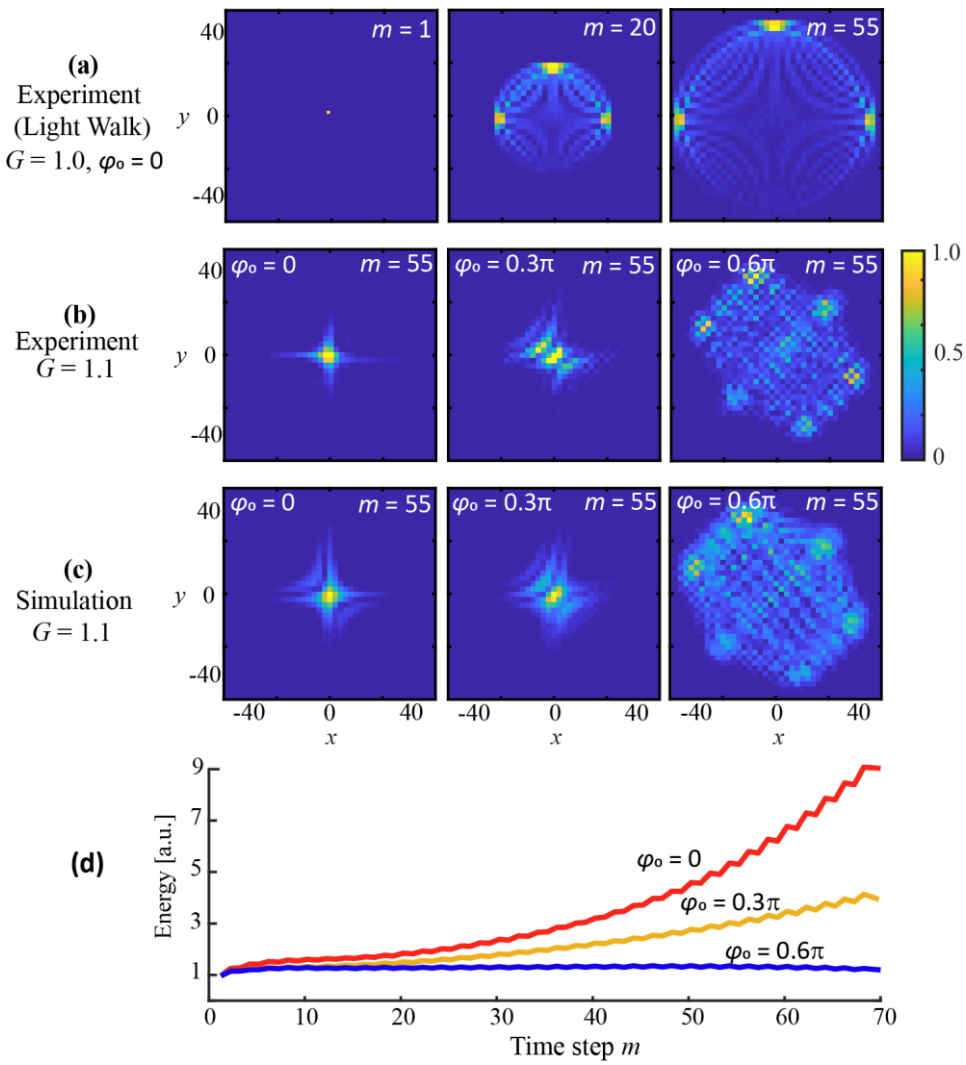

Figure 45: Evolution from a single site excitation in the presence of $\mathcal{PT}$-symmetric potentials. (a) Different propagation steps $\boldsymbol{m}$ for an experimentally realized 2D light walk in a conservative system ($\boldsymbol{G} = \mathbf{0}$) when the phase modulation is $\boldsymbol{\varphi_0} = \mathbf{0}$. (b) Experiment and (c) simulation at $\boldsymbol{m} = \mathbf{55}$ when a single site is excited in the presence of gain/loss $\boldsymbol{G} = \mathbf{1.1}$ and phase modulation $\boldsymbol{\varphi_0} = \mathbf{0}, \mathbf{0.3}\boldsymbol{\pi}$ and $\mathbf{0.6}\boldsymbol{\pi}$. The latter one leads to a pseudo-Hermitian evolution and $\mathcal{PT}$ symmetry is fulfilled. (d) Experimental observation of the energy evolving as a function of roundtrips $\boldsymbol{m}$ for $\boldsymbol{G} = \mathbf{1.1}$ and phase modulation $\boldsymbol{\varphi_0} = \mathbf{0}, \mathbf{0.3}\boldsymbol{\pi}$ and $\mathbf{0.6}\boldsymbol{\pi}$.

3.3.4. 2D $\mathcal{PT}$-solitons and Nonlinearly-driven Instability

In the range of values where $\mathcal{PT}$ symmetry is restored, where the band structure is real ($\Im(\theta) = 0$) and exhibits a bandgap, its upper dispersion branch is similar to that associated with waves propagating in a bulk material since it has a constant positive curvature over a wide range of Bloch momenta. In contrast to a single lattice site excitation (a single pulse) used before, which tends to populate all states simultaneously, a specific much narrower region in the Brillouin zone can instead be excited using a wave packet that is relatively broad in real space (see Figure 37(a)-(c)). Thus, a broad Gaussian distribution prepared by

amplitude modulation (Section 3.1) is injected into the $\mathcal{PT}$-symmetric photonic mesh lattice at the time step 2M (see Figure 35), where a particular amplitude and phase relation between paths A and B are chosen to select either upper or lower band excitation based on Equation (85). The eigenvalues of amplitude and phase, depicted in Table 2, are based on the $\mathcal{PT}$-symmetric potentials (gain/loss G and phase potential φ_0) and the exact values to excite the center ($k_x = k_y = 0$) of the focusing (upper) band consists of four amplitudes (A_1, B_1, A_2 and B_2) and phases ($\varphi_{A1}, \varphi_{B1}, \varphi_{A2}$ and φ_{B2}), which should be arranged onto the lattice as depicted in Figure 46(a). Consequently, in the time domain, each consecutive pulse on paths A and B acquire alternatively amplitude and phase coefficients, which change their order for the next ΔT_{inner} (meaning $y \rightarrow y \pm 2$) (see Figure 46(b)).

Experimentally, a broad excitation promoting a selective population within the central point Γ ($k_x = k_y = 0$) of the upper band ($G = 1.1$ and $\varphi_0 = 0.6\pi$) is carried out by launching a train of rectangular pulses comprising of a Gaussian envelope $G_{\mathrm{w}}(\mathrm{x},\mathrm{y}) = A_{\mathrm{w}}\exp[-(x^2+y^2)/w^2]$ along the synthetic x- and y-axis. In this case, variable amplitude (A_{w}) is used while the width (w) is fixed in such a way so as the $1/e$ drop in intensity occurs after 6 sites (see Figure 47(a)).

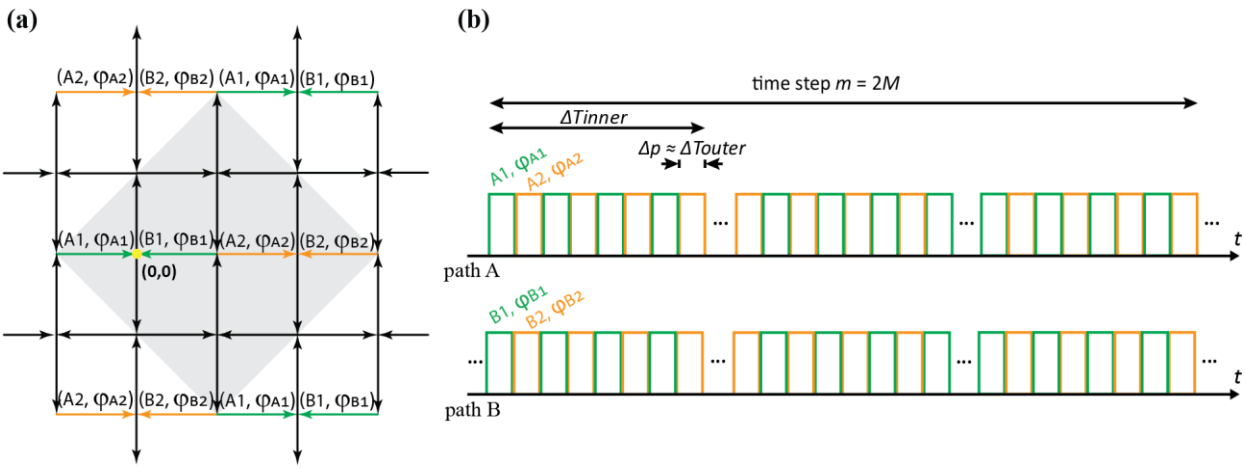

Figure 46: Amplitude and phase protocol in the (a) space and (b) time domain at the time step $\boldsymbol{m = 2M}$ of path A and B as required to excite the center of the Brillouin Zone $(\boldsymbol{k}_{\mathrm{x}} = \boldsymbol{0}, \boldsymbol{k}_{\mathrm{y}} = \boldsymbol{0})$.

Table 2: Amplitude and phase difference between the loop $\boldsymbol{A}$ and $\boldsymbol{B}$ at the time step $\boldsymbol{2M}$ in order to excite the center of the Brillouin Zone ($\boldsymbol{k_x} = \boldsymbol{k_y} = \boldsymbol{0}$) for different modulated system configurations.

G	φ_0	(A_1, B_1, A_2, B_2)	$(\varphi_{A1}, \varphi_{B1}, \varphi_{A2}, \varphi_{B2})$
1.0	0.6π	$(0.305, 0.64, 0.64, 0.305)$	$(-0.7, 0, 0, -0.7)\pi$
1.1		$(0.303, 0.615, 0.660, 0.307)$	$(-0.71, 0.007, 0, -0.68)\pi$
1.69		$(0.304, 0.573, 0.695, 0.311)$	$(-0.742, 0.022, 0, -0.649)\pi$

At an input power of approximately 0.208 mW, the field distribution experiences linear diffraction and spreads diagonally in the x-y-plane in this photonic mesh lattice (see Figure 47(c)-(e)) due to the orientation of the phase potential lines. By gradually increasing the input power to 1.1 mW, 2D $\mathcal{PT}$ solitons start to appear (see Figure 47(f)-(h)).

In the numerical simulation, a family of $\mathcal{PT}$ solitonic solutions is traced for the case $\varphi_0 = 0.6\pi$ and $G \geq 1$. In this model, the nonlinear coefficient χ is fixed to unity, so that the localized solutions originate from the positive ($\theta > 0$) focusing band. The total energy

$$E_{\mathrm{T}} = \sum_{x,y=1}^{N} \left(\left| a_{x,y} \right|^2 + \left| b_{x,y} \right|^2 \right), \tag{86}$$

is unconstrained by the solver as it can be freely varied during the optimization process since it is a nonconservative system. The size of the computational domain N is 80×80 positions, which corresponds to 40×40 elementary unit cells of the $\mathcal{PT}$-symmetric lattice. The domain has periodic boundaries in both the x and y directions. The optimization process is based on the in-built Matlab Levenberg-Marquardt algorithm [70], which aims to minimize the following nonlinear multidimensional problem:

$$\begin{cases} \left| a_{x,y}^{m=2} - a_{x,y}^{m=0} e^{i\theta} \right|^2 \to 0 \\ \left| b_{x,y}^{m=2} - b_{x,y}^{m=0} e^{i\theta} \right|^2 \to 0 \end{cases}, \tag{87}$$

where the originally two-dimensional vector $\{a_{x,y}, b_{x,y}\}_{\mathrm{x,y=1...N}}$ is preliminary stacked into a one-dimensional vector of the form $\{a_{1,1}, b_{1,1}, a_{1,2}, b_{1,2} \dots a_{1,N}, b_{1,N}, a_{2,1}, b_{2,1} \dots a_{N,N}, b_{N,N}\}$. The double step propagator for such a state is a consecutive action of a matrix $\mathrm{N}^2 \times \mathrm{N}^2$ (linear operations) and their nonlinear phase shift, depending on the amplitude distribution of the state itself, as it follows from the evolution equations in Equation (80)-(83). Function tolerance of the algorithm was typically set to 10^{-7}, although spatially narrower solutions were found to gradually destabilize at higher θ.

Therefore, their precision had to be lowered down to 10^{-5} for the algorithm to converge in a manageable time. As the initial trial function, it is chosen a radially symmetric Gaussian envelope 6 positions wide (similar to the experiments), which matches the Bloch eigenvector of the elementary unit cell to the correspondent central point ($k_x = k_y = 0$, $\theta_{\mathrm{band}} > 0$) of the upper focusing band in Equation (85). First, the parametric family of

solitons in the conservative case ($G = 1.0$ and $\varphi_0 = 0.6\pi$) is traced for further comparison. The propagation constant (θ) of the target solution is fixed slightly above the θ_{band} of the corresponding linear Bloch wave. After the solution is found, it is further chosen as a trial function for the next target solution, whose θ is again slightly increased concerning the previous one. In this way, the parametric family of solitons can be map out up to nearly $-\theta_{\text{band}}$ (see Figure 48(a)). Besides, the conservative soliton width curve along $x = y$ is shown in Figure 48(b) as a function of propagation constant. Next, as E_{T} and θ increase, the soliton gets more localized and expectedly loses its stability due to the discretization effect of the mesh lattice [176], [193], [248].

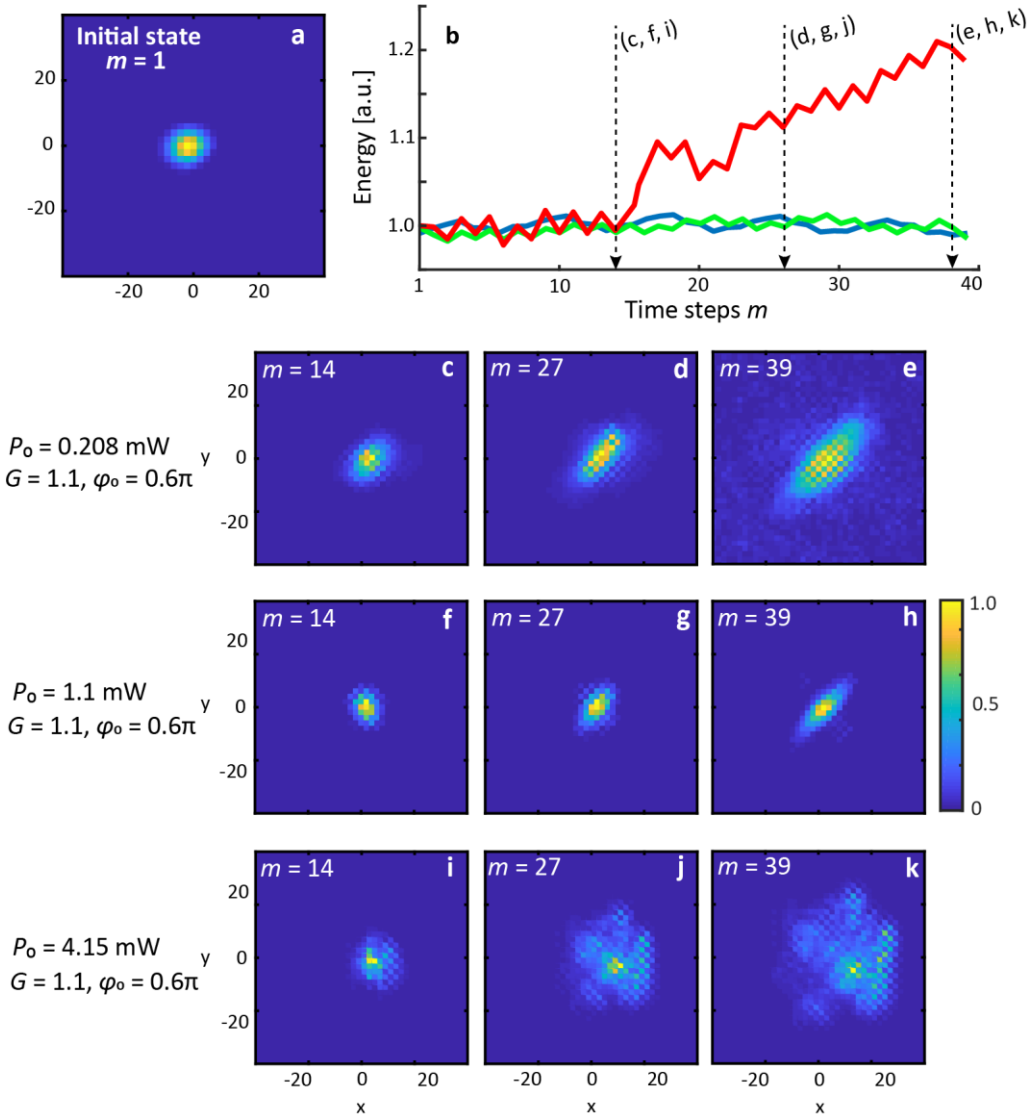

Figure 47: Experimental evolution of a broad excitation in the presence of $\mathcal{PT}$-symmetric potentials ($\boldsymbol{G} = \mathbf{1.1}; \boldsymbol{\varphi_0} = \mathbf{0.6}\boldsymbol{\pi}$). (a) 2D image of the initial Gaussian distribution at the input. (b) Experimental investigation of the energy evolution as a function of time steps $\boldsymbol{m}$ for $\mathbf{0.208}$ (blue), $\mathbf{1.1}$ (green), $\mathbf{4.15}$ mW (red) input power. (c)-(k) 2D image, displayed with normalized scaled colors, of the wave packets after $\mathbf{14}$ (c),(f),(i), $\mathbf{27}$ (d),(g),(j) and $\mathbf{40}$ (e),(h),(k) time steps $\boldsymbol{m}$ for different input powers ($\mathbf{0.208}$; $\mathbf{1.1}$ and $\mathbf{4.15}$ mW).

More specifically, a small perturbation grows exponentially and manifests itself as weak oscillations of the amplitude while the soliton propagates. At some critical point, the soliton falls into a more stable nonstationary solution, which is mostly localized at one unit cell and is bouncing between two potential walls either in the x or y directions (see Figure 48(e)). In the bandgap region, where the E_{T} growth noticeably declines ($\theta \approx 0.17\pi$), the initial stationary soliton becomes extremely unstable, meaning that the transition happens almost immediately (see Figure 48(a)).

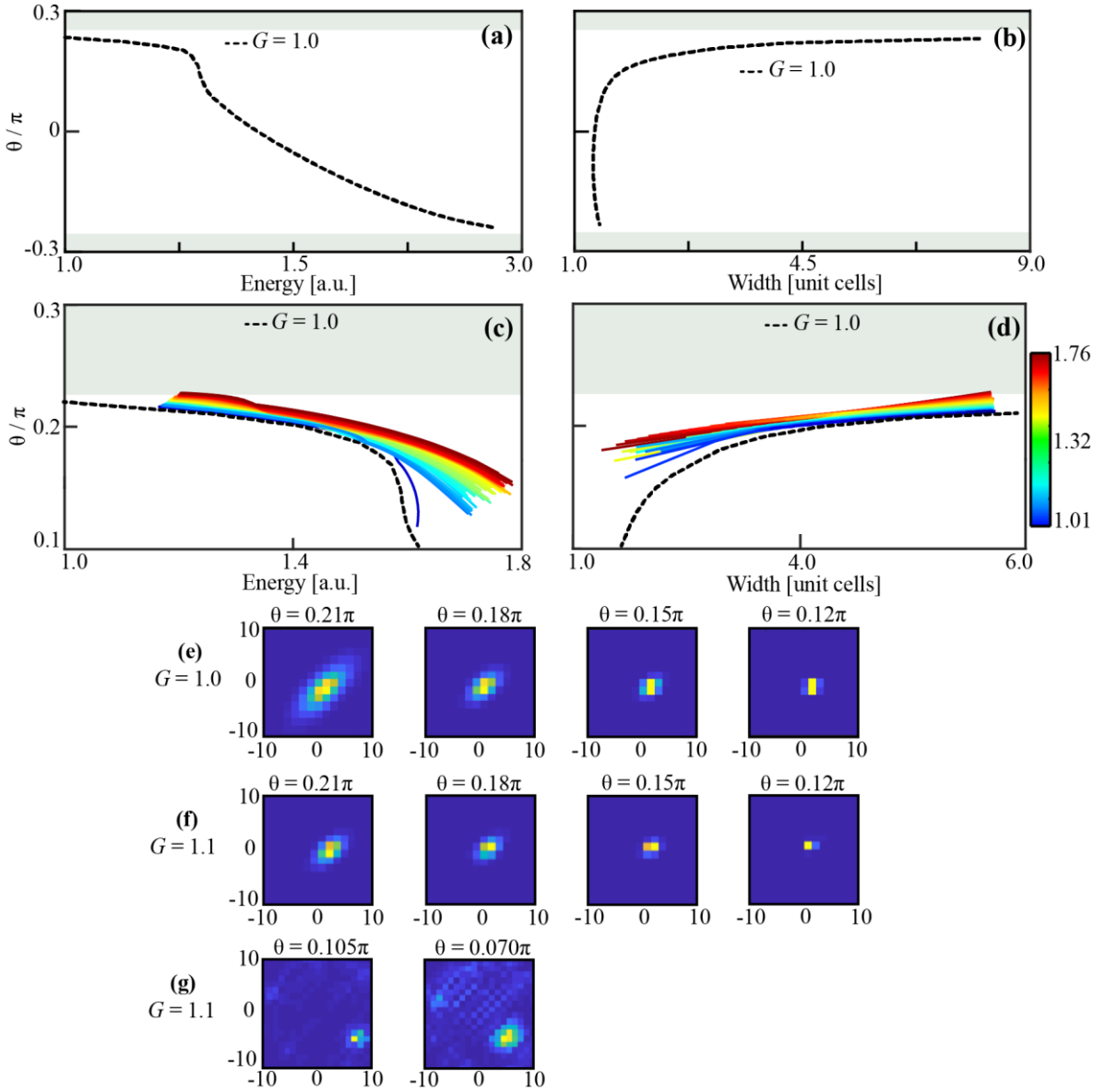

Figure 48: Numerical investigation of the conservative ($\boldsymbol{G = 1.0, \varphi_0 = 0.6\pi}$) and the non-Hermitian ($\boldsymbol{G > 1.0, \varphi_0 = 0.6\pi}$) solitons. (a) Energy of the conservative soliton as a function of $\boldsymbol{\theta}$. (b) Width of the conservative soliton as a function of $\boldsymbol{\theta}$. (c) and (d) Zoom in of (a) and (b), respectively, including the non-Hermitian case ($\boldsymbol{1.01 \leq G \leq 1.76, \varphi_0 = 0.6\pi}$). The upper and lower grey zones represent the linear bands of the system ($\boldsymbol{k_x = k_y = 0}$). (e) Conservative soliton profiles at the time step $\boldsymbol{m = 90}$ for different $\boldsymbol{\theta}$. (f) Non-Hermitian soliton profiles at the time step $\boldsymbol{m = 90}$ for different $\boldsymbol{\theta}$. (g) Soliton solutions above the energy threshold are unstable and tend to collapse.

Since the transition takes place without a substantial loss of energy, the soliton does not acquire a considerable momentum and thus it is bouncing in one particular direction. Note that the initially unstable soliton does not turn into a less energetic and more stable breather, but instead it almost adiabatically collapses into a highly localized nonstationary state, a typical process for the 2D discrete Schrödinger system (see Figure 48(e)) [172], [192], [249]. Since the transition under consideration makes the soliton abruptly shrink in space, we can similarly refer to it as a collapse event on the discrete lattice [179]. Similar to Townes-like solitons in conservative 2D nonlinear Schrödinger systems [172], [192], the 2D $\mathcal{PT}$-solitonic waves are intrinsically unstable. Figure 48(c) displays the dependence of the soliton propagation constant (eigenvalue θ) as a function of the E_{T} for both conservative ($G = 1.0$) and non-Hermitian lattice ($1.01 \leq G \leq 1.76$) [194], [218]. Note that the intensity profile of low energy soliton solutions reflects the asymmetry of the lattice showing two non-equivalent diagonal directions (see Figure 47(e) and (h) and Figure 48(e) and (f)). In contrast, high energetic solutions appear more symmetric in shape when their width almost approaches one elementary $\mathcal{PT}$ unit cell (see Figure 47(h) in the experiment and Figure 48(f) in numerical simulation), thus corresponding to a highly localized soliton trapped between two zigzag-shaped phase potential barriers (acting as a Peierls-Nabarro barrier [246], [250]).

Similarly, Figure 48(d) depicts the eigenvalue-soliton width curve, where the field distribution along the diagonal $x = y$ was fitted with a Gaussian function. Interestingly, the conservative soliton line (dotted black line) determines the threshold of the propagation constant beyond which nonconservative (i.e. $G > 1.0$) nonlinear localized stationary solutions cannot exist. As the gain/loss factor increases, the corresponding propagation constant curves for $\mathcal{PT}$ solitons proportionally decrease and their widths rapidly become narrower. As in the case of 1D $\mathcal{PT}$-symmetric photonic mesh lattices [35], [243], [251], these solitons also belong to one parametric family. Therefore, this 2D $\mathcal{PT}$ system behaves similarly to that of its Hermitian counterpart and, consequently, allows the solitons to adapt their amplitudes to their widths.

Nonconservative soliton eigenvalues present a threshold of initial total energy E_T that makes them highly unstable and immediately blows-up, releasing a large amount of energy due to their higher dissipative flux of energy for bigger gain/loss factors (see Figure 49(a)). Numerical simulations show that the soliton lifetime strongly depends on the soliton total

energy E_T and the respective gain/loss factor. Likewise, soliton maximum lifetime is quantified by the propagation time step m, at which the amplitude profile deviation

$$\delta E = \sum_{x,y=0}^{N} \left(\left| a_{x,y}^{m+2} - e^{i\theta} a_{x,y}^{m} \right|^2 + \left| b_{x,y}^{m+2} - e^{i\theta} b_{x,y}^{m} \right|^2 \right) \tag{88}$$

between two subsequent time steps m and $m + 2$ (after one modulation period) exceeds 1% of the total energy E_T (see Figure 49(b)). For those $\mathcal{PT}$-symmetric low energetic stationary soliton solutions that are relatively broad ($w = 5$ unit cells), their dimensions are noticeably larger than the step size of the lattice or its internal structure (under $\mathcal{PT}$-symmetric gain and phase modulation).

As a result, discretization effects become negligible in this quasi-continuous limit, thus allowing these otherwise unstable solitons to live for very long propagation times given that the gain/loss contrast factor is small (see Figure 49(b)). Since the Peierls-Nabarro potential is diminished, the broad soliton can diffract at the corners and slowly move along the diagonal zigzag-shaped potential without any energy loss [246], [250], [252]–[255]. In all cases, as in 1D systems [35], [198], [209], [256]–[258], non-Hermitian 2D solitons exhibit a small energy growth that is proportional to the gain/loss factor (see Figure 49(c) and (d)), although $\mathcal{PT}$ symmetry of the lattice was restored in the linear limit −a clear indication that $\mathcal{PT}$ symmetry is locally broken by nonlinearity [220], [259], [260].

Furthermore, as non-Hermitian 2D solitons propagate in this quasi-conservative system, they do not immediately disintegrate since the effective growth factor is generally much smaller than the gain/loss factor G (see Figure 49(d)). Instead, their energy exponentially grows until they collapse. Unlike the 1D systems, the rate of growth of this instability is further enhanced in a 2D environment −especially close to the collapse point where the $\mathcal{PT}$ symmetry is now violated. This is demonstrated in the experiments by further increasing the input power to ~4.15 mW, where the region of instability is reached faster and nonlinear self-focusing leads to an immediate collapse of the field distribution (see Figure 47(i)-(k)), in a way analogous to what happens in a conservative 2D discrete Schrödinger system [45], [172], [192]. Contrary to what happens in its conservative counterpart ($G = 1.0$), the non-Hermitian collapse event is followed by a fast growth of the total energy (see the red curve in Figure 47(b)), which leads to an even stronger local break in the $\mathcal{PT}$ symmetry.

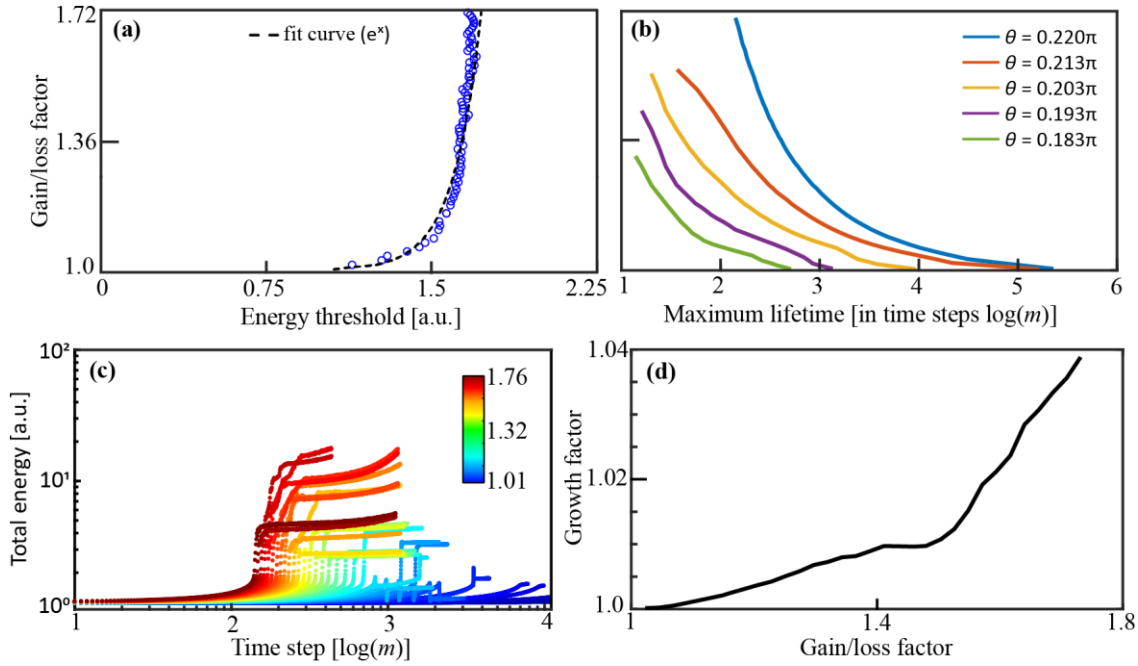

Figure 49: Nonlinearity driven instability of the solitary waves for a non-Hermitian system ($\mathbf{1.01} \geq \boldsymbol{G} \geq \mathbf{1.76}, \boldsymbol{\varphi_0} = \mathbf{0.6}\boldsymbol{\pi}$). (a) Total energy threshold and (b) maximum lifetime (in time step $\boldsymbol{m}$) as a function of gain/loss factor. (c) Higher gain/loss factors force the soliton to collapse/blow-up faster and with a proportional amount of rapidly released energy (sharp increase curve). (d) Exponential total energy growth rate before the collapse/blow-up event.

This extremely localized field is concentrated around a single lattice site and a small amount of excess radiation is released in the form of outward propagating waves (see Figure 47(i) and (j)). During the collapse, this highly localized wave nonlinearly self-accelerates and, as a result, moves on the mesh lattice (see Figure 47(k) in the experiments and Figure 48(g) in numerical simulation). Numerical simulations indicate that, in most cases, the directionality of this movement tends to be perpendicular to the zigzag-shaped $\mathcal{PT}$ phase potentials (Peierls-Nabarro barrier), meaning that the energy of the highly localized state is large enough to overcome this potential barrier. Nevertheless, due to its very small width ($w \approx 1$), this moving localized soliton experiences discretization effects from the lattice as well as the previously mentioned zigzag-shaped $\mathcal{PT}$ phase potentials. Consequently, by overcoming the phase barrier, this moving −highly localized− collapsed soliton gradually loses its energy and finally dissolves.

Conclusions and Outlook

In the course of my work, I implemented one and two transverse synthetic dimensions in a fiber optical system by using the time-multiplexing technique. The system is essentially composed of high-speed telecommunication devices and optical components connected as loops. Arriving Pulses and corresponding time delays produced by loop length differences resemble a photonic mesh lattice. Experimentally, the classical description of light as an electromagnetic wave is employed by launching high coherent optical pulses into the coupled-fiber loop, which exhibits interference effects and resembles the wave dynamics in a waveguide array.

By applying a time-periodic bell-shaped potential with a vanishing temporal average, the Kapitza guiding light effect is demonstrated in the coupled-fiber loop set-up. The results confirm the pivotal role of the fiber-based platform for demonstrating fundamental effects in wave mechanics. Future works could comprise the investigation of topological effects under the action of a spatio-temporal periodic potential and the interaction between nonlinear localization and Kapitza effective potentials.

Besides, thermalization processes in a nonlinear multimodal photonic mesh lattice are experimentally realized. These include Rayleigh-Jeans distributions with either positive or negative temperatures, isentropic expansion, and compression, as well as Joule photon-gas expansions. Exceptionally, the modal occupancy in thermal equilibrium possesses a unique temperature and chemical potential that have nothing to do with the actual thermal environment. Further works could focus on the investigation of wave transport in nonlinear structures employing thermodynamic Carnot cycles.

In addition to classical light, we proposed and experimentally validated an all-optical architecture for single-photon pairs generation and propagation. First, utilizing modulating optical switchers and exploiting fiber-based loop properties, optical bins featuring stable time delay are generated by a classical light walk. A microring resonator placed at an intermediate stage of this modified coupled-fiber loop generates time-bin single-photon pairs. These entangled photons propagate in the opposite direction of classical pulses and perform quantum interference measurements with high stability. Further works could focus on the investigation of multistage biphoton interference ($m > 3$) as well as three or more time-bins interference.

Further, we used two-dimensional photonic mesh lattices to experimentally evaluate nonlinear wave dynamics in conservative and non-Hermitian systems. Wave collapse of a

broad initial field distribution around a single lattice site is observed in such a discrete mesh lattice working at mW-power levels. By exploiting commercially available broad bandwidth photonic devices, such as amplitude and phase modulators, gain/loss, and the corresponding phase modulation, we reproduced a $\mathcal{PT}$-symmetric photonic mesh lattice. Non-conservative $\mathcal{PT}$ solitons were numerically investigated and experimentally observed in a 2D photonic mesh lattice arrangement. Non-Hermitian solitons were found to exhibit a small energy growth that is proportional to the gain/loss factor, even though $\mathcal{PT}$ symmetry of the lattice was restored in the linear limit. For higher input power levels, a family of $\mathcal{PT}$ solitons is demonstrated to self-accelerate and move during the collapse. Further works may involve 2D topological insulators for $\mathcal{PT}$-symmetric potentials.

Bibliography

[1] K. Pearson, "The problem of the random walk [3]," *Nature*, vol. 72, no. 1865. p. 294, 1905.

[2] G. F. Lawler and V. Limic, *Random Walk: A Modern Introduction*. 2010.

[3] V. M. Kendon, "A random walk approach to quantum algorithms," *Philos. Trans. R. Soc. A Math. Phys. Eng. Sci.*, vol. 364, no. 1849, pp. 3407–3422, 2006.

[4] G. H. Weiss, "Random walks and random environments, volume 1: Random walks," *J. Stat. Phys.*, vol. 82, no. 5–6, pp. 1675–1677, 1996.

[5] A. K. Geim, "Nobel Lecture: Random walk to graphene," *Rev. Mod. Phys.*, vol. 83, no. 3, pp. 851–862, 2011.

[6] A. Charles and O. Darné, "Variance-ratio tests of random walk: An overview," *Journal of Economic Surveys*, vol. 23, no. 3. pp. 503–527, 2009.

[7] N. Shenvi, J. Kempe, and K. B. Whaley, "Quantum random-walk search algorithm," *Phys. Rev. A - At. Mol. Opt. Phys.*, vol. 67, no. 5, pp. 523071–5230711, 2003.

[8] N. Perra, A. Baronchelli, D. Mocanu, B. Gonçalves, R. Pastor-Satorras, and A. Vespignani, "Random walks and search in time-varying networks," *Phys. Rev. Lett.*, vol. 109, no. 23, 2012.

[9] J. Nelson and R. E. Chandler, "Random walk models of charge transfer and transport in dye sensitized systems," *Coordination Chemistry Reviews*, vol. 248, no. 13–14. pp. 1181–1194, 2004.

[10] F. Bartumeus, M. G. E. Da Luz, G. M. Viswanathan, and J. Catalan, "Animal search strategies: A quantitative random-walk analysis," *Ecology*, vol. 86, no. 11, pp. 3078–3087, 2005.

[11] V. Kozlov and M. Y. Mitrofanova, "Galton board," *Regul. Chaotic Dyn.*, vol. 8, no. 4, pp. 431–439, 2003.

[12] N. Chernov and D. Dolgopyat, "Diffusive motion and recurrence on an idealized galton board," *Phys. Rev. Lett.*, vol. 99, no. 3, 2007.

[13] P. L. Knight, E. Roldán, and J. E. Sipe, "Quantum walk on the line as an interference phenomenon," *Phys. Rev. A - At. Mol. Opt. Phys.*, vol. 68, no. 2, p. 4, 2003.

[14] S. Simmons *et al.*, "Entanglement in a solid-state spin ensemble," *Nature*, vol. 470, no. 7332, pp. 69–72, 2011.

[15] Y. He *et al.*, "Time-Bin-Encoded Boson Sampling with a Single-Photon Device," *Phys. Rev. Lett.*, vol. 118, no. 19, 2017.

[16] S. Dong *et al.*, "Generation of hyper-entanglement in polarization/energy-time and discrete-frequency/energy-time in optical fibers," *Sci. Rep.*, vol. 5, 2015.

[17] C. Reimer, Y. Hu, M. Zhang, A. Shams-Ansari, and M. Loncar, "Quantum walks and synthetic tight-binding crystals in on-chip electro-optic frequency combs," in *2019 Conference on Lasers and Electro-Optics, CLEO 2019 - Proceedings*, 2019.

[18] A. Schreiber *et al.*, “Photons walking the line: A quantum walk with adjustable coin operations,” *Phys. Rev. Lett.*, vol. 104, no. 5, 2010.

[19] Y. Omar, N. Paunković, L. Sheridan, and S. Bose, “Quantum walk on a line with two entangled particles,” *Phys. Rev. A - At. Mol. Opt. Phys.*, vol. 74, no. 4, 2006.

[20] H. Jeong, M. Paternostro, and M. S. Kim, “Simulation of quantum random walks using the interference of a classical field,” *Phys. Rev. A - At. Mol. Opt. Phys.*, vol. 69, no. 1, p. 7, 2004.

[21] K. Manouchehri and J. B. Wang, “Continuous-time quantum random walks require discrete space,” *J. Phys. A Math. Theor.*, vol. 40, no. 45, pp. 13773–13785, 2007.

[22] A. Regensburger *et al.*, “Photon propagation in a discrete fiber network: An interplay of coherence and losses,” *Phys. Rev. Lett.*, vol. 107, no. 23, 2011.

[23] Y. Aharonov, L. Davidovich, and N. Zagury, “Quantum random walks,” *Phys. Rev. A*, vol. 48, no. 2, pp. 1687–1690, 1993.

[24] S. C. Lu, Y. Zheng, X. T. Wang, and R. B. Wu, “Quantum machine learning,” *Kongzhi Lilun Yu Yingyong/Control Theory and Applications*, vol. 34, no. 11. pp. 1429–1436, 2017.

[25] A. Montanaro, “Quantum algorithms: An overview,” *npj Quantum Information*, vol. 2, no. 1. 2016.

[26] R. Landauer, “Information is inevitably physical,” in *Feynman and Computation*, 2018, pp. 77–92.

[27] V. Zaburdaev, S. Denisov, and J. Klafter, “Lévy walks,” *Rev. Mod. Phys.*, vol. 87, no. 2, pp. 483–530, 2015.

[28] J. Biamonte, M. Faccin, and M. De Domenico, “Complex networks from classical to quantum,” *Communications Physics*, vol. 2, no. 1. 2019.

[29] G. Carleo and M. Troyer, “Solving the quantum many-body problem with artificial neural networks,” *Science (80-.).*, vol. 355, no. 6325, pp. 602–606, 2017.

[30] L. Sansoni *et al.*, “Two-particle bosonic-fermionic quantum walk via integrated photonics,” *Phys. Rev. Lett.*, vol. 108, no. 1, 2012.

[31] J. Kempe, “Quantum random walks: An introductory overview,” *Contemporary Physics*, vol. 44, no. 4. pp. 307–327, 2003.

[32] A. Schreiber, K. N. Cassemiro, V. Potoček, A. Gábris, I. Jex, and C. H. Silberhorn, “Decoherence and disorder in quantum walks: From ballistic spread to localization,” *Phys. Rev. Lett.*, vol. 106, no. 18, 2011.

[33] A. Dutt, M. Minkov, Q. Lin, L. Yuan, D. A. B. Miller, and S. Fan, “Experimental band structure spectroscopy along a synthetic dimension,” *Nat. Commun.*, vol. 10, no. 1, 2019.

[34] L. Yuan, Y. Shi, and S. Fan, “Photonic gauge potential in a system with a synthetic frequency dimension,” *Opt. Lett.*, vol. 41, no. 4, p. 741, 2016.

[35] M. Wimmer, A. Regensburger, M. A. Miri, C. Bersch, D. N. Christodoulides, and U. Peschel, “Observation of optical solitons in PT-symmetric lattices,” *Nat. Commun.*, vol. 6, 2015.

[36] A. Schreiber *et al.*, “A 2D quantum walk simulation of two-particle dynamics,” *Science (80-.).*, vol. 335, no. 6077, pp. 55–58, 2012.

[37] A. Regensburger, C. Bersch, M. A. Miri, G. Onishchukov, D. N. Christodoulides, and U. Peschel, “Parity-time synthetic photonic lattices,” *Nature*, vol. 488, no. 7410, pp. 167–171, 2012.

[38] W. A. Shay, “Time Division Multiplexing,” in *Handbook of Computer Networks*, vol. 1, 2011, pp. 568–578.

[39] L. Yuan, Q. Lin, M. Xiao, and S. Fan, “Synthetic dimension in photonics,” *arXiv*, vol. 5, no. 11, 2018.

[40] A. Goban *et al.*, “Atom-light interactions in photonic crystals,” *Nat. Commun.*, vol. 5, 2014.

[41] J. Kirchhof *et al.*, “Photonic crystal fibers,” in *Photonic Crystals: Advances in Design, Fabrication, and Characterization*, 2006, pp. 267–288.

[42] S. Z. Butler *et al.*, “Progress, challenges, and opportunities in two-dimensional materials beyond graphene,” *ACS Nano*, vol. 7, no. 4. pp. 2898–2926, 2013.

[43] J. Valentine *et al.*, “Three-dimensional optical metamaterial with a negative refractive index,” *Nature*, vol. 455, no. 7211, pp. 376–379, 2008.

[44] A. Celi *et al.*, “Synthetic gauge fields in synthetic dimensions,” *Phys. Rev. Lett.*, vol. 112, no. 4, 2014.

[45] A. L. M. Muniz, M. Wimmer, A. Bisianov, R. Morandotti, and U. Peschel, “Collapse on the line – how synthetic dimensions influence nonlinear effects,” *Sci. Rep.*, vol. 9, no. 1, 2019.

[46] H. Hodaei, M. A. Miri, M. Heinrich, D. N. Christodoulides, and M. Khajavikhan, “Parity-time-symmetric microring lasers,” *Science (80-.).*, vol. 346, no. 6212, pp. 975–978, 2014.

[47] M. Wimmer, H. M. Price, I. Carusotto, and U. Peschel, “Experimental measurement of the Berry curvature from anomalous transport,” *Nat. Phys.*, vol. 13, no. 6, pp. 545–550, 2017.

[48] T. Dauxois, P. De Buyl, L. Lori, and S. Ruffo, “Models with short-and long-range interactions: The phase diagram and the reentrant phase,” *J. Stat. Mech. Theory Exp.*, vol. 2010, no. 6, 2010.

[49] M. Karski *et al.*, “Quantum walk in position space with single optically trapped atoms,” *Science (80-.).*, vol. 325, no. 5937, pp. 174–177, 2009.

[50] A. Schreiber *et al.*, “Simulations of two particle dynamics employing dynamic coin control in 2D quantum walks,” in *2013 Conference on Lasers and Electro-Optics Europe and International Quantum Electronics Conference, CLEO/Europe-IQEC*

2013, 2013.

[51] G. Agrawal, *Nonlinear Fiber Optics*. 2006.

[52] L. Grüner-Nielsen *et al.*, "Dispersion-compensating fibers," *Journal of Lightwave Technology*, vol. 23, no. 11. pp. 3566–3579, 2005.

[53] G. P. Agrawal, *Fiber-Optic Communication Systems*. 2002.

[54] P. V. Landshoff, A. Metherell, and W. G. Rees, "Bloch waves," in *Essential Quantum Physics*, 2012, pp. 178–179.

[55] A. Gómez-León and G. Platero, "Floquet-Bloch theory and topology in periodically driven lattices," *Phys. Rev. Lett.*, vol. 110, no. 20, 2013.

[56] J. B. Pendry, "Calculating photonic band structure," *J. Phys. Condens. Matter*, vol. 8, no. 9, pp. 1085–1108, 1996.

[57] B. K. Meyer, "Band structure," in *Springer Series in Materials Science*, vol. 120, 2010, pp. 77–94.

[58] X. L. Qi and S. C. Zhang, "Topological insulators and superconductors," *Rev. Mod. Phys.*, vol. 83, no. 4, 2011.

[59] C. L. Tang, *Fundamentals of quantum mechanics: For solid state electronics and optics*, vol. 9780521829526. 2005.

[60] M. A. Miri, A. Regensburger, U. Peschel, and D. N. Christodoulides, "Optical mesh lattices with PT symmetry," *Phys. Rev. A - At. Mol. Opt. Phys.*, vol. 86, no. 2, 2012.

[61] M. Wimmer *et al.*, "Optical diametric drive acceleration through action-reaction symmetry breaking," *Nat. Phys.*, vol. 9, no. 12, pp. 780–784, 2013.

[62] A. Regensburger *et al.*, "Observation of defect states in PT-symmetric optical lattices," *Phys. Rev. Lett.*, vol. 110, no. 22, 2013.

[63] B. Hinrichs, "Feldausbreitung in photonischen Netzwerken," Diplomarbeit, Physik Department, Friedrich-Alexander-Universität Erlangen-Nürnberg, 2011.

[64] M. A. Miri, A. Regensburger, U. Peschel, and D. N. Christodoulides, "Beam dynamics in optical mesh lattices," in *2013 Conference on Lasers and Electro-Optics, CLEO 2013*, 2013.

[65] Martin Wimmer, "Nichtlineare Pulsausbreitung in einem optischen Fasernetzwerk," Masterarbeit, Physik Department, Friedrich-Alexander-Universität Erlangen-Nürnberg, 2013.

[66] M. Wimmer, M. A. Miri, D. Christodoulides, and U. Peschel, "Observation of Bloch oscillations in complex PT-symmetric photonic lattices," *Sci. Rep.*, vol. 5, 2015.

[67] M. Wimmer and U. Peschel, "Observation of Time Reversed Light Propagation by an Exchange of Eigenstates," *Sci. Rep.*, vol. 8, no. 1, 2018.

[68] A. Bisianov, M. Wimmer, U. Peschel, and O. A. Egorov, "Stability of topologically protected edge states in nonlinear fiber loops," *Phys. Rev. A*, vol. 100, no. 6, p. 63830,

2019.

[69] A. L. M. Muniz *et al.*, “Kapitza light guiding in photonic mesh lattice,” *Opt. Lett.*, vol. 44, no. 24, p. 6013, Dec. 2019.

[70] A. L. M. Muniz *et al.*, “2D Solitons in P T -Symmetric Photonic Lattices,” *Phys. Rev. Lett.*, vol. 123, no. 25, p. 253903, Dec. 2019.

[71] X. Bao and L. Chen, “Recent Progress in Distributed Fiber Optic Sensors,” *Sensors (Switzerland)*, vol. 12, no. 7. pp. 8601–8639, 2012.

[72] “Dynamical Stability of a Pendulum When Its Point of Suspension Vibrates,” in *Collected Papers of P.L. Kapitza*, 1965, pp. 714–725.

[73] S. Longhi, “Dynamic trapping of light in modulated waveguide lattices,” *Opt. Lett.*, vol. 36, no. 6, p. 819, 2011.

[74] W. Paul, “Electromagnetic traps for charged and neutral particles,” *Rev. Mod. Phys.*, vol. 62, no. 3, pp. 531–540, 1990.

[75] I. Gilary, N. Moiseyev, S. Rahav, and S. Fishman, “Trapping of particles by lasers: The quantum Kapitza pendulum,” *J. Phys. A. Math. Gen.*, vol. 36, no. 25, 2003.

[76] R. J. Cook, D. G. Shankland, and A. L. Wells, “Quantum theory of particle motion in a rapidly oscillating field,” *Phys. Rev. A*, vol. 31, no. 2, pp. 564–567, 1985.

[77] S. Rahav, I. Gilary, and S. Fishman, “Time independent description of rapidly oscillating potentials,” *Phys. Rev. Lett.*, vol. 91, no. 11, 2003.

[78] A. Alberucci, L. Marrucci, and G. Assanto, “Light confinement via periodic modulation of the refractive index,” *New J. Phys.*, vol. 15, 2013.

[79] C. Rizza and A. Ciattoni, “Effective medium theory for kapitza stratified media: Diffractionless propagation,” *Phys. Rev. Lett.*, vol. 110, no. 14, 2013.

[80] B. T. Torosov, G. Della Valle, and S. Longhi, “Imaginary Kapitza pendulum,” *Phys. Rev. A - At. Mol. Opt. Phys.*, vol. 88, no. 5, 2013.

[81] C. P. Jisha, A. Alberucci, L. Marrucci, and G. Assanto, “Interplay between diffraction and the Pancharatnam-Berry phase in inhomogeneously twisted anisotropic media,” *Phys. Rev. A*, vol. 95, no. 2, 2017.

[82] A. Zheltikov, “Laser-induced tunneling, the Kapitza effective potential, and the limits of perturbative nonlinear optics,” *Opt. Express*, vol. 27, no. 6, p. 8246, 2019.

[83] S. Longhi, “Quantum-optical analogies using photonic structures,” *Laser and Photonics Reviews*, vol. 3, no. 3. pp. 243–261, 2009.

[84] J. Hu and C. R. Menyuk, “Understanding leaky modes: Slab waveguide revisited,” *Opt. InfoBase Conf. Pap.*, vol. 1, no. 1, pp. 58–106, 2009.

[85] A. Ridinger and N. Davidson, “Particle motion in rapidly oscillating potentials: The role of the potential’s initial phase,” *Phys. Rev. A - At. Mol. Opt. Phys.*, vol. 76, no. 1, 2007.

[86] S. Braun *et al.*, “Negative absolute temperature for motional degrees of freedom,” *Science (80-.).*, vol. 339, no. 6115, pp. 52–55, 2013.

[87] F. O. Wu, A. U. Hassan, and D. N. Christodoulides, “Thermodynamic theory of highly multimoded nonlinear optical systems,” *Nat. Photonics*, vol. 13, no. 11, pp. 776–782, 2019.

[88] S. A. Derevyanko, “Thermalized polarization dynamics of a discrete optical-waveguide system with four-wave mixing,” *Phys. Rev. A - At. Mol. Opt. Phys.*, vol. 88, no. 3, 2013.

[89] T. Kottos and B. Shapiro, “Thermalization of strongly disordered nonlinear chains,” *Phys. Rev. E - Stat. Nonlinear, Soft Matter Phys.*, vol. 83, no. 6, 2011.

[90] P. Aschieri, J. Garnier, C. Michel, V. Doya, and A. Picozzi, “Condensation and thermalization of classsical optical waves in a waveguide,” *Phys. Rev. A - At. Mol. Opt. Phys.*, vol. 83, no. 3, 2011.

[91] M. Parto, F. O. Wu, P. S. Jung, K. Makris, and D. N. Christodoulides, “Thermodynamic conditions governing the optical temperature and chemical potential in nonlinear highly multimoded photonic systems,” *arXiv*, 2019.

[92] S. Varró, “A Study on Black-Body Radiation: Classical and Binary Photons,” *Acta Phys. Hungarica A) Heavy Ion Phys.*, vol. 26, no. 3–4, pp. 365–389, 2006.

[93] K. Krupa *et al.*, “Spatial beam self-cleaning in multimode fibres,” *Nat. Photonics*, vol. 11, no. 4, pp. 237–241, 2017.

[94] L. G. Wright, Z. Liu, D. A. Nolan, M. J. Li, D. N. Christodoulides, and F. W. Wise, “Self-organized instability in graded-index multimode fibres,” *Nat. Photonics*, vol. 10, no. 12, pp. 771–776, 2016.

[95] D. N. Christodoulides, F. Lederer, and Y. Silberberg, “Discretizing light behaviour in linear and nonlinear waveguide lattices,” *Nature*, vol. 424, no. 6950. pp. 817–823, 2003.

[96] S. Fan and J. M. Kahn, “Principal modes in multimode waveguides,” *Opt. Lett.*, vol. 30, no. 2, p. 135, 2005.

[97] J. Klaers, J. Schmitt, F. Vewinger, and M. Weitz, “Bose-Einstein condensation of photons in an optical microcavity,” *Nature*, vol. 468, no. 7323, pp. 545–548, 2010.

[98] A. Yariv, Y. Xu, R. K. Lee, and A. Scherer, “Coupled-resonator optical waveguide:?a proposal and analysis,” *Opt. Lett.*, vol. 24, no. 11, p. 711, 1999.

[99] S. Longhi, “Modulational instability and space time dynamics in nonlinear parabolic-index optical fibers,” *Opt. Lett.*, vol. 28, no. 23, p. 2363, 2003.

[100] K. Krupa *et al.*, “Observation of Geometric Parametric Instability Induced by the Periodic Spatial Self-Imaging of Multimode Waves,” *Phys. Rev. Lett.*, vol. 116, no. 18, 2016.

[101] H. E. Lopez-Aviles *et al.*, “A systematic analysis of parametric instabilities in nonlinear parabolic multimode fibers,” *APL Photonics*, vol. 4, no. 2, 2019.

[102] G. Lopez-Galmiche *et al.*, “Visible supercontinuum generation in a graded index multimode fiber pumped at 1064 nm,” *Opt. Lett.*, vol. 41, no. 11, p. 2553, 2016.

[103] L. G. Wright, D. N. Christodoulides, and F. W. Wise, “Spatiotemporal mode-locking in multimode fiber lasers,” *Science (80-.).*, vol. 358, no. 6359, pp. 94–97, 2017.

[104] N. R. Thompson and B. W. J. McNeil, “Mode locking in a free-electron laser amplifier,” *Phys. Rev. Lett.*, vol. 100, no. 20, 2008.

[105] V. Brasch *et al.*, “Photonic chip-based optical frequency comb using soliton Cherenkov radiation,” *Science (80-.).*, vol. 351, no. 6271, pp. 357–360, 2016.

[106] W. H. Renninger and F. W. Wise, “Optical solitons in graded-index multimode fibres,” *Nat. Commun.*, vol. 4, 2013.

[107] L. G. Wright, D. N. Christodoulides, and F. W. Wise, “Controllable spatiotemporal nonlinear effects in multimode fibres,” *Nat. Photonics*, vol. 9, no. 5, pp. 306–310, 2015.

[108] M. Mitchell, M. Segev, T. H. Coskun, and D. N. Christodoulides, “Theory of self-trapped spatially incoherent light beams,” *Phys. Rev. Lett.*, vol. 79, no. 25, pp. 4990–4993, 1997.

[109] A. Picozzi *et al.*, “Optical wave turbulence: Towards a unified nonequilibrium thermodynamic formulation of statistical nonlinear optics,” *Physics Reports*, vol. 542, no. 1. pp. 1–132, 2014.

[110] N. F. Ramsey, “Thermodynamics and statistical mechanics at negative absolute temperatures,” *Phys. Rev.*, vol. 103, no. 1, pp. 20–28, 1956.

[111] G. Agrawal, *Nonlinear Fiber Optics*. 2006.

[112] J. M. Stone, F. Yu, and J. C. Knight, “Highly birefringent 98-core fiber,” *Opt. Lett.*, vol. 39, no. 15, p. 4568, 2014.

[113] T. Moriya, K. Murano, and H. Gambe, “Digital Signal Processing.,” in *Fujitsu Scientific and Technical Journal*, vol. 22, no. 4, 1986, pp. 343–353.

[114] M. Teixeira and V. Zaharov, “Digital Transmission,” in *Handbook of Computer Networks*, vol. 1, 2011, pp. 84–101.

[115] K. Kikuchi, “Fundamentals of coherent optical fiber communications,” *Journal of Lightwave Technology*, vol. 34, no. 1. pp. 157–179, 2016.

[116] J. O’Neal, “Introduction to Signal Transmission,” *IEEE Trans. Commun.*, vol. 20, no. 5, pp. 1046–1047, 2004.

[117] International Telecommunication Union, “Overview of the Internet of things,” *Ser. Y Glob. Inf. infrastructure, internet Protoc. Asp. next-generation networks - Fram. Funct. Archit. Model.*, p. 22, 2012.

[118] S. Li, L. Da Xu, and S. Zhao, “The internet of things: a survey,” *Inf. Syst. Front.*, vol. 17, no. 2, pp. 243–259, 2015.

[119] I. Lee and K. Lee, “The Internet of Things (IoT): Applications, investments, and

challenges for enterprises," *Bus. Horiz.*, vol. 58, no. 4, pp. 431–440, 2015.

[120] T. S. Rappaport *et al.*, "Millimeter wave mobile communications for 5G cellular: It will work!," *IEEE Access*, vol. 1, pp. 335–349, 2013.

[121] IEEE 5G, "IEEE 5G and beyond technology roadmap," 2017.

[122] Reuters, "Samsung spurs R&D efforts for 6G before 5G becomes mainstream," *Mint*, 2019.

[123] K. David and H. Berndt, "6G Vision and requirements: Is there any need for beyond 5g?," *IEEE Veh. Technol. Mag.*, vol. 13, no. 3, pp. 72–80, 2018.

[124] K. M S and D. K. Vali, "A Survey on Evolution of Mobile Communication from 1G to 7G," *Int. J. Multidiscip. Curr. Res.*, pp. 391–397, 2018.

[125] B. Parthasarathy, "Information Technology," in *International Encyclopedia of Human Geography*, 2009, pp. 469–474.

[126] A. Aspuru-Guzik and P. Walther, "Photonic quantum simulators," *Nature Physics*, vol. 8, no. 4. pp. 285–291, 2012.

[127] S. Lloyd and S. L. Braunstein, "Quantum computation over continuous variables," *Phys. Rev. Lett.*, vol. 82, no. 8, pp. 1784–1787, 1999.

[128] B. P. Lanyon *et al.*, "Measurement-based quantum computation with trapped ions," *Phys. Rev. Lett.*, vol. 111, no. 21, 2013.

[129] M. Förtsch *et al.*, "A versatile source of single photons for quantum information processing," *Nat. Commun.*, vol. 4, 2013.

[130] M. Veldhorst *et al.*, "A two-qubit logic gate in silicon," *Nature*, vol. 526, no. 7573, pp. 410–414, 2015.

[131] Y. Wang, "Quantum computation and quantum information," *Stat. Sci.*, vol. 27, no. 3, pp. 373–394, 2012.

[132] P. Roztocki *et al.*, "Kerr combs and telecommunications components for the generation and high-dimensional quantum processing of d-level cluster states," in *International Conference on Transparent Optical Networks*, 2019, vol. 2019-July.

[133] M. Kues *et al.*, "On-chip generation of high-dimensional entangled quantum states and their coherent control," *Nature*, vol. 546, no. 7660, pp. 622–626, 2017.

[134] T. Monz *et al.*, "14-qubit entanglement: Creation and coherence," *Phys. Rev. Lett.*, vol. 106, no. 13, 2011.

[135] E. Togan *et al.*, "Quantum entanglement between an optical photon and a solid-state spin qubit," *Nature*, vol. 466, no. 7307, pp. 730–734, 2010.

[136] J. Roslund, R. M. De Araújo, S. Jiang, C. Fabre, and N. Treps, "Wavelength-multiplexed quantum networks with ultrafast frequency combs," *Nat. Photonics*, vol. 8, no. 2, pp. 109–112, 2014.

[137] K. De Greve *et al.*, "Quantum-dot spin-photon entanglement via frequency

downconversion to telecom wavelength," *Nature*, vol. 491, no. 7424, pp. 421–425, 2012.

[138] X. C. Yao *et al.*, "Observation of eight-photon entanglement," *Nat. Photonics*, vol. 6, no. 4, pp. 225–228, 2012.

[139] C. Reimer *et al.*, "High-dimensional one-way quantum processing implemented on d-level cluster states," *Nature Physics*, vol. 15, no. 2. pp. 148–153, 2019.

[140] W. K. Wootters, "Entanglement of formation of an arbitrary state of two qubits," *Phys. Rev. Lett.*, vol. 80, no. 10, pp. 2245–2248, 1998.

[141] R. Horodecki, P. Horodecki, M. Horodecki, and K. Horodecki, "Quantum entanglement," *Rev. Mod. Phys.*, vol. 81, no. 2, pp. 865–942, 2009.

[142] "Logic gates," *Data Handl. Sci. Technol.*, vol. 1, no. C, pp. 30–55, 1984.

[143] D. Loss and D. P. DiVincenzo, "Quantum computation with quantum dots," *Phys. Rev. A - At. Mol. Opt. Phys.*, vol. 57, no. 1, pp. 120–126, 1998.

[144] A. Barenco *et al.*, "Elementary gates for quantum computation," *Phys. Rev. A*, vol. 52, no. 5, pp. 3457–3467, 1995.

[145] D. P. DiVincenzo and D. Loss, "Coupled quantum dots as quantum gates," *Phys. Rev. B - Condens. Matter Mater. Phys.*, vol. 59, no. 3, pp. 2070–2078, 1999.

[146] H. L. Yin *et al.*, "Measurement-Device-Independent Quantum Key Distribution over a 404 km Optical Fiber," *Phys. Rev. Lett.*, vol. 117, no. 19, 2016.

[147] R. Blatt and C. F. Roos, "Quantum simulations with trapped ions," *Nature Physics*, vol. 8, no. 4. pp. 277–284, 2012.

[148] D. Leibfried, R. Blatt, C. Monroe, and D. Wineland, "Quantum dynamics of single trapped ions," *Reviews of Modern Physics*, vol. 75, no. 1. pp. 281–324, 2003.

[149] E. Knill, R. Laflamme, and G. J. Milburn, "A scheme for efficient quantum computation with linear optics," *Nature*, vol. 409, no. 6816, pp. 46–52, 2001.

[150] A. M. Childs, D. Gosset, and Z. Webb, "Universal computation by multiparticle quantum walk," *Science (80-.).*, vol. 339, no. 6121, pp. 791–794, 2013.

[151] A. Peruzzo *et al.*, "Quantum walks of correlated photons," *Science (80-.).*, vol. 329, no. 5998, pp. 1500–1503, 2010.

[152] J. L. O'Brien, G. J. Pryde, A. G. White, T. C. Ralph, and D. Branning, "Demonstration of an all-optical quantum controlled-NOT gate," *Nature*, vol. 426, no. 6964, pp. 264–267, 2003.

[153] J. Romero, J. P. Olson, and A. Aspuru-Guzik, "Quantum autoencoders for efficient compression of quantum data," *Quantum Sci. Technol.*, vol. 2, no. 4, 2017.

[154] T. Pittman, "It's a Good Time for Time-Bin Qubits," *Physics (College. Park. Md).*, vol. 6, 2013.

[155] P. C. Humphreys *et al.*, "Linear optical quantum computing in a single spatial mode,"

Phys. Rev. Lett., vol. 111, no. 15, 2013.

[156] A. Martin, F. Kaiser, A. Vernier, A. Beveratos, V. Scarani, and S. Tanzilli, "Cross time-bin photonic entanglement for quantum key distribution," *Phys. Rev. A - At. Mol. Opt. Phys.*, vol. 87, no. 2, 2013.

[157] C. Reimer *et al.*, "Generation of multiphoton entangled quantum states by means of integrated frequency combs," *Science (80-.).*, vol. 351, no. 6278, pp. 1176–1180, 2016.

[158] P. P. Rohde, "Simple scheme for universal linear-optics quantum computing with constant experimental complexity using fiber loops," *Phys. Rev. A - At. Mol. Opt. Phys.*, vol. 91, no. 1, 2015.

[159] A. C. Dada, J. Leach, G. S. Buller, M. J. Padgett, and E. Andersson, "Experimental high-dimensional two-photon entanglement and violations of generalized Bell inequalities," *Nat. Phys.*, vol. 7, no. 9, pp. 677–680, 2011.

[160] H. Jayakumar, A. Predojević, T. Kauten, T. Huber, G. S. Solomon, and G. Weihs, "Time-bin entangled photons from a quantum dot," *Nat. Commun.*, vol. 5, 2014.

[161] C. Wang *et al.*, "Ultrahigh-efficiency second-harmonic generation in nanophotonic PPLN waveguides," *arXiv*, 2018.

[162] S. Tanzilli *et al.*, "PPLN waveguide for quantum communication," in *European Physical Journal D*, 2002, vol. 18, no. 2, pp. 155–160.

[163] F. Boitier, A. Godard, N. Dubreuil, P. Delaye, C. Fabre, and E. Rosencher, "Two-photon-counting interferometry," *Phys. Rev. A - At. Mol. Opt. Phys.*, vol. 87, no. 1, 2013.

[164] S. P. Walborn, A. N. de Oliveira, S. Pádua, and C. H. Monken, "Multimode Hong-Ou-Mandel Interference," *Phys. Rev. Lett.*, vol. 90, no. 14, p. 4, 2003.

[165] A. Sipahigil *et al.*, "Indistinguishable photons from separated silicon-vacancy centers in diamond," *Phys. Rev. Lett.*, vol. 113, no. 11, 2014.

[166] J. Brendel, N. Gisin, W. Tittel, and H. Zbinden, "Pulsed energy-time entangled twin-photon source for quantum communication," *Phys. Rev. Lett.*, vol. 82, no. 12, pp. 2594–2597, 1999.

[167] P. G. Kwiat, A. M. Steinberg, and R. Y. Chiao, "High-visibility interference in a Bell-inequality experiment for energy and time," *Phys. Rev. A*, vol. 47, no. 4, 1993.

[168] K. Suhling, P. M. W. French, and D. Phillips, "Time-resolved fluorescence microscopy," *Photochem. Photobiol. Sci.*, vol. 4, no. 1, pp. 13–22, 2005.

[169] M. Wahl and S. Orthaus-müller, "Time Tagged Time-Resolved Fluorescence Data Collection in Life Sciences TTTR with Multiple Detectors and," *Tech. Note PicoQuant*, pp. 1–10, 2014.

[170] S. Ates *et al.*, "Two-photon interference using background-free quantum frequency conversion of single photons emitted by an InAs quantum dot," *Phys. Rev. Lett.*, vol. 109, no. 14, 2012.

[171] L. E. Myers and W. R. Bosenberg, “Periodically poled lithium niobate and quasi-phase-matched optical parametric oscillators,” *IEEE J. Quantum Electron.*, vol. 33, no. 10, pp. 1663–1672, 1997.

[172] C. Sulem and P. L. Sulem, “The Nonlinear Schrödinger Equation: Self-Focusing and Wave Collapse,” *Nonlinear Schrödinger Equ. Self-Focusing Wave Collapse*, 2004.

[173] A. B. Datseff, “On the nonlinear schrödinger equation,” *Int. J. Quantum Chem.*, vol. 28, no. 19 S, pp. 739–740, 1985.

[174] P. D. Lax, “Integrals of nonlinear equations of evolution and solitary waves,” *Commun. Pure Appl. Math.*, vol. 21, no. 5, pp. 467–490, 1968.

[175] Y. Silberberg, “Collapse of optical pulses,” *Opt. Lett.*, vol. 15, no. 22, p. 1282, 1990.

[176] F. Lederer, G. I. Stegeman, D. N. Christodoulides, G. Assanto, M. Segev, and Y. Silberberg, “Discrete solitons in optics,” *Physics Reports*, vol. 463, no. 1–3. pp. 1–126, 2008.

[177] G. P. Agrawal, “Optical pulse propagation in doped fiber amplifiers,” *Phys. Rev. A*, vol. 44, no. 11, pp. 7493–7501, 1991.

[178] R. W. Boyd, “Optically Induced Damage and Multiphoton Absorption,” in *Nonlinear Optics*, 2008, pp. 543–560.

[179] D. Cai, A. R. Bishop, and N. Grønbech-Jensen, “Localized states in discrete nonlinear Schrödinger equations,” *Phys. Rev. Lett.*, vol. 72, no. 5, pp. 591–595, 1994.

[180] W. E. Torruellas *et al.*, “Observation of two-dimensional spatial solitary waves in a quadratic medium,” *Phys. Rev. Lett.*, vol. 74, no. 25, pp. 5036–5039, 1995.

[181] J. F. Henninot, M. Debailleul, F. Derrien, G. Abbate, and M. Warenghem, “(2D + 1) Spatial optical solitons in dye doped liquid crystals,” in *Synthetic Metals*, 2001, vol. 124, no. 1, pp. 9–13.

[182] Z. Chen, M. Mitchell, M. Segev, T. H. Coskun, and D. N. Christodoulides, “Self-trapping of dark incoherent light beams,” *Science (80-.).*, vol. 280, no. 5365, pp. 889–891, 1998.

[183] E. DelRe, M. Tamburrini, M. Segev, E. Refaeli, and A. J. Agranat, “Two-dimensional photorefractive spatial solitons in centrosymmetric paraelectric potassium-lithium-tantalate-niobate,” *Appl. Phys. Lett.*, vol. 73, no. 1, pp. 16–18, 1998.

[184] E. W. Laedke, K. H. Spatschek, and S. K. Turitsyn, “Stability of discrete solitons and quasicollapse to intrinsically localized modes,” *Phys. Rev. Lett.*, vol. 73, no. 8, pp. 1055–1059, 1994.

[185] J. CHRIS EILBECK and M. JOHANSSON, “the Discrete Nonlinear Schrödinger Equation — 20 Years on,” 2003, pp. 44–67.

[186] P. G. Kevrekidis, “The discrete nonlinear schrödinger equation: Mathematical analysis, numerical computations and physical perspectives,” *Springer Tracts Mod. Phys.*, vol. 232, 2009.

[187] A. Ankiewicz and N. Akhmediev, *Dissipative Solitons: From Optics to Biology and Medicine*, vol. 751, no. 2008. 2008.

[188] A. M. Rubenchik, I. S. Chekhovskoy, M. P. Fedoruk, O. V. Shtyrina, and S. K. Turitsyn, "Nonlinear pulse combining and pulse compression in multi-core fibers," *Opt. Lett.*, vol. 40, no. 5, p. 721, 2015.

[189] F. Lederer, G. I. Stegeman, D. N. Christodoulides, G. Assanto, M. Segev, and Y. Silberberg, "Discrete solitons in optics," *Physics Reports*, vol. 463, no. 1–3. pp. 1–126, 2008.

[190] A. Szameit, J. Burghoff, T. Pertsch, S. Nolte, A. Tünnermann, and F. Lederer, "Two-dimensional soliton in cubic fs laser written waveguide arrays in fused silica," *Opt. Express*, vol. 14, no. 13, p. 6055, 2006.

[191] S. Minardi *et al.*, "Three-dimensional light bullets in arrays of waveguides," *Phys. Rev. Lett.*, vol. 105, no. 26, 2010.

[192] K. D. Moll, A. L. Gaeta, and G. Fibich, "Self-Similar Optical Wave Collapse: Observation of the Townes Profile," *Phys. Rev. Lett.*, vol. 90, no. 20, p. 4, 2003.

[193] P. L. Christiansen *et al.*, "Discrete localized states and localization dynamics in discrete nonlinear Schrödinger equations," *Phys. Scr. T*, vol. 67, no. T67, pp. 160–166, 1996.

[194] R. El-Ganainy, K. G. Makris, M. Khajavikhan, Z. H. Musslimani, S. Rotter, and D. N. Christodoulides, "Non-Hermitian physics and PT symmetry," *Nature Physics*, vol. 14, no. 1. pp. 11–19, 2018.

[195] C. M. Bender, S. Boettcher, and P. N. Meisinger, "PT-symmetric quantum mechanics," *J. Math. Phys.*, vol. 40, no. 5, pp. 2201–2229, 1999.

[196] C. M. Bender and S. Boettcher, "Real spectra in non-hermitian hamiltonians having PT symmetry," *Phys. Rev. Lett.*, vol. 80, no. 24, pp. 5243–5246, 1998.

[197] S. V. Suchkov, A. A. Sukhorukov, J. Huang, S. V. Dmitriev, C. Lee, and Y. S. Kivshar, "Nonlinear switching and solitons in PT-symmetric photonic systems," *Laser Photonics Rev.*, vol. 10, no. 2, pp. 177–213, 2016.

[198] X. Zhu, H. Wang, L.-X. Zheng, H. Li, and Y.-J. He, "Gap solitons in parity-time complex periodic optical lattices with the real part of superlattices," *Opt. Lett.*, vol. 36, no. 14, p. 2680, 2011.

[199] A. K. Jahromi, A. U. Hassan, D. N. Christodoulides, and A. F. Abouraddy, "Statistical parity-time-symmetric lasing in an optical fibre network," *Nat. Commun.*, vol. 8, no. 1, 2017.

[200] B. Peng *et al.*, "Parity-time-symmetric whispering-gallery microcavities," *Nat. Phys.*, vol. 10, no. 5, pp. 394–398, 2014.

[201] Z. Lin, H. Ramezani, T. Eichelkraut, T. Kottos, H. Cao, and D. N. Christodoulides, "Unidirectional invisibility induced by PT-symmetric periodic structures," *Phys. Rev. Lett.*, vol. 106, no. 21, 2011.

[202] H. Zhou, J. Y. Lee, S. Liu, and B. Zhen, “Exceptional surfaces in PT -symmetric photonic systems,” *arXiv*, 2018.

[203] H. Zhao, S. Longhi, and L. Feng, “Robust light state by quantum phase transition in non-hermitian optical materials,” *Sci. Rep.*, vol. 5, 2015.

[204] A. A. Sukhorukov, S. V. Dmitriev, S. V. Suchkov, and Y. S. Kivshar, “Nonlocality in PT-symmetric waveguide arrays with gain and loss,” *Opt. Lett.*, vol. 37, no. 11, p. 2148, 2012.

[205] X. Y. Lü, H. Jing, J. Y. Ma, and Y. Wu, “P T -Symmetry-Breaking Chaos in Optomechanics,” *Phys. Rev. Lett.*, vol. 114, no. 25, 2015.

[206] J. Schindler, Z. Lin, J. M. Lee, H. Ramezani, F. M. Ellis, and T. Kottos, “PI-symmetric electronics,” *J. Phys. A Math. Theor.*, vol. 45, no. 44, 2012.

[207] Y. Liu, T. Hao, W. Li, J. Capmany, N. Zhu, and M. Li, “Observation of parity-time symmetry in microwave photonics,” *Light Sci. Appl.*, vol. 7, no. 1, 2018.

[208] Y. Xuan *et al.*, “High-Q silicon nitride microresonators exhibiting low-power frequency comb initiation,” *Optica*, vol. 3, no. 11, p. 1171, 2016.

[209] C. E. Rüter, K. G. Makris, R. El-Ganainy, D. N. Christodoulides, M. Segev, and D. Kip, “Observation of parity-time symmetry in optics,” *Nat. Phys.*, vol. 6, no. 3, pp. 192–195, 2010.

[210] H. Alaeian and J. A. Dionne, “Non-Hermitian nanophotonic and plasmonic waveguides,” *Phys. Rev. B - Condens. Matter Mater. Phys.*, vol. 89, no. 7, 2014.

[211] H. Benisty *et al.*, “Implementation of PT symmetric devices using plasmonics: principle and applications,” *Opt. Express*, vol. 19, no. 19, p. 18004, 2011.

[212] S. Zhang, Z. Yong, Y. Zhang, and S. He, “Parity-time symmetry breaking in coupled nanobeam cavities,” *Sci. Rep.*, vol. 6, 2016.

[213] W. Li, C. Li, and H. Song, “Theoretical realization and application of parity-time-symmetric oscillators in a quantum regime,” *Phys. Rev. A*, vol. 95, no. 2, 2017.

[214] M. Kremer, T. Biesenthal, L. J. Maczewsky, M. Heinrich, R. Thomale, and A. Szameit, “Demonstration of a two-dimensional PT -symmetric crystal,” *Nat. Commun.*, vol. 10, no. 1, 2019.

[215] S. Weimann *et al.*, “Topologically protected bound states in photonic parity–time-symmetric crystals,” *Nat. Mater.*, vol. 16, no. 4, pp. 433–438, 2017.

[216] G. Björk, A. Karlsson, and Y. Yamamoto, “Definition of a laser threshold,” *Phys. Rev. A*, vol. 50, no. 2, pp. 1675–1680, 1994.

[217] P. Grelu and N. Akhmediev, “Dissipative solitons for mode-locked lasers,” *Nature Photonics*, vol. 6, no. 2. pp. 84–92, 2012.

[218] N. Moiseyev, *Non-hermitian quantum mechanics*. 2011.

[219] R. El-Ganainy, K. G. Makris, M. Khajavikhan, Z. H. Musslimani, S. Rotter, and D. N. Christodoulides, “Non-Hermitian physics and PT symmetry,” *Nature Physics*, vol. 14,

no. 1. pp. 11–19, 2018.

[220] A. E. Miroshnichenko, B. A. Malomed, and Y. S. Kivshar, “Nonlinearly PT-symmetric systems: Spontaneous symmetry breaking and transmission resonances,” *Phys. Rev. A - At. Mol. Opt. Phys.*, vol. 84, no. 1, 2011.

[221] N. V. Alexeeva, I. V. Barashenkov, A. A. Sukhorukov, and Y. S. Kivshar, “Optical solitons in PT-symmetric nonlinear couplers with gain and loss,” *Phys. Rev. A - At. Mol. Opt. Phys.*, vol. 85, no. 6, 2012.

[222] M. Parto *et al.*, “Complex edge-state phase transitions in 1d topological laser arrays,” *arXiv*, 2017.

[223] Y. N. Joglekar, D. Scott, M. Babbey, and A. Saxena, “Robust and fragile PT-symmetric phases in a tight-binding chain,” *Phys. Rev. A - At. Mol. Opt. Phys.*, vol. 82, no. 3, 2010.

[224] E. M. Graefe and H. F. Jones, “PT-symmetric sinusoidal optical lattices at the symmetry-breaking threshold,” *Phys. Rev. A - At. Mol. Opt. Phys.*, vol. 84, no. 1, 2011.

[225] A. Guo *et al.*, “Observation of PT-symmetry breaking in complex optical potentials,” *Phys. Rev. Lett.*, vol. 103, no. 9, 2009.

[226] S. Klaiman, U. Günther, and N. Moiseyev, “Visualization of branch points in PT-symmetric waveguides,” *Phys. Rev. Lett.*, vol. 101, no. 8, 2008.

[227] Y. D. Chong, L. Ge, and A. D. Stone, “PT-symmetry breaking and laser-absorber modes in optical scattering systems,” *Phys. Rev. Lett.*, vol. 106, no. 9, 2011.

[228] H. Ramezani, T. Kottos, R. El-Ganainy, and D. N. Christodoulides, “Unidirectional nonlinear PT-symmetric optical structures,” *Phys. Rev. A - At. Mol. Opt. Phys.*, vol. 82, no. 4, 2010.

[229] A. Regensburger, C. Bersch, M. A. Miri, G. Onishchukov, D. N. Christodoulides, and U. Peschel, “Parity-time synthetic photonic lattices,” *Nature*, vol. 488, no. 7410, pp. 167–171, 2012.

[230] H. Schomerus, “Quantum noise and self-sustained radiation of PT-symmetric systems,” *Phys. Rev. Lett.*, vol. 104, no. 23, 2010.

[231] S. Longhi, “PT-symmetric laser absorber,” *Phys. Rev. A - At. Mol. Opt. Phys.*, vol. 82, no. 3, 2010.

[232] Z. Lin, H. Ramezani, T. Eichelkraut, T. Kottos, H. Cao, and D. N. Christodoulides, “Unidirectional invisibility induced by PT-symmetric periodic structures,” *Phys. Rev. Lett.*, vol. 106, no. 21, 2011.

[233] M. Kulishov, J. M. Laniel, N. Bélanger, J. Azaña, and D. V. Plant, “Nonreciprocal waveguide Bragg gratings,” *Opt. Express*, vol. 13, no. 8, p. 3068, 2005.

[234] L. Feng *et al.*, “Experimental demonstration of a unidirectional reflectionless parity-time metamaterial at optical frequencies,” *Nat. Mater.*, vol. 12, no. 2, pp. 108–113, 2013.

[235] Z. H. Musslimani, K. G. Makris, R. El-Ganainy, and D. N. Christodoulides, “Optical solitons in PT periodic potentials,” *Phys. Rev. Lett.*, vol. 100, no. 3, 2008.

[236] R. El-Ganainy, K. G. Makris, D. N. Christodoulides, and Z. H. Musslimani, “Theory of coupled optical PT-symmetric structures,” *Opt. Lett.*, vol. 32, no. 17, p. 2632, 2007.

[237] B. Midya, B. Roy, and R. Roychoudhury, “A note on the PT invariant periodic potential V (x) = 4 cos2 x + 4 i V0 sin 2 x,” *Phys. Lett. Sect. A Gen. At. Solid State Phys.*, vol. 374, no. 26, pp. 2605–2607, 2010.

[238] I. V. Barashenkov, S. V. Suchkov, A. A. Sukhorukov, S. V. Dmitriev, and Y. S. Kivshar, “Breathers in PT-symmetric optical couplers,” *Phys. Rev. A - At. Mol. Opt. Phys.*, vol. 86, no. 5, 2012.

[239] N. V. Alexeeva, I. V. Barashenkov, A. A. Sukhorukov, and Y. S. Kivshar, “Optical solitons in PT-symmetric nonlinear couplers with gain and loss,” *Phys. Rev. A - At. Mol. Opt. Phys.*, vol. 85, no. 6, 2012.

[240] K. D. Moll, A. L. Gaeta, and G. Fibich, “Self-Similar Optical Wave Collapse: Observation of the Townes Profile,” *Phys. Rev. Lett.*, vol. 90, no. 20, p. 4, 2003.

[241] P. G. Kevrekidis, *The discrete nonlinear schrödinger equation: Mathematical analysis, numerical computations and physical perspectives*, vol. 232. Berlin, Heidelberg: Springer Berlin Heidelberg, 2009.

[242] L. Feng, R. El-Ganainy, and L. Ge, “Non-Hermitian photonics based on parity-time symmetry,” *Nature Photonics*, vol. 11, no. 12. pp. 752–762, 2017.

[243] S. V. Suchkov, A. A. Sukhorukov, J. Huang, S. V. Dmitriev, C. Lee, and Y. S. Kivshar, “Nonlinear switching and solitons in PT-symmetric photonic systems,” *Laser Photonics Rev.*, vol. 10, no. 2, pp. 177–213, 2016.

[244] M. V. Berry, “Optical lattices with PT symmetry are not transparent,” *J. Phys. A Math. Theor.*, vol. 41, no. 24, 2008.

[245] A. Mock, “Parity-time-symmetry breaking in two-dimensional photonic crystals: Square lattice,” *Phys. Rev. A*, vol. 93, no. 6, 2016.

[246] Y. S. Kivshar and D. K. Campbell, “Peierls-Nabarro potential barrier for highly localized nonlinear modes,” *Phys. Rev. E*, vol. 48, no. 4, pp. 3077–3081, 1993.

[247] R. Morandotti *et al.*, “Interactions of discrete solitons with structural defects,” *Opt. Lett.*, vol. 28, no. 10, p. 834, 2003.

[248] Z. Chen, M. Segev, and D. N. Christodoulides, “Optical spatial solitons: Historical overview and recent advances,” *Reports on Progress in Physics*, vol. 75, no. 8. 2012.

[249] E. W. Laedke, K. H. Spatschek, and S. K. Turitsyn, “Stability of discrete solitons and quasicollapse to intrinsically localized modes,” *Phys. Rev. Lett.*, vol. 73, no. 8, pp. 1055–1059, 1994.

[250] M. Johansson, J. E. Prilepsky, and S. A. Derevyanko, “Strongly localized moving discrete dissipative breather-solitons in Kerr nonlinear media supported by intrinsic gain,” *Phys. Rev. E - Stat. Nonlinear, Soft Matter Phys.*, vol. 89, no. 4, 2014.

[251] K. G. Makris, R. El-Ganainy, D. N. Christodoulides, and Z. H. Musslimani, “Beam dynamics in PT symmetric optical lattices,” *Phys. Rev. Lett.*, vol. 100, no. 10, 2008.

[252] L. Brizhik, A. Eremko, and L. Cruzeiro-Hansson, “Soliton dynamics and Peierls-Nabarro barrier in a discrete molecular chain,” *Phys. Rev. B - Condens. Matter Mater. Phys.*, vol. 61, no. 2, pp. 1129–1141, 2000.

[253] C. Laroche, T. Dauxois, and M. Peyrard, “Discreteness effects on soliton dynamics: A simple experiment,” *Am. J. Phys.*, vol. 68, no. 6, pp. 552–555, 2000.

[254] G. Assanto, L. A. Cisneros, A. A. Minzoni, B. D. Skuse, N. F. Smyth, and A. L. Worthy, “Soliton steering by longitudinal modulation of the nonlinearity in waveguide arrays,” *Phys. Rev. Lett.*, vol. 104, no. 5, 2010.

[255] Z. Xu, Y. V. Kartashov, and L. Torner, “Soliton mobility in nonlocal optical lattices,” *Phys. Rev. Lett.*, vol. 95, no. 11, 2005.

[256] T. Mayteevarunyoo, B. A. Malomed, and A. Reoksabutr, “Solvable model for solitons pinned to a parity-time-symmetric dipole,” *Phys. Rev. E - Stat. Nonlinear, Soft Matter Phys.*, vol. 88, no. 2, 2013.

[257] S. V. Suchkov *et al.*, “Phase sensitivity of light dynamics in PT-symmetric couplers,” *Appl. Phys. A Mater. Sci. Process.*, vol. 115, no. 2, pp. 443–447, 2014.

[258] C. Hang, Y. V. Kartashov, G. Huang, and V. V. Konotop, “Localization of light in a parity-time-symmetric quasi-periodic lattice,” *Opt. Lett.*, vol. 40, no. 12, p. 2758, 2015.

[259] Y. Lumer, Y. Plotnik, M. C. Rechtsman, and M. Segev, “Nonlinearly induced PT transition in photonic systems,” *Phys. Rev. Lett.*, vol. 111, no. 26, 2013.

[260] V. V. Konotop, J. Yang, and D. A. Zezyulin, “Nonlinear waves in PT -symmetric systems,” *Rev. Mod. Phys.*, vol. 88, no. 3, 2016.

Acknowledgments

I would like to offer my special thanks to my supervisor, Professor Dr. Ulf Peschel, for the patient guidance, leadership, encouragement, and advice he has provided throughout my time as his student. Your advice on both research as well as on my career has been invaluable. I wish to acknowledge the help and technical discussions provided by Dr. Martin Wimmer and Dr. Arstan Bisianov as well. In particular, I would like to thank Professor Dr. Demetri Christodoulides and Dr. Pawel Jung from the University of Central Florida, USA, as well as Professor Dr. Roberto Morandotti from the *Institut National de la Recherche Scientifique-EMT*, Canada, for the collaborative projects and technical guidance.

A special thanks to my father and mother for all of the sacrifices that they have made on my behalf. I would also like to thank my beloved wife Glenda Figueiredo Zanela for all the patience and encouragement throughout my doctorate studies.

I would also like to thank the financial support from *Deutsche Forschungsgemeinschaft* (DFG, German research funding organization) as well as NSERC (Canadian National Science and Engineering Research Council) throughout the International Research Training group 2101: Guided light, tightly packed: novel concepts, components, and applications. A special thanks to the coordinator of the doctoral program Dr. Anna Späthe for all the support and advice.

Appendices

A. Eigenvalue derivation of 1D photonic mesh lattice

In the linear regime, the 1D evolution equation for a single time step is given by

$$v_x^{m+1} = (t_{x+1}^m v_{x+1}^m + i r_{x+1}^m u_{x+1}^m)\exp(i\varphi_v) \text{ and}$$
$$u_x^{m+1} = (t_{x-1}^m u_{x-1}^m + i r_{x-1}^m v_{x-1}^m)\exp(i\varphi_u), \tag{1}$$

where t_x^m and r_x^m indicate transmission and reflection of the optical coupler. A phase modulation φ_u and φ_v is applied to loop v and u according to an arrangement as

$$\varphi_v(m) = \begin{cases} 0, & \text{odd } m \\ \varphi_0, & \text{even } m \end{cases} \quad \text{and}$$
$$\varphi_u(m) = \begin{cases} \varphi_0, & \text{odd } m \\ 0, & \text{even } m \end{cases}. \tag{2}$$

For calculating the eigenvector of a 1D system, the evolution equation in Equation (1) and phase modulation in Equation (2) are converted in matrix evolution as

$$\hat{C} = \begin{pmatrix} \cos(\vartheta) & i\sin(\vartheta) \\ i\sin(\vartheta) & \cos(\vartheta) \end{pmatrix} \tag{3}$$

$$\hat{\varphi}_{odd} = \begin{pmatrix} 0 & 0 \\ 0 & \varphi_0 \end{pmatrix} \tag{4}$$

$$\hat{\varphi}_{even} = \begin{pmatrix} \varphi_0 & 0 \\ 0 & 0 \end{pmatrix} \tag{5}$$

$$\hat{Q} = \begin{pmatrix} e^{ik_x} & e^{ik_x} \\ e^{-ik_x} & e^{-ik_x} \end{pmatrix} \tag{6}$$

where ϑ is the transfer matrix angles of an optical coupler ($t = \cos(\vartheta)$ and $r = \sin(\vartheta)$; e.g. $\vartheta = \pi/4$ denotes a 50/50 coupler), $\hat{\varphi}$ is a phase modulation matrix for odd and even time steps and $\hat{Q}$ is the single-time step Bloch ansatz, which physically represents the direction of pulses spanned on the synthetic transverse coordinate x.

The temporal evolution matrix $\hat{T}_{1D}$ is a result of a double-time step evolution since 1D mesh lattice has a periodicity of two:

$$\hat{T}_{1D} = \underbrace{\hat{C} \cdot e^{i\hat{\varphi}_{odd}} \cdot \hat{Q}}_{\text{odd } m} \cdot \underbrace{\hat{C} \cdot e^{i\hat{\varphi}_{even}} \cdot \hat{Q}}_{\text{even } m}, \tag{7}$$

here $\hat{C}$ and $\hat{Q}$ do not change from odd to even time steps. Additionally, a Floquet ansatz $\hat{\lambda}$ of the system is written as

$$\hat{\lambda} = e^{-i\theta} \begin{pmatrix} 1 & 0 \\ 0 & 1 \end{pmatrix}, \tag{8}$$

where θ is the propagation constant (i.e. eigenvalue of the system). A dispersion relation is calculated by solving the eigenvalue problem

$$\det\left(\hat{T}_{1D} - \hat{\lambda}\right) = 0, \tag{9}$$

which results in a band structure

$$\cos\theta = \cos^2(\vartheta)\cos k_x - \sin^2(\vartheta)\sin\varphi_0. \tag{10}$$

Here, it introduces a variable C for simplifying Equation (10), which represents a splitting ratio of the optical coupler ($C = t^2 = 1 - r^2$):

$$\cos\theta = C\cos k_x - (1 - C)\sin\varphi_0. \tag{11}$$

Next, an eigenvector $(V, U)^t$ is derived from Equations (7) to probe an excitation onto a specific region of the band structure. By defining system parameters, such as phase modulation height φ_0 and splitting ratio C, the eigenvector of Equation (7) is found

$$\text{eigenvector}\left(\hat{T}_{1D}\right)\Big|_{k_x \to 0} = \begin{pmatrix} V \\ U \end{pmatrix}, \tag{12}$$

where Bloch momentum tends to zero (i.e. $\hat{Q}(k_x \to 0)$) in the center of the Brillouin zone, which represents a narrow momentum spread excitation (i.e. a broad Gaussian distribution).

B. Eigenvalue derivation of 2D photonic mesh lattice

First, the 2D evolution equations are reduced to two equations since $a_{x,y}^{m}$ and $b_{x,y}^{m}$ are uniquely determined by $c_{x,y}^{m-1}$ and $d_{x,y}^{m-1}$ and those depend on $a_{x,y}^{m-1}$ and $b_{x,y}^{m-1}$ only. Therefore, the simplified 2D evolution equations for a single time step in the linear regime are given by

$$a_{x,y}^{m+1} = \frac{1}{2}\{a_{x-1,y-1}^{m} + ib_{x-1,y-1}^{m} + (ib_{x-1,y+1}^{m} - a_{x-1,y+1}^{m})\exp[i(-1)^{m-1}\varphi_0]\} \text{ and}$$
$$b_{x,y}^{m+1} = \frac{1}{2}\{(b_{x+1,y+1}^{m} + ia_{x+1,y+1}^{m})\exp[i(-1)^{m-1}\varphi_0] + ia_{x+1,y-1}^{m} - b_{x+1,y-1}^{m}\}, \tag{1}$$

where couplers are set to a 50/50 splitting ratio and $\varphi_a = \varphi_c = 0$, while φ_b and φ_d follow a phase modulation as follows

$$\varphi_{b,d}(m) = \begin{cases} -\varphi_0, & \text{odd } m \\ +\varphi_0, & \text{even } m \end{cases}. \tag{2}$$

Here, the eigenvector and correspondent eigenvalues are calculated by converting Equations (1),(2) into matrix evolution as

$$\hat{C}_{AB} = \hat{C}_{CD} = \frac{1}{\sqrt{2}}\begin{pmatrix} 1 & i \\ i & 1 \end{pmatrix}, \tag{3}$$

$$\hat{\varphi}_{odd} = \begin{pmatrix} 1 & 0 \\ 0 & -\varphi_0 \end{pmatrix}, \tag{4}$$

$$\hat{\varphi}_{even} = \begin{pmatrix} 1 & 0 \\ 0 & \varphi_0 \end{pmatrix}, \tag{5}$$

$$\hat{Q}_x = \begin{pmatrix} e^{ik_x} & 0 \\ 0 & e^{-ik_x} \end{pmatrix}, \tag{6}$$

$$\hat{Q}_y = \begin{pmatrix} e^{ik_y} & 0 \\ 0 & e^{-ik_y} \end{pmatrix}, \tag{7}$$

where $\hat{C}_{AB}$ and $\hat{C}_{CD}$ are the 50/50 splitting ratio of optical couplers connecting loops A/B to C/D, $\hat{\varphi}$ is a phase modulation matrix for odd and even time steps from Equation (2), and $\hat{Q}_x$ and $\hat{Q}_y$ are the single time step Bloch ansatz, which physically represents the direction of

pulses spanned on the synthetic transverse coordinate x and y, respectively. Similarly, the 2D the system has a periodicity of two and thus the double step 2D temporal matrix evolution $\hat{T}$ is written as.

$$\hat{T}_{2D} = \underbrace{\underbrace{\hat{C}_{AB} \cdot e^{i\hat{\varphi}_{odd}} \cdot \hat{Q}_x}_{\text{loop A and B}} \cdot \underbrace{\hat{C}_{CD} \cdot e^{i\hat{\varphi}_{odd}} \cdot \hat{Q}_y}_{\text{loop C and D}}}_{\text{odd } m} \cdot \underbrace{\underbrace{\hat{C}_{AB} \cdot e^{i\hat{\varphi}_{even}} \cdot \hat{Q}_x}_{\text{loop A and B}} \cdot \underbrace{\hat{C}_{CD} \cdot e^{i\hat{\varphi}_{even}} \cdot \hat{Q}_y}_{\text{loop C and D}}}_{\text{even } m} \tag{8}$$

Additionally, a Floquet ansatz $\hat{\lambda}$ of the system is written as

$$\hat{\lambda} = e^{-i\theta} \begin{pmatrix} 1 & 0 \\ 0 & 1 \end{pmatrix}, \tag{9}$$

where θ is the propagation constant (i.e. eigenvalue of the system). A dispersion relation is calculated by solving the following equation

$$\det\left(\hat{T}_{2D} - \hat{\lambda}\right) = 0, \tag{10}$$

which results in a band structure

$$\begin{aligned} \cos(\theta) = \pm\frac{1}{2}[-\frac{1}{2} - \frac{1}{2}\cos(2\varphi_0) - \cos(\varphi_0)\cos(k_x) - \cos(\varphi)\cos\left(k_y\right) \\ + \cos(k_x)\cos\left(k_y\right)] \end{aligned} \tag{11}$$

Next, an eigenvector $(A, B)^t$ consisting of two components, which describe the amplitude and phase relation between loops A and B from Equation (1) is derived to probe an excitation onto a specific region of the band structure. By defining the phase modulation height φ_0, the eigenvector of Equation (8) is found

$$\text{eigenvector}\left(\hat{T}_{2D}\right)\Big|_{k_x \to 0;\, k_y \to 0} = \begin{pmatrix} A \\ B \end{pmatrix}, \tag{12}$$

where Bloch momenta tend to zero (i.e. $\hat{Q}_x(k_x \to 0)$ and $\hat{Q}_y\left(k_y \to 0\right)$) in the center of the Brillouin zone, which represents a narrow momentum spread excitation (i.e. a broad Gaussian distribution).

C. Eigenvalue derivation of 2D $\mathcal{PT}$-symmetric photonic mesh lattice

Similar to its counterpart, 2D $\mathcal{PT}$-symmetric mesh lattice can be represented by matrix evolution to calculate its eigenvector (A_1, B_1, A_2, B_2) and the corresponding eigenvalues. First, the splitting ratio and Bloch momentum is written as

$$\hat{C} = \hat{C}_{AB} = \hat{C}_{CD} = \frac{1}{\sqrt{2}}\begin{pmatrix} 1 & i \\ i & 1 \end{pmatrix}, \tag{1}$$

$$\hat{Q}_x = \begin{pmatrix} e^{ik_x} & 0 \\ 0 & e^{-ik_x} \end{pmatrix}, \tag{2}$$

$$\hat{Q}_y = \begin{pmatrix} e^{ik_y} & 0 \\ 0 & e^{-ik_y} \end{pmatrix}. \tag{3}$$

According to Equation (80)-(83) and Figure 40, 2D $\mathcal{PT}$-symmetric mesh lattice has a periodicity of two and the matrix evolution comprises of 4-by-4 components due to its extended unit cell:

$$\hat{U}_{\mathrm{PT}}(g, \varphi_0) \stackrel{\text{def}}{=} \sum_{x,y} \hat{U}_{\mathrm{PT}_{x,y}}(g, \varphi_0) =$$

$$= \sum_{x,y} \left[\begin{pmatrix} \hat{\Phi}(\varphi_0)\hat{G}(g)\hat{Q}_x\hat{C}\hat{Q}_y\hat{C}\hat{C}\hat{C}^\dagger & -\hat{\Phi}(\varphi_0)\hat{Q}_x\hat{C}\hat{Q}_y^\dagger\hat{C}^\dagger\hat{C}^\dagger \\ -\hat{\Phi}(-\varphi_0)\hat{Q}_x\hat{C}\hat{Q}_y^\dagger\hat{C}^\dagger\hat{C}^\dagger & \hat{\Phi}(-\varphi_0)\hat{G}(-g)\hat{Q}_x\hat{C}\hat{Q}_y\hat{C}\hat{C} \end{pmatrix} * \right.$$

$$\left. * \begin{pmatrix} \hat{\Phi}(\varphi_0)\hat{G}(-g)\hat{Q}_x\hat{C}\hat{Q}_y\hat{C}\hat{C} & -\hat{\Phi}(\varphi_0)\hat{Q}_x\hat{C}\hat{Q}_y^\dagger\hat{C}^\dagger\hat{C}^\dagger \\ -\hat{\Phi}(-\varphi_0)\hat{Q}_x\hat{C}\hat{Q}_y^\dagger\hat{C}^\dagger\hat{C}^\dagger & \hat{\Phi}(-\varphi_0)\hat{G}(g)\hat{Q}_x\hat{C}\hat{Q}_y\hat{C}\hat{C} \end{pmatrix} \right], \tag{4}$$

where $\Phi(\varphi_0)$ and $G(g)$ describe elements of the $\mathcal{PT}$-symmetric phase and gain/loss modulation, respectively

$$\hat{\Phi}(\varphi_0) \stackrel{\text{def}}{=} e^{i\varphi_0}\begin{pmatrix} 1 & 0 \\ 0 & -1 \end{pmatrix} \tag{5}$$

$$\hat{G}(g) \stackrel{\text{def}}{=} e^{g}\begin{pmatrix} 1 & 0 \\ 0 & -1 \end{pmatrix}, g \in \mathbb{R} \tag{6}$$

Here, φ_0 is the phase modulation height and the arguments g and $-g$ of $\hat{G}$ characterize the gain and loss parameters of the modulation, respectively. Hence, the

evolution equation for the wave at a fixed position (x, y) reads

$$U_{\mathrm{PT}_{x,y}}(g,\varphi_0)e^{i(k_x x+k_y y)}\begin{pmatrix}A_1\\B_1\\A_2\\B_2\end{pmatrix}_{k_x,k_y} = e^{-i\theta}e^{i(k_x x+k_y y)}\begin{pmatrix}A_1\\B_1\\A_2\\B_2\end{pmatrix}_{k_x,k_y}. \tag{7}$$

Furthermore, the eigenvalue problem

$$U_{\mathrm{PT}_{x,y}}(g,\varphi_0)\begin{pmatrix}A_1\\B_1\\A_2\\B_2\end{pmatrix}_{k_x,k_y} = e^{i\theta}\begin{pmatrix}A_1\\B_1\\A_2\\B_2\end{pmatrix}_{k_x,k_y}, \tag{8}$$

delivers the corresponding eigenvalues λ of four quasi-energy bands $\theta = -i\ln\left(\lambda(k_x, k_y)\right)$ as

$$\begin{aligned}
&\cos\left(\theta(k_x, k_y, \varphi_0, g)\right) = \\
&= \pm\frac{1}{8}\Bigg(-2\cos(g) + \cos(k_x - k_y) - 4\cos(\varphi_o)\sin^2\left(\frac{k_x + k_y}{2}\right) \\
&\pm\sqrt{2}cos\left(\frac{k_x + k_y}{2}\right)[14 - 6\cos(2\varphi_o) + 4\cos(\varphi_o - g) \\
&+4\cos(\varphi_o + g) + \cos(2\varphi_o - k_x - k_y) + 4\cos(\varphi_o + k_x - k_y) \\
&+4\cos(\varphi_o - k_x + k_y) + 4\cos(g - k_x + k_y) + 4\cos(g + k_x - k_y) \\
&-2\cos(k_x + k_y) + \cos(2\varphi_o + k_x + k_y)]^{1/2}\Bigg).
\end{aligned} \tag{9}$$

By defining the phase modulation height φ_0 and gain/loss strength g, the eigenvector of Equation (4)-(8) is found

$$\mathrm{eigenvector}(U_{\mathrm{PT}})|_{k_x\to 0;\, k_y\to 0} = \begin{pmatrix}A_1\\B_1\\A_2\\B_2\end{pmatrix}, \tag{10}$$

where Bloch momenta tend to zero (i.e. $\hat{Q}_x(k_x \to 0)$ and $\hat{Q}_y(k_y \to 0)$) in the center of the Brillouin zone, which represents a narrow momentum spread excitation (i.e. a broad Gaussian distribution).

D. Recovering phase information by the relative phase in loop v and u

In the linear regime ($\chi = 0$), the 1D evolution equation is described as

$$u_x^{m+1} = (t_{x-1}^m u_{x-1}^m + i r_{x-1}^m v_{x-1}^m)\exp(i\varphi_u), \tag{1}$$

$$v_x^{m+1} = (t_{x+1}^m v_{x+1}^m + i r_{x+1}^m u_{x+1}^m)\exp(i\varphi_v), \tag{2}$$

where m is the time step and x is the effective spatial position. t and r denote transmission and reflection of the variable coupler ($t^2 + r^2 = 1$). After photodetection, optical intensities in loop v and u are measured and organized as $|v_x^m|^2$ and $|u_x^m|^2$, respectively. First, let consider the intensity differences from loop v and u at time step $m+1$ as a result of its last time step m after an imbalance interferometer

$$|u_{x+1}^{m+1}|^2 - |v_{x-1}^{m+1}|^2 = |t_x^m u_x^m + i r_x^m v_x^m|^2 - |t_x^m v_x^m + i r_x^m u_x^m|^2. \tag{3}$$

Here, phase modulation in both loops, such as $\exp(i\varphi_u)$ and $\exp(i\varphi_v)$, are removed by the modulus. Individually, each part of that intensity subtraction in Equation (3) is written as

$$|t_x^m u_x^m + i r_x^m v_x^m|^2 = {t^2}_x^m |u_x^m|^2 + {r^2}_x^m |v_x^m|^2 + i t_x^m r_x^m u_x^m {v^\star}_x^m + i t_x^m r_x^m {u^\star}_x^m v_x^m, \tag{4}$$

$$|t_x^m v_x^m + i r_x^m u_x^m|^2 = {t^2}_x^m |v_x^m|^2 + {r^2}_x^m |u_x^m|^2 + i t_x^m r_x^m v_x^m {u^\star}_x^m + i t_x^m r_x^m {v^\star}_x^m u_x^m, \tag{5}$$

Next, by inserting Equations (4) and (5) into (3), it yields

$$|u_{x+1}^{m+1}|^2 - |v_{x-1}^{m+1}|^2 = \left({t^2}_x^m - {r^2}_x^m\right)(|u_x^m|^2 - |v_x^m|^2) + 2 t_x^m r_x^m \underbrace{\left(i {v^\star}_x^m u_x^m - i {u^\star}_x^m v_x^m\right)}_{2\Im\left({u^\star}_x^m v_x^m\right)}, \tag{6}$$

where $\Im(\cdot)$ denotes the imaginary component. The phase difference (i.e. $\phi_{uv} = \phi_u - \phi_v$) is found provided that $\Im\left({u^\star}_x^m v_x^m\right) = |u_x^m||v_x^m|\sin(\phi_{uv})$. Thus, Equation (6) is rewritten as

$$|u_{x+1}^{m+1}|^2 - |v_{x-1}^{m+1}|^2 = \left({t^2}_x^m - {r^2}_x^m\right)(|v_x^m|^2 - |u_x^m|^2) + 4 t_x^m r_x^m |u_x^m||v_x^m|\sin(\phi_{uv}), \tag{7}$$

Therefore, the phase difference information ϕ_{uv} is described as

$$\phi_{uv} = \sin^{-1}\left[\frac{|u_{x+1}^{m+1}|^2 - |v_{x-1}^{m+1}|^2 - \left({t^2}_x^m - {r^2}_x^m\right)(|u_x^m|^2 - |v_x^m|^2)}{4t_x^m r_x^m |u_x^m||v_x^m|}\right]. \tag{8}$$

For simplicity regarding experimental data processing, t and r are changed to coupling coefficient of that variable coupler, where $C_x^m = {t^2}_x^m = 1 - {r^2}_x^m$. Thus, provided that $t_x^m = \sqrt{C_x^m}$ and $r_x^m = \sqrt{1 - C_x^m}$, Equation (8) is rewritten in terms of C

$$\phi_{uv} = \sin^{-1}\left[\frac{|u_{x+1}^{m+1}|^2 - |v_{x-1}^{m+1}|^2 - (2C_x^m - 1)(|u_x^m|^2 - |v_x^m|^2)}{4\sqrt{C_x^m - {C^2}_x^m}|u_x^m||v_x^m|}\right]. \tag{9}$$

E. List of publications

Peer-reviewed publications (related to this dissertation)

Andre Luiz Marques Muniz, Martin Wimmer, Arstan Bisianov, Roberto Morandotti, and Ulf Peschel, "Collapse on the line – how synthetic dimensions influence nonlinear effects," *Scientific Reports* **9**, 9518 (2019), Jul. 2019.

Andre Luiz Marques Muniz, Alessandro Alberucci, Chandroth Pannian Jisha, Monika Monika, Stefan Nolte, Roberto Morandotti, and Ulf Peschel, "Kapitza light guiding in photonic mesh lattice," *Optics Letter* **44**, no. 24, pp. 6013–6016, Dec. 2019.

Andre Luiz Marques Muniz, Martin Wimmer, Arstan Bisianov, Roberto Morandotti, Pawel S. Jung, Demetrios N. Christodoulides, and Ulf Peschel, "2D Solitons in PT-Symmetric Photonic Lattices," *Physical Review Letter* **123**, no. 25, p. 253903, Dec. 2019.

Andre Luiz Marques Muniz, Pawel S. Jung, Fan O. Wu, Midya Parto, Mercedeh Khajavikhan, Demetrios N. Christodoulides, and Ulf Peschel, "Observation of photon-photon thermodynamics in nonlinear multimode optical lattices." (Submitted to *Nature* in February 2021).

Peer-reviewed publications (not related to this dissertation)

Arstan Bisianov, Andre Luiz Marques Muniz, Ulf Peschel, and Oleg Egorov, "Anomalous Floquet Interface States in Optical Fiber Loops." (Submitted to *Light Science & Applications* in January 2020).

Oral conference contributions (selected)

Andre Luiz Marques Muniz, Martin Wimmer, Arstan Bisianov, Demetrios N. Christodoulides, Roberto Morandotti and Ulf Peschel, "Nonlinear wave collapse in coupled fiber systems," *Conference on Lasers and Optics* (CLEO), San Jose, USA, 2018.

Andre Luiz Marques Muniz, Martin Wimmer, Arstan Bisianov, Demetrios N. Christodoulides, Roberto Morandotti, and Ulf Peschel, "Nonlinear wave collapse at mW-powers," *Photonics North*, Montreal, Canada, 2018.

Andre Luiz Marques Muniz, Martin Wimmer, Arstan Bisianov, Roberto Morandotti, and Ulf Peschel, "Experimental observation of PT soliton collapse in a 2D synthetic lattice," Postdeadline *Conference on Lasers and Optics* (CLEO), San Jose, USA, 2019.

Andre Luiz Marques Muniz, Martin Wimmer, Arstan Bisianov, R. Morandotti, and Ulf Peschel, “PT-symmetry in two synthetic dimensions,” Postdeadline *Conference on Lasers and Optics* (CLEO) Europe, Munich, Germany, 2019.

Andre Luiz Marques Muniz, Martin Wimmer, Arstan Bisianov, Roberto Morandotti, and Ulf Peschel, “Synthetic dimensions, PT-symmetry and nonlinearity in photonic mesh lattices,” *International Conference on Metamaterials, Photonic Crystals and Plasmonics*, Lisbon, Portugal, 2019.

F. Ehrenwörtliche Erklärung

Ich erkläre hiermit ehrenwörtlich, dass ich die vorliegende Arbeit selbständig, ohne unzulässige Hilfe Dritter und ohne Benutzung anderer als der angegebenen Hilfsmittel und Literatur angefertigt habe. Die aus anderen Quellen direkt oder indirekt übernommenen Daten und Konzepte sind unter Angabe der Quelle gekennzeichnet.

Niemand war an der inhaltlich-materiellen Erstellung der vorliegenden Arbeit beteiligt.Insbesondere habe ich hierf ̈ur nicht die entgeltliche Hilfe von Vermittlungs bzw. Beratungsdiensten (Promotionsberater oder andere Personen) in Anspruch genommen. Niemand hat von mir unmittelbar oder mittelbar geldwerte Leistungen f ̈ur Arbeiten erhalten, die im Zusammenhang mit dem Inhalt der vorgelegten Dissertation stehen.

Die Arbeit wurde bisher weder im In- noch im Ausland in gleicher oder ähnlicher Form einer anderen Prüfungsbehörde vorgelegt.

Die geltende Promotionsordnung der Physikalisch-Astronomischen Fakultät ist mir bekannt.

Ich versichere ehrenwörtlich, dass ich nach bestem Wissen die reine Wahrheit gesagt und nichts verschwiegen habe.

_____ _____

Ort, Datum Unterschrift d. Verfassers